The role of hypoxia-inducible factors (HIFs) in a mouse model of colorectal cancer

Dissertation

presented by

Vera Schützhold

from Papenburg

in partial fulfillment of the requirements
for the Degree of
Dr. rer. nat.

Faculty of Biology
Universität Duisburg-Essen

December 2019

The present work was performed in the research group of Prof. Dr. Joachim Fandrey at the Institute of Physiology, University Duisburg-Essen, from October 2016 to November 2019.

Supervisor: Prof. Dr. med Joachim Fandrey
Prof. Dr. med. Elke Cario

Chairman: Prof. Dr. Dr. Jürgen C. Becker

Date of Disputation: June 17, 2020

DOI: 10.17185/duepublico/71948
URN: urn:nbn:de:hbz:464-20200707-143021-1

Contents

1 Abstract 5
2 Zusammenfassung 6
3 Introduction 8
3.1 Ulcerative colitis 8
3.2 Colorectal cancer 9
3.3 The hypoxia-inducible factors (HIFs) – expression, regulation and inhibitors 12
3.4 The factor-inhibiting HIF (FIH) and its metabolic impact 15
3.5 HIFs in inflammation and cancer 16
4 Aim of the study 19
5 Materials and methods 20
5.1 Experimental animals 20
5.2 Laboratory equipment 20
5.3 Consumables and chemicals 21
5.4 Media and solutions 24
5.5 Mouse model of colorectal cancer (AOM-DSS) 26
5.6 Flow cytometry 28
5.7 Isolation of epithelial cells from the colon 29
5.8 RNA isolation and cDNA synthesis 30
5.9 Polymerase chain reaction (PCR) 31
5.10 Quantitative PCR (qPCR) 33
5.11 RNAseq 34
5.12 Lowry protein assay, SDS-PAGE, and Western Blot 35
5.13 Immunohistochemistry 36
5.14 *In situ* hybridization (RNAscope®) 39
5.15 Cell culturing and transfection 40
5.16 Cloning 42
5.17 Co-Immunoprecipitation (Co-IP) 43
5.18 Sensitized-emission Fluorescence Resonance Energy Transfer (seFRET) 44
5.19 Fluorescence lifetime imaging microscopy (FLIM) 46
5.20 Statistical analysis 48
6 Results 49
6.1 Efficiency of the FIH knockout in epithelial cells of the colon 49
6.2 Colitis progression and tumorigenesis in AOM-DSS-treated mice 51
6.3 Colitis progression and tumorigenesis in AOM-DSS-DMOG-treated mice 57
6.4 Effects of AOM-DSS(-DMOG) treatment on splenic immune cells 60

6.5 Immune response in the colon of AOM-DSS(-DMOG)-treated mice 63
6.6 Levels of HIF and hypoxia in AOM-DSS(-DMOG)-treated mice 70
6.7 Protein-protein interaction of HIF and FIH via co-immunoprecipitation 77
6.8 Protein-protein interaction of HIF and FIH via seFRET 78
6.9 Protein-protein interaction of HIF and FIH via FLIM 82
7 Discussion 86
7.1 Colon epithelial FIH knockout has no effect on tumor development in the AOM-DSS colon cancer mouse model 86
7.2 Colon epithelial knockout of FIH attenuates the disease progress in the AOM-DSS-DMOG colon cancer mouse model 87
7.3 FIH knockout in the colon epithelium decreases the inflammatory response in a chronic colitis 88
7.4 The interaction of HIF-1α and FIH 93
8 References 96
9 Appendix 108
9.1 Supplementary figures 108
9.2 Table of figures 111
9.3 Table of tables 113
9.4 Table of abbreviations 114
9.5 List of publications and congress contributions 117
9.6 Acknowledgements 119
9.7 Personal data sheet 120
9.8 Declarations 121

1 Abstract

Hypoxia is a characteristic feature of inflammation as well as of solid tumors and enforces a gene expression response controlled by transcription factors called hypoxia-inducible factors (HIFs). HIFs are regulated by prolyl hydroxylases and the asparaginyl hydroxylase factor-inhibiting HIF (FIH). Colorectal cancer is the fourth most common cause of cancer mortality worldwide and can be promoted by inflammatory bowel diseases as chronic colitis. FIH is suggested to be a tumor suppressor in colorectal cancer development by repressing the HIF-1 pathway. On the other side, epithelial HIF stabilization leads to a less severe inflammation in an acute colitis mouse model. In this work, the role of epithelial FIH in a mouse model of colitis-induced colorectal cancer was studied.

We induced chronic intestinal inflammation and colon cancer by administration of the oncogene azoxymethane (AOM, 10 mg/kg body weight, i.p.) and of dextran sodium sulfate (DSS, 1.5% in the drinking water) to $FIH^{fl/fl}$ (wildtype) and $FIH^{fl/fl}$xVillinCre (FIH knockout in colon epithelial cells) mice. Animals were treated with AOM twice and with two 5-day/one 4-day phases of DSS intermitted by regeneration times of two weeks. As an additional experiment, the pan-hydroxylase inhibitor dimethyloxalylglycine (DMOG) was administered during DSS-treatment. The disease activity index (DAI) comprising weight loss, stool consistency, and (occult) fecal bleeding was recorded and samples for molecular biological analyses were taken.

To study the interaction of FIH and its target HIF we used co-immunoprecipitation (co-IP, *in vitro*) and FRET measurements (‘*in vivo’*: cell culture). Co-IP with fluorophore-tagged HIF-1α and FIH proteins revealed the interaction *in vitro* and the usability of these constructs for *in vivo* measurements. FRET measurements with two different detection methods (seFRET and FLIM) confirmed partly the HIF-1α/FIH interaction in living cells.

In the colitis-associated colorectal cancer mouse model (knockout efficiency of FIH ~70% for whole colon mRNA), we observed a strong tumor development in the mice treated with AOM and DSS compared to control animals. Tumor occurrence did not significantly differ between $FIH^{fl/fl}$ and $FIH^{fl/fl}$xVillinCre mice. However, the $FIH^{fl/fl}$ mice showed a higher DAI compared to the $FIH^{fl/fl}$xVillinCre mice in the last DSS phase with DMOG treatment. Additionally, AOM-DSS-DMOG-treated $FIH^{fl/fl}$ mice showed a higher infiltration of macrophages than $FIH^{fl/fl}$xVillinCre mice of the same experimental group. RNAseq analysis identified an enrichment of immune response-associated GO terms. Thus, FIH knockout in colon epithelial cells seems to ameliorate the inflammatory response in chronic colitis which is possibly enhanced by temporary chemical pan-hydroxylase inhibition.

2 Zusammenfassung

Hypoxie ist ein typisches Charakteristikum für Entzündungsherde und solide Tumoren und löst eine Zellantwort auf Genexpressionsebene aus, die von Transkriptionsfaktoren kontrolliert wird, die Hypoxie-induzierbare Faktoren (HIFs) genannt werden. HIFs werden von Prolylhydroxylasen und einer Asparaginylhydroxylase namens FIH (*factor-inhibiting HIF*) reguliert. Kolorektales Karzinom ist die am vierthäufigsten auftretende Krebsart mit tödlicher Folge weltweit und kann durch chronisch entzündliche Darmerkrankungen wie Colitis *Ulcerosa* begünstigt werden. Es wird vermutet, dass FIH als Tumorsuppressor bei der Entstehung kolorektaler Karzinome durch Hemmung des HIF-1-Signalwegs wirken kann. Andererseits führt die Stabilisierung von epithelialem HIF zu einer schwächeren Entzündungsreaktion der akuten Colitis im Mausmodell. In dieser Arbeit wurde die Bedeutung von epithelialem FIH in einem Mausmodell für ein Colitis-assoziiertes kolorektales Karzinom untersucht.

Chronische Darmentzündung mit darauffolgendem Darmkrebs wurde durch Verwendung des Onkogens Azoxymethan (AOM; 10 mg/kg Körpergewicht, intraperitoneal) und Verabreichung von Dextrannatriumsulfat (DSS; 1,5% im Trinkwasser) bei $FIH^{fl/fl}$ (wildtyp) und $FIH^{fl/fl}$xVillinCre (FIH *knockout* im Dickdarmepithel) Mäusen induziert. Die Tiere wurden zweimal mit AOM und zweimal in einem 5-Tages-, einmal in einem 4-Tageszyklus mit DSS behandelt. Dazwischen lagen Regenerationszeiten von zwei Wochen. In einem zusätzlichen Experiment wurde der Pan-Hydroxylaseinhibitor Dimethyloxalylglycin (DMOG) während der DSS-Phasen eingesetzt. Der *Disease Activity Index* (DAI) wurde aufgezeichnet, welcher den Gewichtsverlust, die Stuhlkonsistenz und das Ergebnis eines Hämoccult-Tests berücksichtigt. Außerdem wurden Proben für molekularbiologische Analysen entnommen. Interaktionsanalysen zwischen FIH und seinem Substrat HIF wurden mithilfe von Co-Immunopräzipitation (Co-IP, *in vitro*) und FRET-Messungen (*in vivo*: Zellkultur) durchgeführt.

Co-IP mit Fluorophor-markiertem HIF-1α und FIH zeigte die Proteininteraktion *in vitro* und die Eignung der Konstrukte für *in vivo* Messungen. FRET-Messungen wurden in zwei unterschiedlichen Systemen durchgeführt: seFRET und FLIM und bestätigten teilweise die Proteininteraktion in lebenden Zellen.

Das Mausmodell für Colitis-assoziierte kolorektale Karzinome, in dem bei den Mäusen ein ~70%iger FIH *knockout* in mRNA aus Gesamtdarmproben festgestellt wurde, zeigte, dass AOM-DSS-behandelte Tiere im Vergleich zu unbehandelten Kontrolltieren Tumore entwickelten. Zwischen $FIH^{fl/fl}$- und $FIH^{fl/fl}$xVillinCre-Tieren waren keine Unterschiede in der Anzahl der Tumore zu beobachten. Jedoch zeigten die $FIH^{fl/fl}$-Mäuse einen höheren DAI verglichen mit $FIH^{fl/fl}$xVillinCre-Mäusen in der letzten DSS-Phase unter DMOG-Behandlung. Außerdem zeigten die AOM-DSS-DMOG-behandelten $FIH^{fl/fl}$-Tiere mehr infiltrierte

Makrophagen im Darm als FIH$^{fl/fl}$xVillinCre-Tiere derselben Behandlungsgruppe. Zusätzlich identifizierten RNAseq-Analysen eine Anreicherung von *gene ontology* Termen, die mit der Immunantwort assoziiert sind. Zusammenfassend kann gesagt werden, dass der FIH *knockout* im Kolonepithel die Entzündungsreaktionen während chronischer Colitis vermindert, was durch Behandlung mit einem chemischen Pan-Hydroxylasehemmer verstärkt werden konnte.

3 Introduction

3.1 Ulcerative colitis

Inflammatory bowel diseases (IBDs) like ulcerative colitis (UC) and Crohn's disease are inflammatory disorders that distress the gastrointestinal tract. UC specifically affects the colorectum (see Figure 3-1 A) and is common in the highly industrialized nations in North America and Europe with an annual incidence of 1 to 20 per 100,000 people (Ford *et al.*, 2013). Patients of UC suffer from abdominal pain, diarrhea, weight loss and blood in the stool with chronic relapses.

UC can be described as an excessive immune response to gut bacteria reducing epithelial barrier functions and increasing tissue damage (Coskun, 2014). Normally, the colon wall consisting of the mucosa (with the *Lamina propria*), submucosa and a muscle layer is surrounded by an epithelium (see Figure 3-1 B) that acts as a protective physical barrier. This protection can be affected by an incorrect formation of tight junctions (Schmitz *et al.*, 1999), by a diminished mucus layer which was shown in *Mucin2*-deficient mice (Van der Sluis *et al.*, 2006) or by a defective expression of antimicrobial peptides (Muniz *et al.*, 2012). All these factors can occur as a corollary or as the cause of colitis.

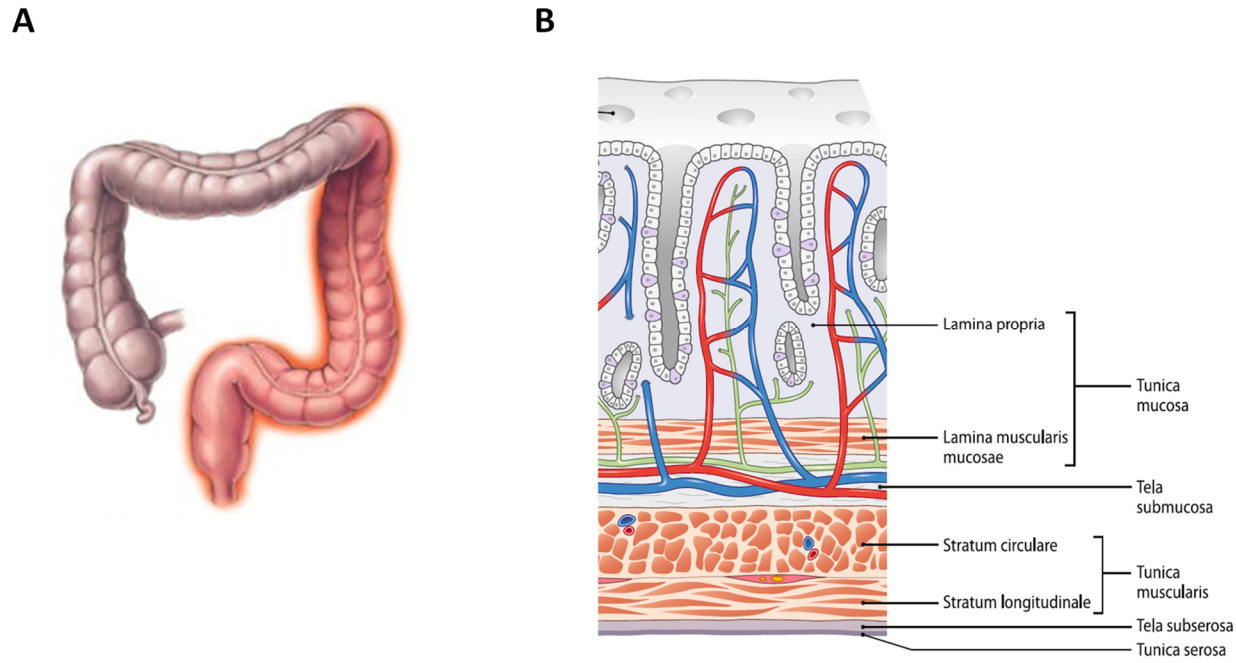

Figure 3-1: Ulcerative colitis affects the distal part of the colon. A: The parts of the colon that are affected by ulcerative colitis are highlighted in this scheme of a colon (adapted from Ungaro *et al.*, 2017). B: The colon wall is built up by several layers: Major parts are the mucosa, the submucosa and the muscle layer (*Tunica muscularis*) (adapted from Zilles, 2010).

The epithelium and mucosa in the gut contain nearly all cell types of the innate and adaptive immune system: macrophages, dendritic cells (DCs), cluster of differentiation 8a$^+$ (CD8a$^+$) and CD4$^+$ T cells, regulatory T cells and antibody-producing plasma cells (Macdonald *et al.*, 2005). Under healthy conditions, the intestinal immune system is able to adjust the response between tolerant and active as the luminal flora contains many symbiotic bacteria but can also be infested with pathogens (Xavier *et al.*, 2007).

Regulatory cytokines play a crucial role in this process as knockout mice for anti-inflammatory cytokines like interleukin-2 (IL-2) or IL-10 develop intestinal inflammation (Schultz *et al.*, 1999, Sellon *et al.*, 1998) and a blocked transforming growth factor-β (TGF-β) signaling in T cells leads to an accumulation of inflammatory cells in the *Lamina propria* of the colon (Gorelik *et al.*, 2000).

Pro-inflammatory cytokines show an increased activation in UC. IL-6, for example, is produced by *Lamina propria* macrophages and induced in experimental colitis as well as in patients with IBD (Kai *et al.*, 2005, Ogino *et al.*, 2013). Also, macrophages and T cells from IBD patients produce higher amounts of the pro-inflammatory and pro-apoptotic tumor necrosis factor (TNF), which activates nuclear factor kappa B (NF-κB) signaling, receptor interacting serine/threonine kinase 1 (RIPK1) and caspase 3 proteins (Neurath, 2014). These factors have already found their way into the clinic as TNF blocking agents show a therapeutic effect in UC (Lawson *et al.*, 2006).

3.2 Colorectal cancer

Each year, more than 1 million new cases of colorectal cancer (CRC) are diagnosed worldwide which makes the colorectum the third most frequently affected organ in matters of cancer cases after lung and breast (Stewart, 2015). In the United States the 5-year survival rate for patients diagnosed from 2006 to 2012 was about 65%. From 1975 to 2014, the death rate in the United States dropped more than half (28.6% in 1976 to 14.1% in 2014) due to treatment improvements, screening uptake and change of risk factors (Siegel *et al.*, 2017). But due to aging and growth of the population, the total number of deaths caused by CRC did not decrease remarkably.

It is a universal finding that the risk of CRC increases after suffering from IBD. It is reported for UC that the CRC incidence rises with disease duration. The risk for CRC after 10 years of UC is about 2% whereas about 20% of patients with a 30-year disease onset develop CRC (Lakatos *et al.*, 2008). Although colitis-associated CRC accounts for only 1 - 2% of all CRC cases, it is responsible for every tenth death in IBD patients (Munkholm, 2003).

Sporadic and colitis-associated CRC share the same steps of cancer development: Formation of aberrant crypt foci (ACF), polyps, adenomas and carcinomas (Terzic *et al.*,

2010). Alterations in genes and signaling pathways that lead to cancer development are also similar in sporadic and colitis-associated CRC. These genes are, for example, tumor protein p53 (*Tp53*), adenomatous polyposis coli (*Apc*), β-catenin and the Kirsten rat sarcoma viral proto-oncogene (*Kras*) (Fearon *et al.*, 1990, Terzic *et al.*, 2010). Other genes are more important only in the sporadic cancer development as cyclooxygenase 2 (*Cox2*) or in the colitis-associated cancer growth, for example nuclear factor κB (*Nfkb*). An overview of the mechanisms of CRC development is given in Figure 3-2.

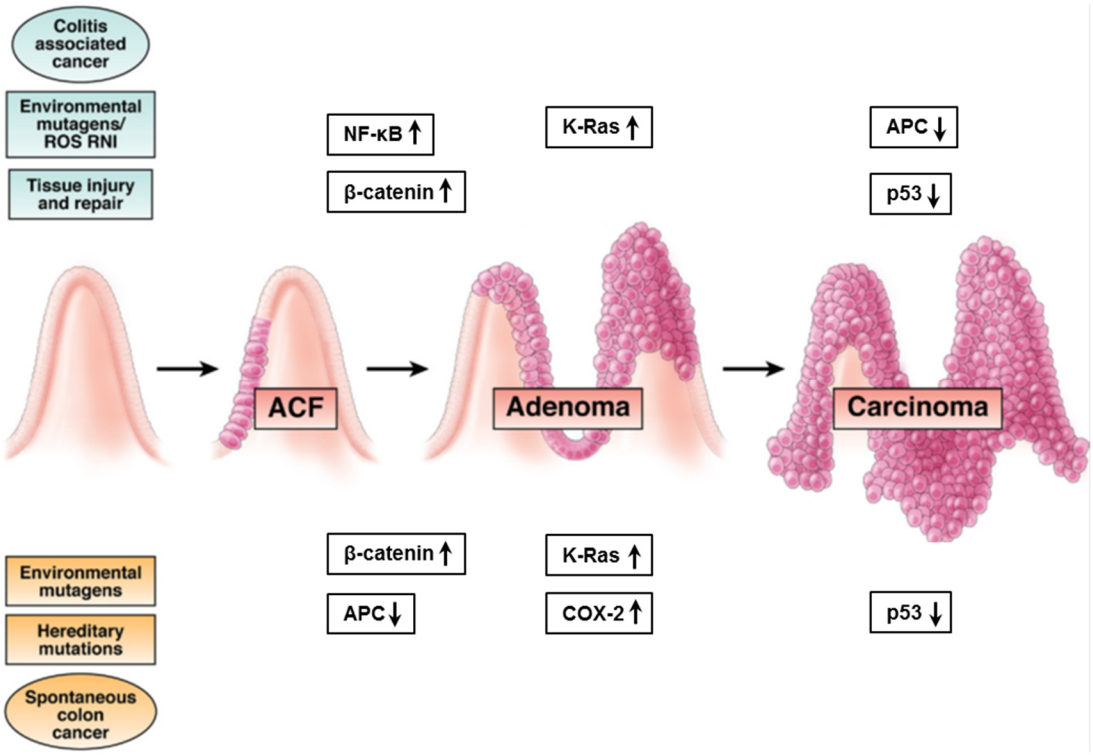

Figure 3-2: Comparison of the mechanisms of spontaneous CRC development and colitis-associated CRC (adapted and changed from Terzic *et al.*, 2010). Changes in the expression of tumor suppressor genes or oncogenes can lead to tumor development. Aberrant crypt foci (ACF) are built first, followed by formation of adenoma and carcinoma. Important genes that are typically altered in colon cancer development are β-catenin, adenomatous polyposis coli (*Apc*), Kirsten rat sarcoma viral proto-oncogene (*Kras*) and cyclooxygenase 2 (*Cox2*). In colitis-associated cancer, changes in nuclear factor κB *(Nfkb)* signaling are also important.

One factor of intestinal inflammation that promotes colorectal cancer is the release of pro-inflammatory cytokines, which is described above. IL-6 activates the signaling pathway of Janus kinase (JAK)/ signal transducer and activator of transcription (STAT) protein resulting in promoting tumor growth and inhibiting cell apoptosis (Becker *et al.*, 2005). TNF-α induces the production of COX-2, which is important for cell proliferation and angiogenesis (Agoff *et al.*, 2000). Furthermore, intestinal inflammation modifies the microbiome. Colibactin is a toxin

produced by bacteria that induces DNA damage, a main cause for cancer development. In inflammatory bowel diseases, Colibactin producing microbes are expanded in the microbiota and the inflamed tissue enables the bacteria to access the epithelium, as the barrier function of the mucosa is decreased (Arthur *et al.*, 2012). DNA damage is also caused by reactive oxygen species whose production is promoted by pro-inflammatory cytokines (Lopez *et al.*, 2018).

To study the molecular events and the disease progress of UC, the dextran sulfate sodium (DSS) mouse model is well established. Colitis is induced in the animals by administration of DSS via the drinking water (1% - 5%) for several days and was – according to Clapper *et al.* (2007) – originally described by Ohkusa (1985) in a Japanese journal. DSS destroys the barrier function of the *Tunica mucosa* and enables the invasion of pathogens resulting in an inflammation (Okayasu *et al.*, 1990). Chronic colitis with active and inactive disease states is mimicked by repeated DSS cycles followed by phases of normal drinking water. About 20% of the animals that underwent four 7-day cycles of 4% DSS treatment developed colorectal tumors. To transform this model into an efficient model for colitis-associated CRC development in terms of CRC incidence, survival rate and experiment duration, the administration of a carcinogen (e.g. azoxymethane (AOM)) was added. DSS and AOM in combination led to 100% incidence of colonic tumors while lowering the number of DSS cycles, their duration and the DSS concentration (1% - 2%), which is more acceptable for a mouse experiment (Clapper *et al.*, 2007, Tanaka *et al.*, 2003). Besides carcinogen administration, there are also genetical strategies to induce colitis-associated CRC in a mouse model: DSS treatment is then used in mice carrying a mutation in the tumor suppressor gene *Apc* ($Apc^{Min/+}$) (Tanaka *et al.*, 2006) or in p53 deficient mice ($p53^{-/-}$) (Fujii *et al.*, 2004, Chang *et al.*, 2007).

One of the characteristics of solid tumors is tumor hypoxia, which means that regions of the tumor microenvironment show much lower oxygen levels than the correspondent tumor-free tissue (Hockel *et al.*, 2001). Major causes for tumor hypoxia are non-functional or disorganized blood vessels, especially in rapidly growing tumor tissue (Wigerup *et al.*, 2016), or the increased diffusion distance for oxygen with tumor expansion (Vaupel *et al.*, 2004). Tumor hypoxia is associated with resistance to radiation as reviewed by Bertout *et al.* (2008) who specifically addressed the first radiation studies in normal mammalian cells under hypoxia in the early 20th century by Churchill-Davidson *et al.* (1955). Many different aspects of cancer cell progression are affected by tumor hypoxia like cell proliferation, metabolism, immune response, apoptosis and genomic instability (Wigerup *et al.*, 2016). These processes are regulated by the expression of certain genes which are in turn dependent on transcription factors. Active transcription factors during hypoxia are the hypoxia-inducible factors (HIFs).

In colitis-associated CRC, not only tumor hypoxia can activate HIFs but also the inflammatory response itself. The expression of HIFs is then regulated by NF-κB (Bonello *et al.*, 2007, van Uden *et al.*, 2008, Frede *et al.*, 2006).

3.3 The hypoxia-inducible factors (HIFs) – expression, regulation and inhibitors

Cellular adaptation to hypoxia is dependent on the activity of HIFs. HIFs regulate the expression of several target genes which makes the survival of cells at low oxygen levels possible. These target genes are, for example, vascular endothelial growth factor (*Vegf*), the glucose transporter 1 (*Glut1*), erythropoietin (*Epo*) or phosphoglycerate kinase 1 (*Pgk1*). They are all part of the survival strategies of an organism to overcome hypoxia and therefore ATP shortage by inducing angiogenesis, glycolysis or erythropoiesis (Wenger, 2002).

HIFs are heterodimers consisting of the two subunits HIF-α and HIF-β, also named ARNT (aryl hydrocarbon receptor nuclear translocator). ARNT is constitutively expressed, while HIF-α stabilization is oxygen-dependent. The transcriptional activity is only present after the formation of a dimer of an α- and a β-subunit (ARNT) (Wang *et al.*, 1995b). HIF-α has three isoforms: HIF-1α, HIF-2α and HIF-3α. The function of HIF-3α is not resolved yet, but HIF-1α and HIF-2α both form heterodimers with ARNT and are transcriptionally active under hypoxia (Wenger, 2002). HIF-1α and -2α have different expression patterns. While HIF-1α is expressed ubiquitously throughout all organs, HIF-2α expression is limited on endothelium in general, kidney, heart, lungs and small intestine (Ema *et al.*, 1997, Tian *et al.*, 1997).

HIF-1α, HIF-2α and ARNT have similar protein structures (see Figure 3-3). The basic helix-loop-helix (bHLH) domain binds hypoxia-responsive elements (HREs) on the DNA. A Per-Arnt-Sim (PAS) domain makes interaction between the subunits possible (Wang *et al.*, 1995a). The α-subunit then has an oxygen-dependent degradation domain (ODD), which contains two proline residues that can be hydroxylated for HIF regulation (Huang *et al.*, 1998). HIF-α has two transactivation domains: an N-terminal (N-TAD) and a C-terminal (C-TAD) one (Jiang *et al.*, 1997). The C-TAD domain is responsible for the binding of co-activators like p300 and the CREB binding protein (CBP) and can be hydroxylated at an asparagine residue to inhibit the interaction with these co-activators.

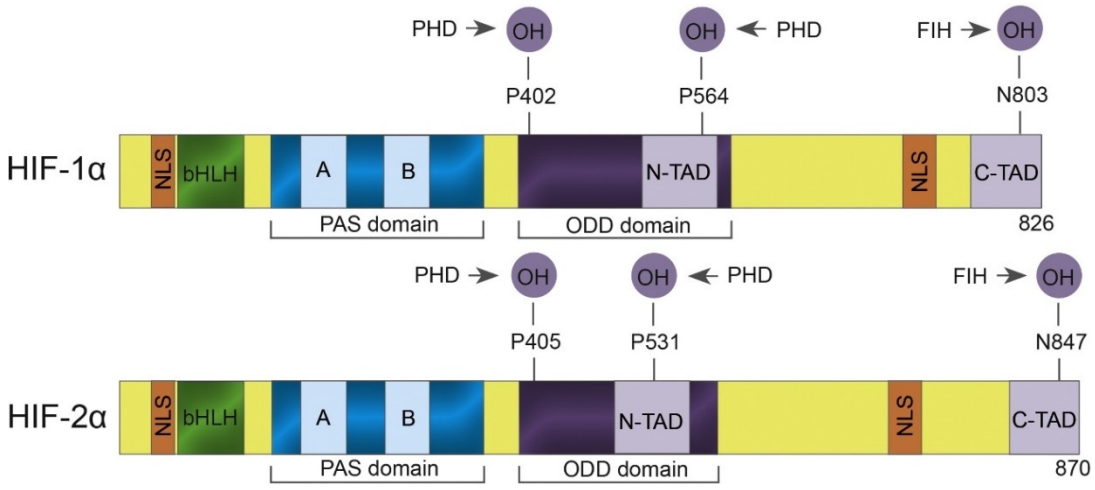

Figure 3-3: Structure of the HIF subunits HIF-1α and HIF-2α (adapted from Wigerup *et al.*, 2016). HIF-1α and HIF-2α share the same domain structure: The nuclear localization sequences (NLS), the bHLH and PAS domain as well as ODD, C-TAD, N-TAD are illustrated in this schema. The hydroxylation sites that enable the hydroxylases PHD1-3 and FIH to regulate the HIF-α protein are also highlighted.

If the proline residues in the ODD (HIF-1α: Pro402 and Pro564, HIF-2α: Pro405 and Pro531 in humans) are hydroxylated by prolyl hydroxylases (PHD1-3), the HIF-α subunit is marked for proteasomal degradation (see Figure 3-4) (Fandrey *et al.*, 2006). These hydroxylation reactions constitutively take place under normoxia. Oxygen as well as α-ketoglutarate are needed as co-substrates in this reaction which makes the enzyme oxygen-dependent. The hydroxylated proline residues are recognized by the von-Hippel-Lindau protein (pVHL) which then binds the α-subunit and starts ubiquitination, as it is part of an E3 ubiquitin ligase (Maxwell *et al.*, 1999). The poly-ubiquitinylated α-subunit is then proteasomally degraded. Under hypoxia, the PHDs are inhibited due to the lack of oxygen and HIF-α can accumulate and translocate into the nucleus where it finds and binds its partner ARNT for dimerization. Subsequently, dimerized HIF in the nucleus can induce the cellular answer to hypoxia. *Phd2* and *3* belong to the target genes of HIF resulting in a negative feedback loop (del Peso *et al.*, 2003).

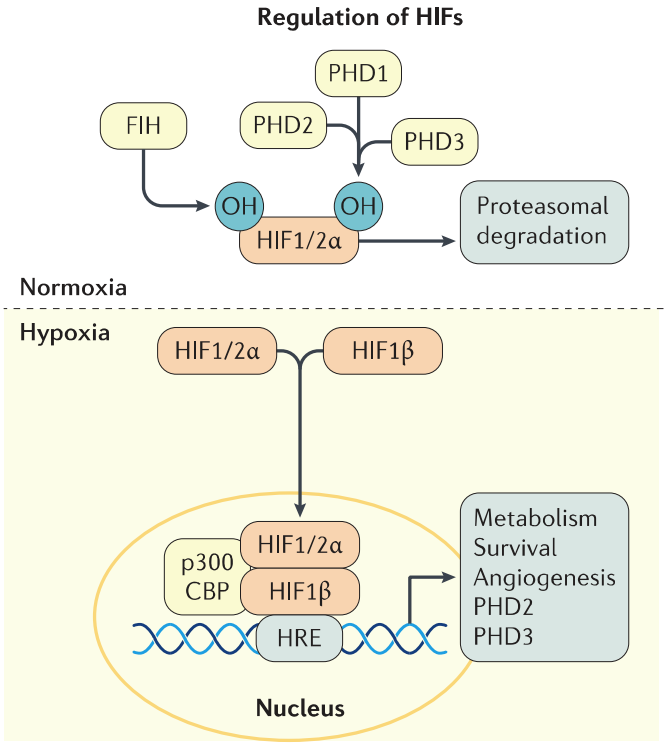

Figure 3-4: Regulation of HIFs by PHDs. Schema for proteasomal HIF degradation under normoxia (adapted from Van Welden *et al.*, 2017). PHD1-3 hydroxylate the HIF-α subunit under normoxia and mark it for proteasomal degradation. Under hypoxia, HIF-α can translocate into the nucleus and form a dimer with HIF-β (ARNT). FIH hydroxylation leads to the inhibition of HIF interaction with p300/CBP under normoxia. The complex of HIF with p300/CBP binds hypoxia-responsive elements (HREs) on the DNA inducing a cellular response to the hypoxic environment.

An additional way to inhibit HIF activity in normoxia is to hydroxylate an asparagine residue in the C-TAD domain (HIF-1α: Asn803, HIF-2α: Asn847). The factor-inhibiting HIF (FIH or FIH-1; also HIF1AN) uses oxygen and 2-oxoglutarate for its enzymatic activity making FIH oxygen-dependent as well (Lando *et al.*, 2002a, Lando *et al.*, 2002b). The hydroxylated asparagine prevents the recruitment of the co-activators p300/CBP and the expression of C-TAD-dependent genes is then inhibited.

Besides hypoxia, which prevents hydroxylation by the lack of the co-substrate oxygen, the hydroxylases can be inhibited chemically. One pan-hydroxylase inhibitor that is used in experiments to block hydroxylase activity is dimethyloxalylglycine (DMOG) (Jaakkola *et al.*, 2001, Lando *et al.*, 2002b). This 2-oxoglutarate analog acts as a competitive inhibitor for all 2-oxoglutarate-dependent hydroxylases such as PHD and FIH. Therefore, it can be used in animal models and experimental cell cultures to study the effect of a constitutive HIF activity on all sorts of scientific questions.

3.4 The factor-inhibiting HIF (FIH) and its metabolic impact

FIH is a 2-oxoglutarate-dependent asparaginyl hydroxylase that is active as a homodimer (Lancaster *et al.*, 2004). Its eponymous substrate is HIF-α, which is hydroxylated and therefore inhibited by FIH. FIH is a cytoplasmic protein (Linke *et al.*, 2004) that enters the nucleus together with its substrate HIF-1α under hypoxia via HIF-1α-dependent binding to importin beta-1 (Wang *et al.*, 2018, Liang *et al.*, 2015). Under catalytic inhibition as under hypoxia, or with increased hydroxylation status of Asn803, this nuclear entry is even enhanced (Wang *et al.*, 2018).

The enzyme properties of FIH differ from those of the HIF prolyl hydroxylases. FIH is still active at low oxygen tensions when the PHDs are already inhibited. This difference can be quantified by the K_m values for O_2. The K_m value for FIH is 90 µM ± 20 µM (Koivunen *et al.*, 2004) whereas the K_m for the PHDs is in the range of 230 to 250 µM (Hirsila *et al.*, 2003). The importance of this second regulatory system for a HIF-dependent transcriptional response to hypoxia was determined by using pan-hydroxylase and PHD-specific inhibitors: the broad inhibitors could imitate the cellular hypoxic response better than the more selective ones (Chan *et al.*, 2016). It was found that FIH acts more efficiently on HIF-1α than HIF-2α peptides, leading to a potentially higher effect of FIH inhibition on HIF-1 than HIF-2 target genes (Koivunen *et al.*, 2004).

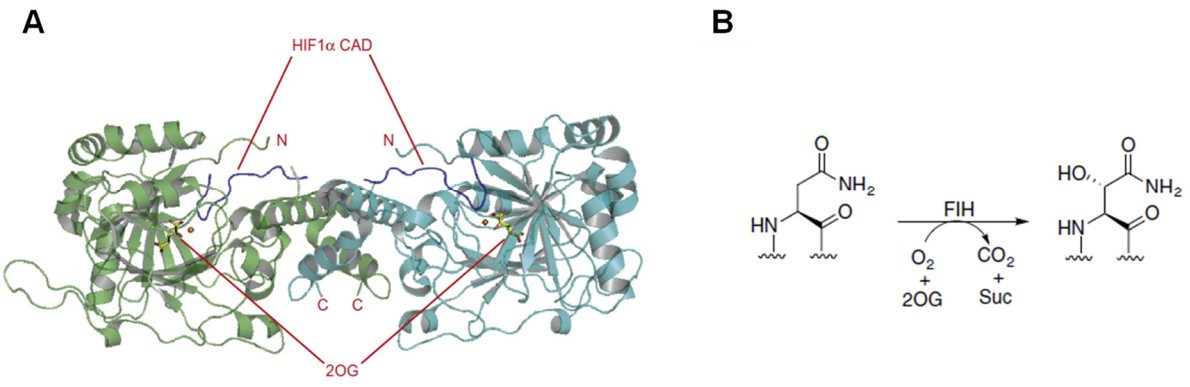

Figure 3-5: Crystal structure and hydroxylation reaction of the FIH dimer (adapted from Chan *et al.*, 2016). A: The crystal structure of the FIH dimer shows the binding sites for HIF-1α C-TAD and for the co-substrate 2-oxoglutarate (2OG). B: Hydroxylation reaction of an asparagine residue of HIF-1α catalyzed by FIH. 2-oxoglutarate (2OG) and oxygen (O_2) are needed as co-substrates, succinate (Suc) and carbon dioxide (CO_2) are produced.

Mice with a null mutation in the *Fih* gene were well studied by Zhang *et al.* (2010) with regard to the regulation of metabolism. Mice lacking FIH showed a higher respiratory frequency and

lower plasma EPO levels under/post hypoxia, an increased consumption of oxygen as well as of food and water while having a lower body mass throughout life (Zhang *et al.*, 2010). Furthermore, different metabolic changes could be observed in experiments with murine embryonic fibroblasts (MEFs) lacking FIH. Cells without FIH had a greater capacity to increase glycolysis when oxidative metabolism was interrupted. The FIH loss accelerated oxidative processes and increased the respiratory capacity. This is different in pVHL loss and therefore FIH specific which means it might be independent from the HIF pathway (Sim *et al.*, 2018). ATP levels in these cells were increased while cell growth was somewhat decreased (Zhang *et al.*, 2010).

To understand the influence of HIF hydroxylases on the whole organism, it is important to consider not only the effects of HIF but also alternative targets for PHDs and FIH. It is known that PHDs and FIH hydroxylate several other proteins and can change their activation statuses and interaction capabilities.

For PHDs, the alternative targets p53 (Ullah *et al.*, 2017, Deschoemaeker *et al.*, 2015, Rodriguez *et al.*, 2018), mitogen-activated protein kinase 6 (MAPK6) (Rodriguez *et al.*, 2016), forkhead box O3 (FOXO3a) (Zheng *et al.*, 2014), inhibitor of NF-κB kinase (IKK)-β (Cummins *et al.*, 2006, Zheng *et al.*, 2014) and centrosomal protein (Cep)192 (Moser *et al.*, 2013) were identified, mostly by immunoprecipitation and mass spectrometry. These proteins are important actors in tumor suppression, cell cycle and proliferation, angiogenesis and the NF-κB pathway.

It has been proven that there are also alternative targets for the asparaginyl hydroxylase FIH. These are, by now, the ovarian tumor domain containing ubiquitin aldehyde binding protein 1 (OTUB1) (Scholz *et al.*, 2016), the NF-κB precursor p105 and inhibitor of kappa B (IκB)α (Cockman *et al.*, 2006) and receptor-interacting serine/threonine-protein kinase 4 (RIPK4) (Rodriguez *et al.*, 2016). All FIH targets share a common domain, the ankyrin repeat domain (ARD). As the ARD occurs in a large number of diverse proteins, it is likely that several more targets of FIH will be found soon as technical possibilities for large-scale screenings have improved impressively over the last years.

3.5 HIFs in inflammation and cancer

The intestinal epithelium is hypoxic under physiological conditions with pO_2 values of <15 mmHg (luminal) up to 23 mmHg (epithelial border to the submucosa) (Van Welden *et al.*, 2017). These oxygen partial pressures correspond to a concentration of about 2 - 3% of oxygen in the air. Hypoxic regions are even extended during inflammation as it was shown in mouse models of colitis (Karhausen *et al.*, 2004, Fluck *et al.*, 2016). This decrease of the oxygen partial pressure during inflammation is caused by additional oxygen consumption due

to a high amount of infiltrating immune cells (Campbell *et al.*, 2014) and by a reduced bloodstream due to thrombosis (Hatoum *et al.*, 2003).

As hypoxia is an important side effect of IBD, the role of HIFs and PHDs in different intestinal cell types is well studied. Epithelial HIF-1 and -2 were shown to be protective in experimental mouse models of colitis (Karhausen *et al.*, 2004). This protection is supposedly possible by preserving intestinal barrier functions as some barrier-protective genes belong to the HIF target genes. Innate and adaptive immune cells infiltrate the center of inflammation and are exposed to hypoxia as well. Therefore, infiltrating macrophages, for example, lacking HIF-1α, were shown to endure the hypoxic environment to a lesser extent than HIF-1α expressing macrophages, as they are not able to produce a sufficient quantity of ATP (Cramer *et al.*, 2003). In a murine colitis model, knockdown of HIF-1α in myeloid cells including macrophages ameliorated the disease progress (Backer *et al.*, 2017). In DCs, loss of HIF-1α leads to reduced expression of chemokines which usually facilitate the recruitment of regulatory T cells. Thus, mice lacking HIF-1α in DCs are more susceptible to colitis (Fluck *et al.*, 2016).

Deletion of PHDs also affects the IBD progress in mice. Epithelial PHD3 plays a protective role for the intestinal barrier function and its deletion can even cause spontaneous colitis (Chen *et al.*, 2015b). Within the inflamed environment of patients with ulcerative colitis, the number of PHD3-positive macrophages increased as well as the intensity of PHD3 staining (Escribese *et al.*, 2012). DMOG treatment in mouse models ameliorated colitis (Cummins *et al.*, 2008). The protective effects of this pan-hydroxylase inhibitor were also found in ileitis (Hindryckx *et al.*, 2010) and radiation-induced intestinal injuries (Taniguchi *et al.*, 2014).

In cancer, HIF is known to be activated intratumorally to mediate tumor cell adaptation to the low oxygen availability by inducing angiogenesis and increasing the flux through the glycolytic pathway for ATP production (Semenza, 2013). Several other metabolic pathways are also known to be altered by hypoxia and HIF, e.g. glycogen biosynthesis, glutamine metabolism, lipid synthesis and redox stress (Xie *et al.*, 2017). In general, HIF target gene induction promotes cancer progression and increased HIF protein levels are associated with decreased patient survival in many different cancer types (Semenza, 2010). The effects of hypoxia and therefore HIF stabilization in cancer are summarized in Figure 3-6. Furthermore, the tumor protein p53 was shown to co-precipitate and therefore associate with HIF-1α suggesting that hypoxic induction of p53 transcriptional activity is caused by p53 stabilization due to the association with HIF-1α (An *et al.*, 1998). But the molecular mechanism was unknown and the direct interaction of p53 with HIF-1α was challenged. It was then found that p53 and HIF are connected via the HIF co-activators p300/CBP, which play a significant role in p53 signal transduction (Grossman, 2001). Another bridge for the impact of HIF-1α on p53 stability was then found in the E3 ligase mouse double minute 2

homolog (Mdm2). Mdm2 directly binds to HIF-1α and might hence be kept from ubiquitinating p53, which would result in proteasomal degradation of p53 (Chen *et al.*, 2003). Putting these mechanisms into a computational model for p53 activation by HIF-1 upon hypoxia, Wang *et al.* (2019) showed a remarkable contribution of HIF-1α expression on p53 stabilization. The model also revealed the impact of FIH expression on p53: Transcriptional activity of HIF-1 is needed for p53 stabilization and p53 levels increased with FIH inhibition (Wang *et al.*, 2019).
As inflammation and cancer development are closely connected, the activity of HIF in immune cells also has an effect on tumor growth. Loss of HIF-1α in $CD8^+$ T cells led to an acceleration in tumorigenesis and alterations in tumor vascularization, similar to VEGF-A deficiency (Palazon *et al.*, 2017). In a mouse model of CRC with APC deficient mice, epithelial HIF-2α facilitated the tumor progression by recruiting neutrophils (Triner *et al.*, 2017). As FIH inactivates HIF and reduces the cancer promoting effects it is suggested to be a tumor suppressor. In human CRC tissues, downregulation of FIH defined a poor prognosis of CRC and low mRNA levels of FIH correlated with CRC depth of invasion, contribution of lymph nodes and formation of metastases (Chen *et al.*, 2015a).

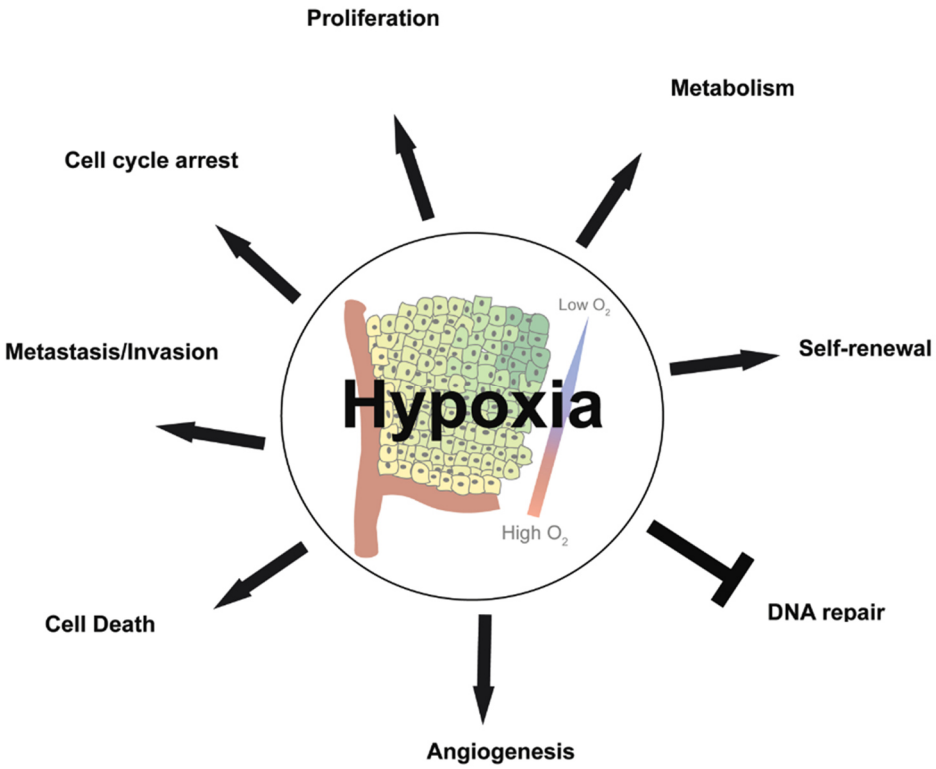

Figure 3-6: Effects of HIF accumulation regarding tumor metabolism (adapted and changed from Henze *et al.*, 2010). Tumor hypoxia affects tumor cells by activation of HIF. This results in increased metabolism, proliferation, angiogenesis, cell-death and self-renewal with less DNA repair mechanisms. These processes can promote metastasis and invasion.

4 Aim of the study

Colorectal cancer is one of the most lethal cancer diseases worldwide. Chronic inflammatory bowel diseases like ulcerative colitis can promote tumor development in the colon. To date, the connection between inflammation and tumor growth are inadequately understood. More detailed knowledge about this process could lead to new therapeutic approaches.

In both diseases, inflammation and solid tumors, hypoxia-inducible factors (HIFs) are active. HIFs regulate the cellular answer to hypoxic stress and enable the adaptation of processes like angiogenesis, erythropoiesis, and glycolysis to low oxygen levels. HIF-1α in epithelial and myeloid cells is supposed to act in a protective way in inflammatory bowel diseases. The same applies to the treatment with pan-hydroxylase inhibitors like DMOG and FG-4497 which was shown in mouse models of colitis. This protective effect of HIFs could also result in a lower risk of developing colorectal cancer after a chronic colitis. But it is suggested that FIH is a tumor suppressor in human colorectal cancer development by repressing the HIF-1α pathway. Patients, whose colorectal cancer tissue showed downregulated FIH protein level had a poor prognosis with lower chance of survival. This reveals the need to study the role of HIFs and their inhibitor FIH in a model of colitis-induced colorectal cancer.

Therefore, the AOM-DSS mouse model is used to simulate a chronic colitis resulting in tumor development. Mice with an epithelial knockout of FIH in the colon will be compared to wildtype siblings in terms of disease progress, inflammatory response and tumor growth. RNA, protein and immunohistochemical analyses will be done to gain insights on the molecular level. The same experiment will also be done with DMOG treatment during colitis to possibly strengthen the effect of the FIH knockout by increasing the amount of stabilized HIF-α.

Additionally, the interaction of HIFs and FIH as well as potential further partners is to be studied *in vitro* (co-immunoprecipitation) and *in vivo* (cell culture, microscopically). For the latter, FRET measurements in HEK293T and U2OS cells, which are transfected with constructs coding for fluorophore-linked proteins (HIF-α, HIF-β/ARNT, and FIH), will be carried out using sensitized emission FRET and FLIM.

5 Materials and methods

5.1 Experimental animals

Animal experiments were carried out with laboratory mice with a mixed C57/Bl6/129/FVB background. The epithelial knockout of FIH was induced by the Cre/loxP system, in which exon 2 of the *Fih* gene is flanked by loxP-sites on both alleles ($FIH^{fl/fl}$). $FIH^{fl/fl}$ mice were then mated with mice carrying the gene for the Cre recombinase (heterozygous Cre expression: $Cre^{+/-}$), combined with the Villin promoter for colon epithelial specificity (VillinCre) (Madison *et al.*, 2002). The resulting offspring has then an epithelial knockout of FIH ($FIH^{fl/fl}$xVillinCre) or is wildtype regarding the expression of Cre recombinase ($FIH^{fl/fl}$). $FIH^{fl/fl}$ mice were kindly provided by Sir Peter J. Ratcliffe and were first described by Zhang *et al.* (2010).

During the experiment, mice were kept individually and pathogen-free in Sealsafe NEXT Type II cages, at 20 °C and a 12 hrs day and night rhythm at the Central Animal Laboratory, University Hospital Essen. Food pellets and drinking water were given *ad libitum*, except described differently for experimental reasons.

The animal experiments were permitted by the State Agency for Nature, Environment, and Consumer Protection of North Rhine-Westphalia (LANUV NRW) under the file numbers 84-02.04.2013.A085 and 81-02.04.2018.A114.

5.2 Laboratory equipment

The laboratory equipment used in the experiments for this work is listed in Table 5-1.

Table 5-1: Laboratory equipment/kits and its producers.

Equipment	Producer
Automatic tissue dehydration machine	RWW Medizintechnik
Axiovert 200M	Zeiss
Centrifuge	Eppendorf
Clean bench HERA Safe	Heraeus Instruments
CSA II	Dako
Culture microscope CK40	Olympus
DAB Kit	Vector
DNA Clean & Concentrator	Zymo Research
ECL detection system (SuperSignal™ West Femto)	Thermo cientific
Electrophoresis power supply	Bio-Rad
Epoch™ Microplate Spectrophotometer (Take3 plate)	BioTek
FACSCanto™ II flow cytometer	BD

Fusion-FX7	Peqlab
Homogenizer	Polytron
Hypoxyprobe-1™ (MAb) Kit	Hypoxyprobe
iCycler iQ5™	Bio-Rad
Incubator	Heraeus Instruments
innuPREP Plasmid Mini Kit	Analytik Jena
Leica TCS SP8 microscope	Leica
Mastercycler	Eppendorf
Nitrocellulose membrane (0.2 µm)	Schleicher&Schuell
NucleoSpin® RNA	Machery-Nagel
Pipette	Eppendorf
PureYield™ Plasmid Midi Kit	Promega
RNAscope® 2.5 HD Detection Kit (BROWN)	Advanced Cell Diagnostics
Rotary Microtome Microm HM 340E	Thermo Scientific
Aperio ScanScope® CS2	Aperio
TCSPC module PicoHarp 300	PicoQuant
Thermo Cycler	Biometra
UV desk (BioDoc-It™ Imaging System)	UVP
Vectastain ABC-Elite Standard-Kit	Vector Laboratories
Vortexer	Scientific Industries
Western Blot chamber Mini Trans-Blot®	Bio-Rad
X-ray developer machine (Curix 60)	AGFA
ZymoClean™ Gel DNA Recovery Kit	Zymo Research

5.3 Consumables and chemicals

All used consumables and chemicals are listed in Table 5-2.

Table 5-2: Used consumables and chemicals in this work.

Consumable/chemical	**Producer**
(Filter) tips (2.5 µL, 20 µL, 200 µL, 1000 µL)	Sarstedt
µ-Slide 8 well	ibidi
4-(2-hydroxyethyl)-1-piperazineethanesulfonic acid (HEPES)	AppliChem
Acetic acid	AppliChem
Agarose	AppliChem
Ammonium hydroxide	Sigma-Aldrich
Ammonium persulfate (APS)	Bio-Rad
Antibody diluent	Dako

Antigen retrieval (10X)	Dako
Azoxymethane (AOM)	Sigma-Aldrich
Bisacrylamide (30%)	Bio-Rad
Blue S'Green qPCR Kit	Biozym
Bovine serum albumin (BSA)	PAA
Bromphenol blue	Sigma-Aldrich
Calf intestinal phosphatase	New England Biolabs
Cell culture flask (T25 & T75)	Sarstedt
Cell plate (6-well)	Sarstedt
Cell plate (96-well skirted, protein assay)	4-titude
Cell plate (96-well without skirt, qPCR)	Sarstedt
Cell strainer (70 µm)	Falcon
Conical centrifuge tube (15 / 50 mL)	Sarstedt
Cover slips	Engelbrecht
CutSmart® (10X)	New England Biolabs
Dextran sodium sulfate (DSS)	MP-Biomedicals
Diethyl pyrocarbonate (DEPC)	Sigma-Aldrich
Dimethyl sulfoxide (DMSO)	Sigma-Aldrich
Dimethyloxaloylglycine (DMOG)	Biomol
Dithiothreitol (DTT)	Sigma-Aldrich
DNA ladder (100 bp)	Invitrogen
dNTPs	Promega
D-sorbitol	Sigma-Aldrich
Dulbecco's Modified Eagle Medium (DMEM)	Gibco
Eclipse needle (0.4 mm x 19 mm)	BD
Embedding cassettes	Roth
Entellan®	Merck
Eosin Y	Sigma Aldrich
Ethanol	VWR
Ethidium bromide	Sigma-Aldrich
Ethylene glycol-bis(β-aminoethyl ether)tetraacetic acid (EGTA)	Fluka
Ethylenediaminetetraacetic acid (EDTA)	Merck
Fetal calf serum (FCS)	Biochrom AG
GFP-traps	Chromotek
Glucose	Merck
Glycine	Sigma-Aldrich
GoTaq G2 polymerase	Promega
GoTaq reaction buffer (5X)	Promega
Guanidinium thiocyanate (GTC)	Roth

H_2O_2 (30%)	Merck
Hematoxylin	Merck
Hemoccult test (hema-screen™)	Immunostics. inc.
Isopropanol	AppliChem
Kanamycin	Calbiochem
Lipofectamine™ 3000 (+ P3000 reagent)	ThermoFisher
Lithium chloride (LiCl)	AppliChem
Live Cell Fluorescence Imaging Medium, FluoroBrite™ DMEM	Thermo Fisher
Methanol	Sigma-Aldrich
Milk powder	DNG Farmland
Nonidet® P40 (NP40)	AppliChem
Normal goat serum	Invitrogen
Normal rabbit serum	Invitrogen
Oligo-dT primers	Invitrogen
Paraffin	McCormick Scientific
Paraformaldehyde (PFA)	Sigma-Aldrich
Penicillin/streptavidin (10000 U/mL)	Invitrogen
Phenol	AppliChem
Phenol:chloroform:isoamyl alcohol mixture	AppliChem
Phenylmethylsulfonyl fluoride (PMSF)	Sigma-Aldrich
Ponceau S solution	Sigma-Aldrich
Potassium chloride (KCl)	Applichem
Potassium hydrogen phosphate (KH_2PO_4)	Merck
Proteinase inhibitor (PI) (Complete Mini EDTA-free)	Sigma-Aldrich
Reaction tube (0.5 mL safe-lock)	Eppendorf
Reaction tube (1.5 / 2 mL)	Sarstedt
Reagent A and B (protein assay)	Bio-Rad
M-MLV reverse transcriptase (RT)	Promega
M-MLV RT reaction buffer (5X)	Promega
Serological pipettes (5 mL, 10 mL, 25 mL)	Greiner Bio-One
Serum-free protein block	Dako
Sodium acetate (NaOAc)	Sigma-Aldrich
Sodium azide	Applichem
Sodium chloride (NaCl)	Fluka
Sodium deoxycholate	Sigma-Aldrich
Sodium dodecyl sulfate (SDS)	Sigma-Aldrich
Sodium fluoride (NaF)	Fluka
Sodium hydrogen phosphate (Na_2HPO_4)	Fluka
Sucrose	Merck

Superfrost™ microscope slides	Thermo Scientific
Syringe (1 mL)	BD
T4 ligase	New England Biolabs
T4 ligase buffer	New England Biolabs
Tetramethylethylenediamine (TEMED)	Sigma-Aldrich
Tris(hydroxymethyl)-aminomethane (Tris)	AppliChem
Triton-X 100	Sigma-Aldrich
Trypsin (0.5% / 10X)	Gibco
Tryptone	Sigma-Aldrich
TurboFect™	ThermoFisher
Tween 20	Roth
XL10 Gold bacteria	Agilent Technologies
X-ray film 100 NF 13x18	FUJIFILM
Xylene	Roth
Yeast extract	AppliChem
β-mercaptoethanol	Merck

5.4 Media and solutions

The formulas for the solutions and media used in this study can be found in Table 5-3.

Table 5-3: Formulas of the media and solutions that were used in this work.

Solution	Formula
10X PBS	137 mM NaCl 2.7 mM KCl 10 mM Na_2HPO_4 2 mM KH_2PO_4 pH 7.4
10X TBS (immunohistochemistry)	301.4 mM NaCl 50 mM Tris pH 7.6
10X TBS (Western Blot)	137 mM NaCl 20 mM Tris pH 7.6
1X TBS-T (immunohistochemistry)	1X TBS 0.1% Tween 20
1X TBS-T (Western Blot)	1X TBS 0.05% Tween 20
4X Lower buffer (SDS-PAGE)	1.5 M Tris 13.9 mM SDS pH 8.8
4X SDS buffer	200 mM Tris pH 6.8 8% SDS 10% β-mercaptoethanol 0.02% Bromphenol blue

	40% Glycine
4X Upper buffer (SDS-PAGE)	251 mM Tris 6.9 mM SDS pH 6.8
Blotting buffer	25 mM Tris 96 mM Glycine 20% Methanol
Chelating buffer	96.2 mM NaCl 1.6 mM KCl 5.6 mM Na_2HPO_4 8 mM KH_2PO_4 43.4 mM Sucrose 54.9 mM D-sorbitol 0.5 mM DTT
Chelating buffer containing EDTA	2 mM EDTA in chelating buffer
Colon lysis buffer	150 mM NaCl 5 mM KCl 10 mM Hepes 0.5 mM EDTA 0.2 mM EGTA 1 mM NaF 1 mM DTT 0.05% NP40 10% Proteinase inhibitor
Culture medium	10% FCS 1% Penicillin/streptavidin in DMEM
DEPC water	0.1% DEPC in H_2O
FACS buffer	1X PBS 0.1% FCS 0.02% Sodium azide
GTC solution (4M)	4 M GTC 250 mM NaOAc 0.75% β-mercaptoethanol in DEPC water
Lysis buffer (Co-IP)	10 mM Tris 150 mM NaCl 0.5 mM EDTA 0.1% SDS 1% Triton-X 1% Sodium deoxycholate 1 mM PMSF 10% Proteinase inhibitor
Lysogeny broth (LB) medium	5 wt% Tryptone 5 wt% NaCl 5 wt% Yeast extract
NaOAc (2M)	2M NaOAc pH 4.0
NaOAc (3M)	3M NaOAc pH 5.2
Protein lysis buffer	20 mM Tris 150 mM NaCl

	1% NP40 5 mM EDTA
Running buffer (SDS-PAGE, 10X)	25 mM Tris 192 mM Glycine 3.5 mM SDS
Super optimal broth (SOB) medium	20 w% Tryptone 5 w% Yeast extract 0.5 w% NaCl 0.186 w% KCl 0.02 M Glucose
TAE buffer	40 mM Tris 0.11% Acetic acid 1 mM EDTA pH 8.0
Washing buffer (Co-IP)	10 mM Tris 150 mM NaCl 0.5 mM EDTA 1 mM PMSF

5.5 Mouse model of colorectal cancer (AOM-DSS)

The azoxymethane (AOM), dextran sodium sulfate (DSS) model is a mouse model to simulate a chronic colitis connected to colorectal cancer development. The carcinogen AOM induces colorectal tumorigenesis by introducing DNA damage specifically in the colon and allows the usage of a low DSS dosage compared to a colorectal cancer induction by DSS administration alone.

$FIH^{fl/fl}$ and $FIH^{fl/fl}$xVillinCre mice, which were at least 12 weeks old, were individualized and 10 mg AOM per kg body weight in sterile PBS (100 µL total volume) were injected intraperitoneally (i.p.). After five days, the first DSS phase started: 1.5% DSS were given in the drinking water for five days renewing the DSS on day 3. Eleven days of regeneration later, AOM and another five days later DSS were administered again, repeating the first phase of AOM and DSS exactly. After 16 days of regeneration, the last phase of DSS started, which only took four days. During the DSS phases and five to seven days beyond (dependent on the phase-specific disease progress), the weight of the mice, the consistency of their stool and a possible blood occurrence were registered to determine the disease activity index (DAI). The DAI is calculated by adding the scores of each of the three categories weight loss, stool consistency and hemoccult test (see Table 5-4). Days 10 to 12, (DSS 1), 29 to 33 (DSS 2) and 48 to 53 (DSS 3) were determined as the important periods of time to check bodyweight and DAI. These periods include three days of normal drinking water after DSS treatment and consider the earlier response to DSS from phase to phase.

Table 5-4: Calculation of the DAI after Kim *et al.* (2012).

DAI category	Evaluation	Score
Weight loss	No loss 1 – 5% 5 – 10% 10 – 20% >20%	0 1 2 3 4
Stool consistency	Normal Loose Diarrhea	0 2 4
Hemoccult test / bleeding	No blood Hemoccult positive Visual pellet bleeding Gross bleeding / blood around anus	0 1 2 4

In the experiments with hydroxylase inhibitor administration, DMOG was applied three times per DSS cycle (on day 1, 3 and 5): 320 mg/kg DMOG were solved in sterile PBS (maximum volume [µL] = body weight [g] * 10) and injected i.p. The whole procedure is summarized schematically in Figure 5-1.

To ensure the reproducibility of the results, three rounds of the AOM-DSS and the AOM-DSS-DMOG model each were carried out with five to seven DSS-treated animals and up to three control animals per experiment and genotype.

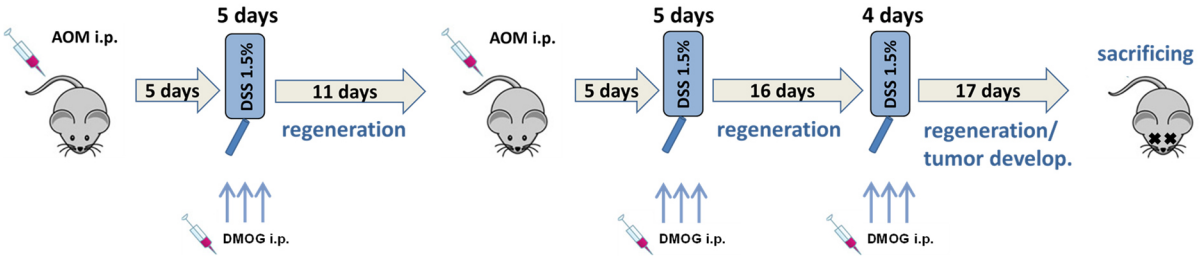

Figure 5-1: Schema of the AOM-DSS(-DMOG) mouse model for colitis-associated CRC. Mice were injected twice with AOM (10 mg/kg bodyweight, i.p.) and treated with 1.5% DSS for two phase of five days and a third phase of four days. DSS cycles were interrupted by regeneration phases of 16 days. After 68 days altogether, mice were sacrificed by cervical dislocation. In the AOM-DSS-DMOG model, mice were injected with 320 mg of DMOG per kg bodyweight three times during DSS phases (day 1, 3 and 5).

To test DMOG for functionality, HBLAK bladder cells, which were used in the lab by default, were incubated with 1 mM DMOG for 4 hrs. Afterwards, proteins were isolated by adding 65 µL of lysis buffer containing 10% protease inhibitor (PI) after washing cells with PBS. Cells were loosened with a cell scraper and transferred to a 1.5 mL tube. After 20 min of incubation on ice, the samples were centrifuged at 10,000 rpm and 4° C for 5 min. The

supernatant was used for Western Blot analysis (see 5.12). The HIF signal of the treated cells was then compared to that of lysates of untreated HBLAK cells.

Three weeks after the last DSS phase had started, the preparation of the mice was carried out. 60 mg/kg pimonidazole from the Hypoxyprobe-1™ (MAb) Kit in 0.9% NaCl (total volume 100 µL) was injected i.p. Pimonidazole, belonging to the group of 2-nitroimidazole, is chemically reduced under hypoxic conditions. The reduced molecule can then bind to thiol groups of amino acids and hence accumulates in hypoxic tissue. Later, these areas with accumulated reduced pimonidazole can be visualized in an immunohistochemical staining. After one hour of incubation, mice were sacrificed by cervical dislocation.
The spleen was taken, weighed, pressed with PBS through a 70 µm cell strainer into a 50 mL tube (total volume about 20 mL), and stored on wet ice for further analysis (see 5.6).
The colon was cut off at the caecum and anus, cleared from adhesive fat and rinsed with PBS to remove fecal remains. The length and weight of the colon was documented before it was opened longitudinally and photos were taken. Afterwards, 1 cm of the distal end was cut off and plunged in 4% PFA overnight at 4 °C for immunohistochemical studies. If a tumor with a diameter of more than 2 mm was found in the middle or proximal part of the colon, it was excised and put in 4% PFA for immunohistochemical studies. The next 1.5 cm of the distal colon were collected in two 2 mL tubes for RNA- (0.5 cm) and protein- (1.0 cm) extraction, quick-frozen in liquid nitrogen and stored at -80 °C until further processing. Another day, the frozen RNA samples were homogenized in 700 µL of 4M GTC solution and stored at -20 °C until starting the RNA isolation (see 5.8). Protein samples were homogenized in 300 µL of the colon lysis buffer. Afterwards, the samples were centrifuged for 5 min at 13200 rpm and 4 °C and the supernatant was collected in a fresh 1.5 mL tube and stored at -80 °C.

5.6 Flow cytometry

Singularized spleen cells were diluted in PBS and used for flow cytometry analysis to determine the status and composition of the splenic immune cells.
Spleen cells were counted and seeded in a 96-well round bottom plate with 4 x 10^6 cells / well in a total volume of 20 µL. Antibodies were premixed in fluorescence activated cell sorting (FACS) buffer with different dilution factors and in combination (see Table 5-5). 50 µL of the antibody mix were added to the cells and the plate was incubated for 20 min at 4° C in the dark. All following incubation and centrifugation steps were carried out at 4° C and in the dark. To wash the cells, 200 µL of FACS buffer were added and the plate was centrifuged for 5 min at 1500 rpm. The supernatant was discarded. Cells were resuspended in 200 µL of

FACS buffer and ready for measurement with the FACSCanto™ II flow cytometer. Measurement and analysis of the results were performed with the FACSDiva™ software.
A fixable viability dye (FVD) was used to mark dead cells. It was added to the antibody mix with a dilution factor of 1:200. In the analysis, only FVD negative cells were considered. Staining of samples in each fluorophore channel was compared to that of an unstained control: The gate for intensities determined as positive was set to get less than 1% of positive cells in the unstained control. This allowed subtracting false positive staining for the single fluorophores. To investigate if certain cells are co-expressing two or more markers, the gate of one fluorophore could be copied into another resulting in the percentage of double-positive cells.
Each day of measurement, the compensation of the flow cytometer had to be calculated. Therefore, each fluorophore (conjugated to an antibody binding a marker that was most likely expressed in a sufficient amount on the cells) was measured individually. The results were compared with an unstained control and the compensation was calculated by the FACSDiva™ software.

Table 5-5: FACS antibodies/dies with conjugated fluorophore and dilution factor.

Antibody	Fluorophore	Dilution
CD11b	Pacific Blue	1:200
CD11c	PE-Cy7	1:200
CD86	APC	1:200
FVD	APC-Cy7	1:200

5.7 Isolation of epithelial cells from the colon

A whole murine colon, dissected as fat-free as possible, was needed for the isolation of epithelial colonic cells. The colon was washed with sterile PBS to remove fecal remains and placed in a 6-well plate, embedded in PBS. The colon was then cut into small pieces and washed again with ice-cold PBS. 3 mL of chelating buffer containing EDTA were added. After an incubation of 30 min on ice, the mixture was pipetted up and down strongly several times and was then transferred into a 50 mL tube. After 3 min in which the colon pieces could settle, the supernatant was removed. 3 mL of chelating buffer without EDTA were added and mixed with the colon pieces by pipetting up and down with a 10 mL pipette to detach the epithelial cells. After the settling of the solid components, the supernatant containing the loosened epithelial cells was removed and collected in another tube. 2 mL of the chelating

buffer were added, mixed with the solid colon pieces by pipetting and the supernatant was added to the previously collected supernatant. This procedure was repeated 3 to 4 times. The supernatant collection was then centrifuged at 1800 rcf for 3 min. After removing the supernatant of the centrifugation, the pellet was washed in 2 mL of PBS and centrifuged again at 900 rcf for 3 min. The supernatant was discarded, and the pellet was resuspended in 10 mL of PBS.

To prepare the samples for RNA isolation, 1 mL of cell suspension was transferred into a 2 mL tube and centrifuged at 13,200 rpm for 1 min. The supernatant was discarded and 700 µL of GTC solution were added to the pellet. After vortexing this mixture, it could be stored at -20 °C until the RNA isolation was started (see 5.8).

5.8 RNA isolation and cDNA synthesis

Samples for RNA isolation were stored at -20 °C in 700 µL of 4M GTC solution. After thawing, 70 µL of 2M NaOAc were used to acidify the solution. Besides, 500 µL of phenol and 350 µL of phenol:chloroform:isoamyl alcohol mixture were added. While vortexing, the suspension turned milky white and became cloudy. If not, another 100 µL of the phenol:chloroform:isoamyl alcohol mixture could be added to achieve this state. The samples were incubated on ice for 60 min and centrifuged at 13,200 rpm and 4 °C for 30 min subsequently. In 1.5 mL tubes, 600 µL of isopropanol were provided so that the aqueous phase with the RNA could be transferred into these tubes. After mixing, the samples were frozen at -20 °C overnight.

The next day, samples were put into the centrifuge at 13,200 rpm and 4 °C for 30 min. Supernatant was discarded, and the pellet was air-dried for one hour to get rid of phenol remains. 300 µL of GTC solution and 500 µL of isopropanol were added before mixing the solution and freezing it at -20 °C overnight to precipitate the RNA.

For the colon samples from experimental animals, potential DSS residues had to be removed carefully as they would interfere with cDNA synthesis. Therefore, a few steps containing sample treatment with LiCl were added to the protocol. First, samples were centrifuged for 30 min at 13,200 rpm and 4 °C. Supernatant was discarded, and pellets were resuspended in 180 µL of DEPC water. 20 mL of an 8 M LiCl solution were added and the mixture was incubated on ice for 2 hours. Centrifugation and addition of DEPC water and LiCl solution followed by the incubation were repeated. After another centrifugation at 13,200 rpm and 4 °C for 30 min and removal of the supernatant, pellets were resuspended in 200 µL of DEPC water. 20 µL of 3 M NaOAc and 440 µL 100% ethanol were added and the mixture was stored at -20 °C overnight.

Samples were centrifuged at 13,200 rpm and 4 °C for 30 min. Supernatant was discarded, and pellets were air-dried for a few minutes. 500 µL of 75% ethanol (in DEPC water) were added. After mixing, the suspension was incubated for 15 min at room temperature (RT). Supernatant was removed, and pellets were air-dried properly. The RNA pellet was resuspended in 20 µL (epithelial cells) or 60 µL (colon tissue) of DEPC water by heating the solution to 60 °C for maximum 10 min.

RNA concentration and purity could be measured with the Epoch™ Microplate Spectrophotometer and a Take3 plate. For short storage, RNA was frozen at -20 °C, for longer storage at -80 °C.

For cDNA synthesis, deionized water was added to 1 µg of RNA to gain 9.5 µL in total. Diluted RNA was mixed with 2.5 µL of oligo-dT primers and heated to 68 °C for 10 min. After another 10 min on ice, 13 µL of the reaction mix were added (see Table 5-6) and the cDNA synthesis was started (see Table 5-7). For each cDNA synthesis procedure, a negative control with deionized water instead of an RNA sample was added to verify the purity of the components. Newly synthesized cDNA was checked by a standard polymerase chain reaction for the house-keeping gene β-actin (see 5.9).

Table 5-6: Reaction mix for cDNA synthesis.

Reaction mix component	Volume per sample (µL)
5X M-MLV RT buffer	5
dNTPs	5
H_2O	2.5
Reverse transcriptase	0.5

Table 5-7: Protocol of cDNA synthesis in the mastercycler.

Temperature	Time (min)
45 °C	90
52 °C	30
95 °C	15

5.9 Polymerase chain reaction (PCR)

The expression of genes in a certain tissue or cell line can be detected by the polymerase chain reaction (PCR). Here, a part of the gene of interest is amplified by a DNA polymerase after the binding of specific primers and the product can then be visualized on an agarose gel

containing ethidium bromide. The cDNA made from the RNA of the experimental mice or isolated epithelial cells was analyzed by PCRs, as the presence of certain genes in the cDNA leads to their mRNA expression level.

For a PCR reaction, 0.5 µL of cDNA template were mixed with 24.5 µL of a reaction mix containing the polymerase, its reaction buffer, dNTPs and the gene specific primers (see Table 5-8). For each PCR mix a negative control without a DNA template was run to verify the purity of the deionized water and the primers.

Table 5-8: Reaction mix for a PCR per sample.

Component	Volume per sample (µL)
5X GoTaq reaction buffer	5
dNTPs	2
Primer 5' / 3' (200 µM)	0.5
GoTaq G2 polymerase	0.1
H_2O	17

The primer sequences used for PCRs and quantitative PCRs are listed in Table 5-9.

Table 5-9: Primer sequences for qualitative and quantitative PCRs.

Gene	Sequence	Product length (bp)
5' β-actin (*Actb*) 3' β-actin (*Actb*)	ATATCGCTGCGCTGGTCG TTCCCACCATCACACCCTGG	129
5' *F4/80* 3' *F4/80*	TCTGGGGAGCTTACGATGGA GAATCCCGCAATGATGGCAC	237
5' *Fih* 3' *Fih*	AGAGTAGAGATGGCGGCGAC CTGGCTCAGACGTGGGATG	150
5' *Phd3* 3' *Phd3*	GGCCGCTGTATCACCTGTAT GGCTGGACTTCATGTGGATT	134
5' *Vegf* 3' *Vegf*	ACTGGACCCTGGCTTTACTG ACTTGATCACTTCATGGGACTTCT	99

After mixing the cDNA templates with the reaction mix, the PCR program was started in the mastercycler. The program (see Table 5-10) consists of an initial denaturation of the DNA followed by 35 cycles of a denaturation, an annealing and an elongation phase. A terminal phase to complete the synthesis finishes the reaction. The annealing temperature is dependent on the chosen primers, but all reactions in this work could be performed at 60 °C.

Table 5-10: The standard PCR program for the GoTaq G2 polymerase.

Phase	Temperature	Duration
Initial phase	96 °C	3 min
Denaturation	96 °C	1 min
Annealing	60 °C	1 min
Elongation	72 °C	1 min
Terminal synthesis	72 °C	10 min

The synthesized PCR product was visualized on a 2% agarose gel containing 0.08% ethidium bromide. The first gel slot was filled with 10 µL of a 100 bp DNA ladder to enable the analysis of the PCR product. Sample gel slots were filled with 20 µL of the PCR product. After 45 min of electrophoresis at 100 V, the gel was photographed under ultraviolet (UV) light.
Qualitative PCRs were used to test the specificity of primers or to verify the success of a cDNA synthesis reaction with primers for β-actin.

5.10 Quantitative PCR (qPCR)

To quantify the expression of a gene of interest in an mRNA sample, a quantitative PCR (qPCR) can be conducted with the corresponding cDNA and gene specific primers. 0.5 µL of cDNA were used as a template and mixed with the reaction components (see Table 5-11). For primer sequences see Table 5-9. 10 µL of this reaction mixture were then pipetted into a well of a 96-well plate. For a duplicate determination, another 10 µL were placed into the next well. The first two wells were reserved for the reaction mixture without DNA template as a negative control.

Table 5-11: Reaction mixture for a qPCR approach.

Component	Volume per sample (µL)
Biozym Blue S'Green qPCR Kit	12.5
Primer 5' / 3' (200 µM)	0.5
H_2O	11

The 96-well plate was placed into the iCycler iQ5™ and the PCR program was started (see Table 5-12). All qPCRs were carried out at an annealing temperature of 60 °C and with

40 cycles of denaturation/annealing/elongation. To check the purity of the primers, a melting curve of the PCR product was measured for each primer pair from time to time to exclude the existence of side products.

Table 5-12: The qPCR program for the Biozym Blue S'Green qPCR Kit.

Phase	Temperature	Duration
Initial phase	95 °C	10 min
Denaturation	95 °C	15 s
Annealing and elongation	60 °C	90 s

The iCycler iQ5™ detects the amount of PCR product by the fluorescence of the SYBR Green dye and quotes the Cycle of Threshold (C_T) with an automatically calculated threshold. This C_T value is normalized to the house-keeping gene ß-actin by the $\Delta\Delta C_T$ method (Livak *et al.*, 2001) to gain fold change values in comparison to untreated wildtype samples.

5.11 RNAseq

Isolated RNA (see 5.8) was treated with DNase before RNAseq analysis. 10,000 ng in 50 µL of DEPC water were mixed with 5 µL of a solution consisting of the reaction buffer for DNase digestion and 10% rDNase (as described in the manual of the RNA isolation kit from Machery-Nagel). The reaction mix was centrifuged shortly at 1000 rcf and incubated for 10 min at 37° C. 5.5 µL of 3M NaOAc (pH 5.2) and 150 µL of 100% ethanol were added and the whole mixture was deep-frozen for several hours to precipitate the RNA again. Subsequently, the mix was centrifuged for 10 min at 13,200 rpm and 4° C. The supernatant was discarded, and the pellet was washed with 500 µL of 75% ethanol (diluted in DEPC water). RNA isolation was then carried out as described in 5.8.

1000 ng of DNase-treated RNA were sent to StarSEQ GmbH (Mainz, Germany) for Illumina™ NextSeq 500 analysis. After a quality check with a Bioanalyzer, samples were successfully sequenced. Therefore, mRNA was captured by its poly(A) tail, fragmented and primed. From these fragments, corresponding cDNA was synthesized, completed with a second strand and finally sequenced. The sequenced fragments were then matched to the accordant gene from a gene library of the species. The mean number of fragments per gene could then be compared between the experimental groups.

Raw data were analyzed by Dr. Anne Bicker (Institute of Organismic and Molecular Evolution, Johannes Gutenberg-University, Mainz, Germany) resulting in a list with fold change- and p-values for every gene of $FIH^{fl/fl}$xVillinCre mice in comparison to $FIH^{fl/fl}$ mice. Whole colon RNA of control mice (n = 4) as well as DSS-AOM- (n = 3) and DSS-AOM-DMOG- (n = 4) treated mice were sent for sequencing. The expression data were used for Gene Ontology (GO) terms analysis and Ingenuity Pathway Analysis (IPA), carried out by Dr. Anne Bicker.

5.12 Lowry protein assay, SDS-PAGE, and Western Blot

The Lowry protein assay was used to determine the concentration of a protein solution (Lowry *et al.*, 1951). 5 µL of the samples as well as 5 µL of a bovine serum albumin (BSA) standard ranging from 0.1 to 25 mg/mL were diluted with 45 µL of deionized water. After mixing, 20 µL were put into a well of a 96-well plate. For a duplicate determination, another 20 µL were placed into the next well. 10 µL of reagent A and 75 µL of reagent B were added to each well. After 5 min of incubation, the plate was read with the Epoch™ Microplate Spectrophotometer at a wavelength of 700 nm and the protein concentrations of the samples were calculated based on the BSA standards.

For Western Blot analysis, 30 - 60 µg protein of whole cell lysate per sample were mixed 1:4 with 4X sodium dodecyl sulfate (SDS) buffer and heated up to 95° C for 5 min for denaturation. Proteins were then separated by mass using the SDS polyacrylamide gel electrophoresis (SDS-PAGE) after Laemmli (1970). The discontinuous gel consists of two parts: a broad separating gel with 7.5% acrylamide and a stacking gel on top with 5% acrylamide (see Table 5-13). A sample comb with 10 or 15 pockets was placed into the stacking gel to establish the formation of gel slots that can be loaded with samples. The denatured protein samples as well as a standard protein ladder were put on the gel and electrophoresis was executed at 120 V for about 90 min in a chamber filled with running buffer.

Table 5-13: Composition of the stacking and the separating gel for SDS-PAGE.

Component	Stacking gel (5%)	Separating gel (7.5%)
Bisacrylamide (30%)	0.83 mL	2.5 mL
4X Upper buffer	1.25 mL	-
4X Lower buffer	-	2.5 mL
A. dest.	2.92 mL	5 mL
APS	50 µL	100 µL
TEMED	5 µL	10 µL

After electrophoresis, proteins were supposed to be transferred to a nitrocellulose membrane by Western Blot. Therefore, the method of Towbin *et al.* (1979) was used. The acrylamide gel containing the proteins was placed onto the membrane and an electrophoresis was carried out at 110 V for 90 min in a chamber filled with blotting buffer. The success of the protein transfer was visualized by staining the membrane with Ponceau S solution. Proteins on the membrane should appear red. Subsequently, Ponceau S solution was washed out by TBS-T (3 x 5 min). To prepare the membrane for antibody treatment, it must be blocked by a solution rich in protein like 5% skimmed milk. The membrane was slued in milk for 1 hr at RT. Primary antibody (anti-murine FIH-1/HIF-1AN, from rabbit, Novus; or anti-murine actin, from rabbit, Sigma-Aldrich; or anti-human HIF-1α, from mouse, BD Transduction; all 1:1000 in 5% skimmed milk) was incubated overnight at 4° C.

The next day, the membrane was washed 3 x with TBS-T for 5 min. Secondary antibody (anti-rabbit Ig or anti-mouse Cx40, HRP-linked, Cell Signaling / Alpha Diagnostics, respectively, 1:10,000 in 5% skimmed milk) was incubated for 1 hr at RT. After washing the membrane with TBS-T (5 x 3 min), an ECL detection system was used to get a chemiluminescent signal that could be detected by the Fusion-FX7 or by an X-ray film in an X-ray developer machine.

5.13 Immunohistochemistry

After an incubation of at least 24 hrs in 4% PFA at 4 °C (see 5.5) the tissue samples for histological analysis were dehydrated in an automatic tissue dehydration machine. The protocol of the dehydration process is shown in Table 5-14.

Table 5-14: Protocol of dehydration of tissue samples for histological analysis.

Solvent	Time
70% Ethanol	50 min
96% Ethanol	50 min
96% Ethanol	50 min
100% Ethanol	50 min
100% Ethanol	60 min
Xylene	40 min (3 x)
Paraffin	70 min
Paraffin	infinite

Dehydrated tissue samples were then embedded in paraffin to build a paraffin block which could be dissected in slices with a thickness of 4 µm at a microtome. These thin tissue pieces could then be mounted on microscope slides, on which they needed to dry overnight. For tissue staining, paraffin was removed by xylene and the sample was hydrated again. The process of paraffin removal and rehydration is slightly different for immunohistochemical staining (see Table 5-15) in comparison to a hematoxylin and eosin (H&E) staining (see Table 5-16).

Table 5-15: Paraffin removal and rehydration process for immunohistochemical stainings.

Solvent	Time
Xylene	3 x 5 min
100% Ethanol	2 x 3 min
96% Ethanol	3 min
90% Ethanol	3 min
80% Ethanol	3 min
70% Ethanol	3 min

Table 5-16: Paraffin removal and rehydration process for H&E stainings.

Solvent	Time
Xylene	2 x 10 min
Isopropanol	5 min
90% Ethanol	5 min
70% Ethanol	5 min
50% Ethanol	5 min

For **H&E staining**, the slides were put in a 50% hematoxylin solution for 30 s which turns into the blue hematein in acid environments like the cell nucleus or the endoplasmic reticulum. After flushing in tap water (which enables the staining reaction due to an increase of the pH), the slides were put shortly in deionized water and then in an eosin solution for 40 s which marks the cell plasma with a red staining. After washing in deionized water, slides were dehydrated again by a short incubation in 50%, 70% and 90% ethanol as well as isopropanol. After incubation in xylene (2 x 5 min), the tissue samples were covered by a cover slip using Entellan® as mounting medium.

The immunohistochemical stainings for **FIH and F4/80** started with the antigen retrieval. Slides were boiled in retrieval solution for 15 min. After the samples had cooled down, the

slides were washed in PBS-T (2 x 2 min). To block endogenous peroxidase activity, samples were incubated in 3% H_2O_2 for 10 min and washed again in PBS-T (2 x 2 min). In addition, potential nonspecific binding sites needed to be blocked by a protein block with 5% goat serum (in PBS-T) for 1 hr at RT. Afterwards, slides were incubated with the primary antibody (see Table 5-17), diluted in 5% goat serum, or with 5% goat serum as negative control. The next day, samples were washed with PBS-T (3 x 2 min) and incubated with the biotinylated secondary antibody (anti-rat, Santa Cruz, or anti-rabbit, Dako, 1:200 in 5% goat serum) for 1 hr at RT. Afterwards, slides were washed with PBS (2 x 2 min) and incubated with the ABC kit for 30 min. The ABC kit needed to be prepared 30 min before usage: 2.5 mL of PBS were mixed with 1 drop each of solution A and B. Slides were washed again with PBS (3 x 5 min). 1 drop of 3,3'-Diaminobenzidine (DAB) solution (Vector) was mixed with 1 drop of the DAB buffer, 1 drop of H_2O_2 and 2.5 mL of deionized water. One slide was incubated with this DAB mix until a brownish staining became visible (1 – 10 min). Submerging the slide in deionized water stopped the reaction. All other slides were then DAB-treated in the same way (i.e. with the same duration) as the first one. For a counterstain, slides were put in a 25% hematoxylin solution for 30 s. Being flushed in tap water and washed in deionized water, the slides were dehydrated again. Therefore, the ethanol series from the rehydration process (see Table 5-15) was used in reverse: The slides were washed shortly in each ethanol solution and incubated 3 x 5 min in xylene before covering with Entellan® and a cover slip.

The protocol for the staining of the reduced pimonidazole (**Hypoxyprobe™-1** Kit) slightly differs from the description above. Here, it was important that slices were made not more than 24 hrs in advance. After the regular rehydration process (see Table 5-15), slides were boiled in an antigen retrieval solution for 20 min. Cooled down slides were then washed in TBS-T (2 x 2 min). Peroxidase block was done in 3% H_2O_2 for 20 min at RT. After washing in TBS-T twice for 2 min, a serum-free protein block was applied for 2 hr at RT. Again, slides were washed in TBS-T (2 x 2 min). A second protein block with 10% rabbit serum (host of the secondary antibody) was carried out for 20 min at RT. After removing the blocking solution, samples were incubated with the primary antibody (mouse-FITC-Mab1, Hpi in antibody diluent) overnight at 4° C. Negative controls incubated with pure antibody diluent. The next day, slides were washed in TBS-T (3 x 2 min) before incubation with the secondary antibody for 30 min at RT (rabbit-anti-FITC, HRP-linked, Hpi, 1:100 in antibody diluent). Again, slides were washed in TBS-T (3 x 2 min). The staining reaction with DAB as well as the counterstaining, the dehydration and the covering process were carried out in the same way as described above for FIH and F4/80 staining.

For **HIF-1α or HIF-2α staining**, the CSA II kit of Dako was used. Rehydration and antigen retrieval were carried out as for FIH and F4/80 staining. Slides were then washed in TBS-T twice for 2 min. Peroxidase block from the kit was added for 5 min at RT, followed by another

washing step with TBS-T (2 x 2 min). Washed slides were incubated with the protein block from the kit for 5 min at RT. After removal of the block solution, HIF-1α or HIF-2α primary antibody (see Table 5-17) diluted in antibody diluent was added, covering the whole slice. Slides were incubated overnight at 4° C. The next day, slides were washed in TBS-T three times for 5 min, as every washing step on this day. HRP-conjugated secondary antibody (anti-rabbit, Dako, 1:500 in antibody diluent) was added for 15 min at RT. After another washing step, amplification reagent of the kit was added for 15 min at RT in the dark. Slides were washed and incubated with anti-fluorescein-HRP from the kit for 15 min at RT. After washing them, slides were stained by the DAB solution (substrate buffer + DAB chromogen) from the kit. Staining reaction was stopped in deionized water, counterstained with 25% hematoxylin and dehydrated as described above.
All immunohistochemically stained slides were scanned with the Aperio ScanScope® CS2 with a magnification of 20x. Zoomed areas are shown in a magnification of 40x.

Table 5-17: Primary antibodies used in immunohistochemical stainings.

Antibody	Host	Dilution
Anti-mouse F4/80	rat	1:200
FIH	rabbit	1:700
Mouse-FITC-Mab1 (Hypoxyprobe™-1 Kit)	rabbit	1:100
HIF-1α	rabbit	1:10.000
HIF-2α	rabbit	1:10.000

5.14 *In situ* hybridization (RNAscope®)

For *in situ* hybridization, the RNAscope® 2.5 HD Detection Kit (BROWN) was used. HIF-1α and HIF-2α mRNA could be detected in 4 µm tissue samples on Superfrost™ slides. The *in situ* hybridization was carried out as described in the manufacturer's guide line for formalin-fixed paraffin-embedded samples.
The slides were put in in xylene twice for 5 min each and in 100% ethanol twice for 1 min. Afterwards, the samples hat to air-dry at least for 5 min. Hydrogen peroxide from the kit was added onto the dry slides for 10 min at RT. Then the slides were washed in deionized water twice by moving the slide rack up and down several times. Subsequently, the samples were put into boiling 1X Target Retrieval solution from the kit for 15 min. Slides were then washed in deionized water twice and in 100% ethanol. The air-dried tissue was then surrounded with a hydrophobic barrier by drawing a circle with an Immedge™ barrier pen.

The next day, Protease Plus from the kit was placed onto the dry tissue and the slides incubated at 40 °C for 30 min in the HybEZ™ Oven. Afterwards, samples were washed twice in deionized water. Then, the tissue samples were incubated with prewarmed (RT) Mm-HIF-1α (Cat No. 313821) or Mm-HIF-2α (Cat No. 314371) probes for hybridization. The incubation was carried out for 2 hrs at 40 °C in the HybEZ™ Oven as every incubation at 40 °C. Probes were removed by 1X Wash Buffer from the kit for 2 min at RT (regular washing step). The kit's Amp 1 solution was added for 30 min at 40 °C and removed by washing. Slides were then incubated in Amp 2 for 15 min at 40 °C and washed afterwards. The same steps were done for Amp 3 to 6 with 30 min (Amp 3 and 5) or 15 min (Amp 4 and 6) of incubation at 40 °C (Amp 3 and 4) or RT (Amp 5 and 6). The HIF-1α or -2α signal was detected using DAB from the kit (BROWN-A and BROWN-B mixed equally) for 10 min at RT. DAB was removed by washing the slides several times in deionized water. The tissue was counterstained in 25% hematoxylin for 20 s. After washing in deionized water, slides were put in 0.02% ammonia water for 10 s and washed again in deionized water. After incubation in 70%, 90%, 96% and 100% ethanol (2 min each) slides were put into xylene twice for 5 min. Like for immunohistochemically stained samples, the tissue was covered with Entellan®.

5.15 Cell culturing and transfection

FRET measurements were conducted in human bone osteosarcoma epithelial (U2OS) and human embryonic kidney (HEK293T) cells, co-immunoprecipitation in HEK293T. Both cell lines could be cultured in DMEM containing 10% FCS at 37 °C with 5% CO_2 and 21% O_2. For storing, cells were frozen in liquid nitrogen or at -80 °C (depending on the duration of storing) in medium that is laced with 5% DMSO. Cell culturing started with thawing and transferring into a T25 cell culture flask with 4 mL of medium. Cells were split three times a week in a 1:4 to 1:8 ratio in T75 flasks. First, cells were washed with prewarmed PBS and then incubated with 2 mL of trypsin solution to disassociate the cells from the bottom of the flask. Loosened cells were diluted in 5 mL of medium to stop the trypsin reaction. Cell suspension was centrifuged at 1200 rpm for 2 min in a 50 mL tube. The supernatant was discarded, and the pellet resuspended in 4 to 8 mL of medium. 1 to 2 mL of the cell suspension (depending on the splitting ratio) were then transferred into a new cell culture flask containing 8 mL of fresh and prewarmed medium. The number of passages was noted to avoid usage of cells with a higher number of passages than 30 for transfection as the transfection efficiency decreases with the number of splitting cycles.

For cell transfection, Lipofectamine™ 3000 (U2OS) and TurboFect™ (HEK293T) were used. The cells were seeded in an 8-well µ-slide for FRET microscopy or a 6-well plate for co-immunoprecipitation (Co-IP). For transfection, cells should become 80% confluent the next day. TurboFect™ transfection reagent was premixed with serum-free medium and plasmid DNA (see Table 5-18). After an incubation of 15 min at RT, the mixture was added to the cells. 5 to 6 hours later, the medium of transfected cells was renewed to prevent cell damage due to the transfection reagent. The transfection reaction with Lipofectamine™ 3000 included 2 transfection reagents but was apart from that like the TurboFect™ protocol. The Lipofectamine™ 3000 reagent was mixed with serum-free DMEM first before adding a mixture of DMEM, DNA and the P3000 reagent. The whole transfection mixture (see Table 5-19) was added to the cell medium after 10 min of incubation at RT. Again, the medium of the cells was renewed after 5 to 6 hours.

Table 5-18: Reaction mixture for the transfection of HEK293T cells with TurboFect™.

Component	Volume per well
Serum-free medium	50 µL
TurboFect™	1 µL / 500 ng DNA
Plasmids	100 – 2000 ng

Table 5-19: Reaction mixture for the transfection of U2OS cells with Lipofectamine™ 3000.

Component	Volume per well
Serum-free medium	12.5 µL + 12.5 µL
Lipofectamine™ 3000 reagent	0.75 µL
Plasmids	100 – 2000 ng
P3000 reagent	1 µL / 500 ng DNA

The plasmids used for FRET measurements and Co-IP are listed in Table 5-20. 100 - 200 ng of plasmids coding for a fluorescent protein alone, 100 - 400 ng of plasmids with a fluorophore-protein construct used as the donor of seFRET and 400 - 800 ng of plasmids with a construct used as the seFRET-acceptor were transfected. For FLIM measurements, 200 ng of the donor and 50 - 200 ng of the acceptor fluorophore fused to the proteins of interest were used, depending on the relative size of the acceptor plasmid to the donor, e.g. mCitrine-HIF-1α (~2500 bp). In a 6-well for Co-IP, 1000 ng of the bait and 2000 ng of the prey were transfected.

Table 5-20: List of plasmids used for FRET measurements and Co-IPs with species of origin, antibiotic resistance and source.

Plasmid	Origin	Resistance	Source
Cyan fluorescent protein (CFP)	Aequorea victoria	Ampicillin	ThermoFisher Scientific
CFP-HIF-2α	Aequorea victoria / H. sapiens	Ampicillin	Institute for Physiology, Essen
Yellow fluorescent protein (YFP)	Aequorea victoria	Ampicillin	ThermoFisher Scientific
YFP-ARNT	Aequorea victoria / H. sapiens	Ampicillin	Institute for Physiology, Essen
mTurquoise2-C1	Aequorea victoria	Kanamycin	Addgene_54842
mTurquoise2-HIF-1α	Aequorea victoria / H. sapiens	Kanamycin	see 5.16
mCitrine-C1	Aequorea victoria	Kanamycin	Addgene_54587
mCitrine-HIF-1α	Aequorea victoria / H. sapiens	Kanamycin	Institute for Physiology, Essen
mCitrine-ARNT	Aequorea victoria / H. sapiens	Kanamycin	Institute for Physiology, Essen
mCitrine-FIH	Aequorea victoria / H. sapiens	Kanamycin	see 5.16
mKO2-C1	Fungia concinna	Kanamycin	Addgene_54494
mKO2-ARNT	Fungia concinna / H. sapiens	Kanamycin	Institute for Physiology, Essen
mKO2-FIH	Fungia concinna / H. sapiens	Kanamycin	Institute for Physiology, Essen
mCherry-C1	Discosoma sp.	Kanamycin	Clonetech Cat. No. 632524
mCherry-ARNT	Discosoma sp. / H. sapiens	Kanamycin	Institute for Physiology, Essen
mCherry-FIH	Discosoma sp. / H. sapiens	Kanamycin	Institute for Physiology, Essen
mCherry-N1	Discosoma sp.	Kanamycin	Clonetech: Cat. No. 632523
FIH-mCherry	Discosoma sp. / H. sapiens	Kanamycin	Institute for Physiology, Essen

5.16 Cloning

Two plasmids from Table 5-20 had to be cloned during this work: mTurquoise2-HIF-1α and mCitrine-FIH. The HIF-1α and FIH gene were cut out from existing plasmids like mCitrine-HIF-1α and mCherry-FIH by the restriction enzymes SacI and BamHI as mTurquoise2, mCitrine, mKO2 and mCherry all had restriction sites for these enzymes. For this enzymatic digestion, 4 µg of mCitrine-HIF-1α (insert) and 2 µg of an empty fluorophore vector were mixed with 0.5 µL of each enzyme and 5 µL of CutSmart® reaction buffer (10X). Distilled water was added to reach 50 µL as total volume and the mixture was incubated at 37 °C

overnight. The insert was tested on an agarose gel (see 5.9) and purified with ZymoClean™ Gel DNA Recovery Kit. Vectors were treated with calf intestinal phosphatase to hydrolyze free phosphate groups to avoid any self-ligation and isolated with a DNA Clean & Concentrator Kit.

250 ng of isolated insert and 100 ng of isolated vector were mixed with 2 µL of T4 buffer (10X) and 1 µL of T4 ligase. Distilled water was added to reach 20 µL of total volume. The ligation reaction took place for 1 hr at RT. Ligation mixture was added to 100 µL of XL10 Gold bacteria. After an incubation of 30 min on ice, bacteria were heat shocked at 42° C for 45 s and put back on ice for 2 min. 900 mL of super optimal broth (SOB) medium was added and bacteria were grown at 37 °C for 1 hr. Bacteria solution was centrifuged for 1 min with 13,200 rpm and 90% of the supernatant was discarded. Bacteria pellet was resuspended in the remaining medium and transferred onto an agarose plate containing 50 µg/µL kanamycin. Agarose plates incubated overnight at 37 °C.

The next day, grown colonies were picked and dissolved in 2.5 mL of lysogeny broth (LB) medium with 50 µg/µL kanamycin. Again, bacteria were incubated overnight at 37 °C. From the bacteria solution, plasmids were isolated with the innuPREP Plasmid Mini Kit. Isolated plasmids were tested by digestion with the restriction enzymes SacI and BamHI and visualization on an agarose gel. XL10 Gold bacteria were again transformed with the correct plasmids and grown in 100 mL of LB medium with 50 µg/µL kanamycin to get a high amount of plasmid with the PureYield™ Plasmid Midi Kit.

5.17 Co-Immunoprecipitation (Co-IP)

HEK293T cells were transfected in a 6-well plate as described in 5.15. mCitrine-HIF-1α was used as the bait and FIH as well as ARNT constructs with mCherry represented the prey. Transfected cells were split the next day and incubated overnight at 37 °C and 5% CO_2 to gain two wells of the same condition to increase the amount of proteins. The next day, proteins were isolated. Therefore, medium of cells was aspirated, and cells were washed with cold PBS. 50 µL of lysis buffer were added to each well and cells were loosened with a cell scraper. Two wells with the same transfected cells were merged in a 1.5 mL tube and incubated for 20 min on ice. Afterwards, samples were centrifuged for 10 min at 13,200 rpm and 4 °C. Supernatant was then used as lysate sample: protein concentration was determined (see 5.12) and 40 µg of protein were filled up with washing buffer to a total volume of 30 µL (lysate sample) and deep-frozen at -20 °C.

500 µg of protein from the lysate probe were used for the Co-IP. First, GFP-traps had to be prepared by washing the total amount (5 µL per sample) with 250 µL of washing buffer. Traps were centrifuged at 2500 rpm and 4 °C for 2 min. The supernatant was discarded, and

the washing step was repeated twice. 500 µg of lysate protein were added to 5 µL of the traps, and the solution was filled up with washing buffer to a total volume of 400 µL. Samples incubated overnight at 4 °C tumbling overhead.

The next day, samples were centrifuged at 2500 rpm and 4 °C for 2 min. The remaining supernatant was discarded. 250 µL of washing buffer were added, samples were centrifuged at 2500 rpm and 4 °C for 2 min and the supernatant was discarded. The washing step was repeated twice with discarding the supernatant. The pellet from the last washing step was resuspended in 30 µL of washing buffer named the IP sample. All collected samples were mixed with 10 µL of 4X SDS buffer and heated up to 95° C for 10 min. Subsequently, samples were centrifuged at 5000 rpm and 4 °C for 2 min and supernatants were collected in a fresh 1.5 mL tube. For the analysis, an SDS-PAGE and Western Blot was carried out (see 5.12), using anti-RFP [6G6] from mouse, Chromotek, 1:1000 in 5% skimmed milk as the primary and anti-mouse Ig, HRP-linked, Alpha Diagnostic, 1:10,000 in 5% skimmed milk as the secondary antibody. To detect the bait, anti-GFP [3H9] from rat, Chromotek, 1:1000, was used as primary and anti-rat IgG, HRP-linked, Sigma, 1:10,000 in 5% skimmed milk as secondary antibody.

5.18 Sensitized-emission Fluorescence Resonance Energy Transfer (seFRET)

Protein-protein interaction can be studied in living cells by modern laser microscopy methods. Some of these use the fluorescence resonance energy transfer (FRET), first described by Theodor Förster (Förster, 1948). The energy transfer takes place between two fluorophores in close proximity through non-radiative dipole-dipole coupling. Excitation of the donor fluorophore raises an electron from the ground state S_0 to the excited state S_1. On its way back to the energy ground state, energy is emitted at a fluorophore specific relaxation wavelength. If this wavelength is situated in the excitation spectrum of another fluorophore (the acceptor) in close proximity (< 10 nm), this emitted energy is transferred to the acceptor and excites an electron from S_0 to S_1. The acceptor now emits energy at its specific wavelength. This physical principle of FRET is visualized in the Jablonski diagram (see Figure 5-2 A). It is a precondition for a functional donor acceptor pair that the emission spectrum of the donor and the excitation spectrum of the acceptor overlap. Often-used FRET donor acceptor pairs are CFP/YFP (see Figure 5-2 B) or modern derivatives like mTurquoise and mCitrine. Important properties that help to choose the right fluorescent proteins are brightness, photostability and no oligomerization (Shaner *et al.*, 2005). To study protein-protein interaction, the proteins of interest can be fused to the fluorophore pair of choice. Then, a positive FRET signal can only be detected if the fusion-proteins are in close proximity, where a protein-protein interaction can be assumed (nanometer range).

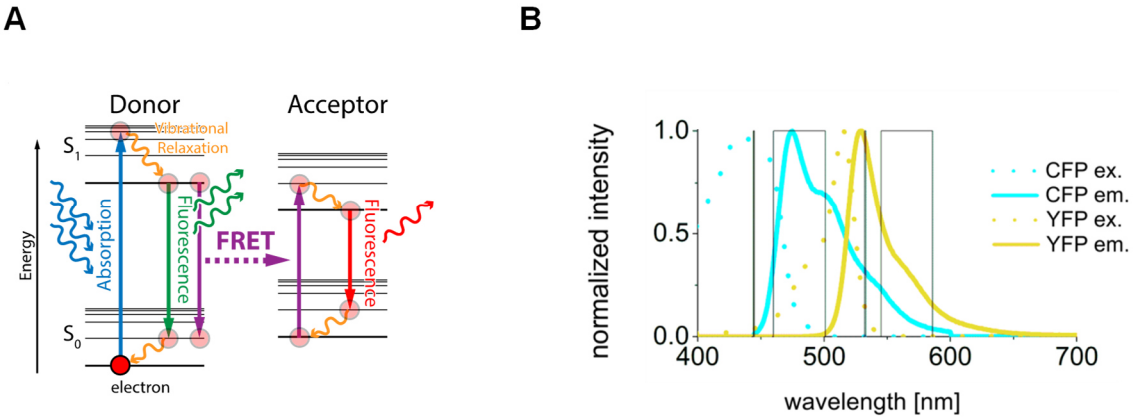

Figure 5-2: The FRET principle. A: The Jablonski diagram shows the principle of FRET (adapted from Hochreiter *et al.*, 2019). The excited donor fluorophore transmits energy to a corresponding adjacent acceptor fluorophore. The acceptor in turn emits an acceptor specific energy by fluorescence which can be measured in different setups. B: Fluorescence spectra of CFP (blue) and YFP (yellow), which are a suitable FRET pair (adapted from Prost-Fingerle *et al.*, 2017). The emission (em.) spectrum of CFP overlaps with the excitation (ex.) spectrum of YFP.

The FRET efficiency (E) depends on the actual distance r of the fluorophores and a fluorophore pair specific radius R_0 (so-called Förster radius) which implies the dipole-dipole orientation κ^2, the medium refractive index n, the quantum yield of the donor alone Q_D, and the spectral overlap integral J(λ) (see Equation 1).

$$E = \frac{R_0^6}{R_0^6 + r^6} \qquad \text{with } R_0(\text{Å}) = 0.221\ [\kappa^2 n^{-4} Q_D J(\lambda)]^6 \qquad (1)$$

This calculation presents the correlation between FRET efficiency and fluorophore distance. Hence it is possible to determine the mean distance of two fluorophore-fused proteins by FRET measurements as it was done for HIF-1α and ARNT by Wotzlaw *et al.* (2007).

In a sensitized-emission setup, the emission of the acceptor was measured directly after donor excitation. At an Axiovert 200M, Zeiss, microscope, CFP or mTurquoise2 or mTFP (donor) transfected cells were excited by a laser beam at 444 nm under controlled conditions with 37° C. To calculate the donor bleed-through, a donor-only sample was excited and detected in the emission spectrum of the acceptor (545 – 585 nm). As a negative control, cells transfected with soluble YFP/mCitrine-C1 as the acceptor were measured. Afterwards, the cells transfected with donor-fused HIF-1α and acceptor-fused ARNT or FIH were analyzed. The software used for these FRET studies (Anufis) was designed by Dr. A. Bernadini and Dr. C. Wotzlaw (Wotzlaw *et al.*, 2010). Resulting images were further processed with a self-written ImageJ script that subtracted the background noise, set an

intensity threshold of 100 and calculated mean FRET efficiencies from manually determined regions of interest (ROIs), which corresponded to single cells. FRET efficiency of a double transfected cell was then assigned to its acceptor to donor ratio resulting in a saturation curve (= positive FRET signal). Random collision depending on an increasing acceptor concentration would result in a straight line, an indication for a FRET negative sample. Exemplary images from the measurement were shown in false color images.

5.19 Fluorescence lifetime imaging microscopy (FLIM)

The fluorescence lifetime of a fluorophore is named τ_D and is dependent on several transition rates (k_F: fluorescent transition, k_{IC}: interconversion, k_{IS}: intersystem crossing; see Equation 2). Transferred emission energy by FRET results in a shorter lifetime of the donor fluorescence (τ_{DA}) under presence of an acceptor fluorophore as it acts as one additional non-radiative process (k_{FRET}) in the sum of transition rates (see Equation 3).

$$\tau_D = \frac{1}{k_F + k_{IC} + k_{IS}} \qquad (2)$$

$$\tau_{DA} = \frac{1}{k_{FRET} + k_F + k_{IC} + k_{IS}} \qquad (3)$$

This effect can be used to prove protein-protein interaction via fluorescence lifetime imaging microscopy (FLIM), an quantitative alternative to seFRET measurements, also in hypoxia-related research (Prost-Fingerle *et al.*, 2017).

To investigate the interaction of HIF-1α and FIH in living cells via FLIM, HEK293T cells were transfected with HIF- and FIH-fluorophore constructs as described in 5.15. A donor-only sample was needed as well as a negative control consisting of the donor and the acceptor fluorophore. Additionally, a positive control, which was a fused donor-acceptor pair could be measured to get the maximal FRET efficiency possible in that setup. The measurements were carried out 24 h after transfection with a Leica SP8 microscope at the 'Imaging Center Essen' (IMCES). Fluorophore lifetimes were detected by time-correlated single-photon counting (TCSPC). An appropriate donor-acceptor pair in our setup is mCitrine/mCherry, as the donor can be excited without exciting the acceptor fluorophore mCherry, which in turn is excited by non-radiative energy transfer from excited mCitrine (see Figure 5-3). A protocol how to use FLIM for protein-protein interaction analysis in living cells was published within the development of this thesis in *Hypoxia: Methods and Protocols*, 2018 (Schutzhold *et al.*, 2018). All procedures should be carried out at 37 °C and 5% CO_2, since the fluorophore lifetimes are temperature and pH sensitive. If DMOG was used, it was applied 2 hours before

the measurement to ensure an equal distribution of the chemical in the whole well and to gain an accumulation of HIF-α due to the inhibition of the PHDs.

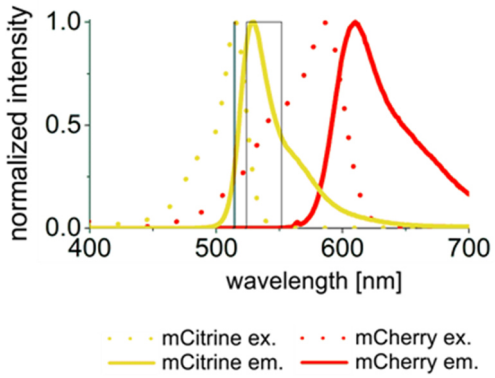

Figure 5-3: Fluorescence spectra of mCitrine and mCherry (adapted from Prost-Fingerle *et al.*, 2017). These fluorophores can be used in FLIM measurements. mCitrine serves as the donor fluorophore as its emission (em.) spectrum overlaps with the excitation (ex.) spectrum of mCherry which is used as the FRET acceptor.

After the measurement, there were three files from the SymPhoTime software that contained the information for the fluorophore lifetimes and the intensities as a function of time: *I (t)*. The lifetime of the donor only sample τ_D, derived from the TCSPC data via a mono-exponential fit (see Figure 5-4 A), and the lifetime of the donor-acceptor sample τ_{DA} could be used to calculate the FRET fraction α (see Figure 5-4 B and Equation 4), which represents the actual fraction of interacting molecules.

$$I(t) = I_0\, e^{\frac{t}{\tau_{AVG}}} = (1 - \alpha)\, e^{\frac{t}{\tau_D}} + \alpha\, e^{\frac{t}{\tau_{DA}}} \qquad (4)$$

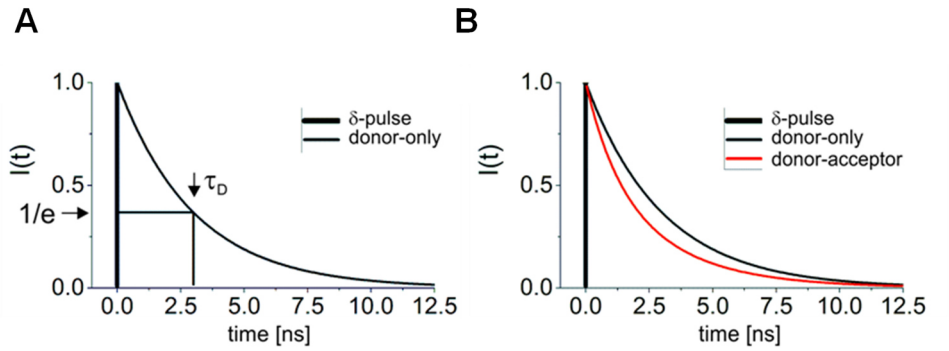

Figure 5-4: TCSPC data (adapted from Prost-Fingerle *et al.*, 2017). A: Theoretical TCSPC data from a donor-only probe after a δ-pulse. A mono-exponential fit is needed to calculate τ_D. B: Exemplary TCSPC data for a donor-only sample with a lifetime of 3 ns and a donor-acceptor lifetime (τ_{DA}) of 1.2 ns, assuming an interacting fraction of 0.6.

To create an α-map that contains the α-values for each pixel and an intensity map showing the counts per pixel we used a python-based code for global analysis of FLIM data called jediFLIM, developed by H. E. Grecco, K. C. Schuermann, and P. J. Verveer at the MPI of Molecular Physiology, Dortmund, Dept. II. (Clayton *et al.*, 2004, Grecco *et al.*, 2009, Verveer *et al.*, 2000). An instrumental response function (IRF) was measured to correct the data for instrumental artefacts. Fluorescein (τ = 4 ns) or mCitrine (τ = 3 ns) were used as IRF reference standards.

A threshold of 40 was applied to mask the cells within the counts per pixel map and set the background to 'not a number' (NaN). Afterwards, ROIs containing cells or cell compartments were drawn to calculate mean α-values for each condition. The α-values of the donor-only sample, the negative control, the positive control and the sample with the proteins of interest were then compared. α-maps were shown as false color images ranging from 0 to 1.

5.20 Statistical analysis

Statistical analysis was carried out with the PRISM® software (GraphPad), version 6.07. Two data sets were compared with the student's t-test. A p value smaller than 0.05 was determined as statistically significant: $p < 0.05$ = *, $p < 0.01$ = **, $p < 0.001$ = ***, $p < 0.0001$ = ****.

6 Results

6.1 Efficiency of the FIH knockout in epithelial cells of the colon

First, it was tested if FIH$^{fl/fl}$xVillinCre mice showed an efficient knockout of FIH in the colon epithelium. An efficient knockout induced by the loxP/Cre system was fundamental for the usage of these mice in the AOM-DSS model to study the effect of FIH on colorectal cancer development and colitis progression.

Colonic epithelial cells were isolated and tested for the expression of exon 2 of *Fih* via PCR with specific primers. The samples from FIH$^{fl/fl}$ mice show a clear band indicating a high expression level of exon 2 of *Fih* while the samples from FIH$^{fl/fl}$xVillinCre mice show no PCR product at all (see Figure 6-1 A). Even the test of whole colon samples of FIH$^{fl/fl}$xVillinCre mice for *fih* expression on protein level by Western Blot and exon 2 of *Fih* on mRNA level by qPCR resulted in a knockout efficiency of 70% (see Figure 6-1 B and C), although the colon consists of many different cell types besides epithelial cells.

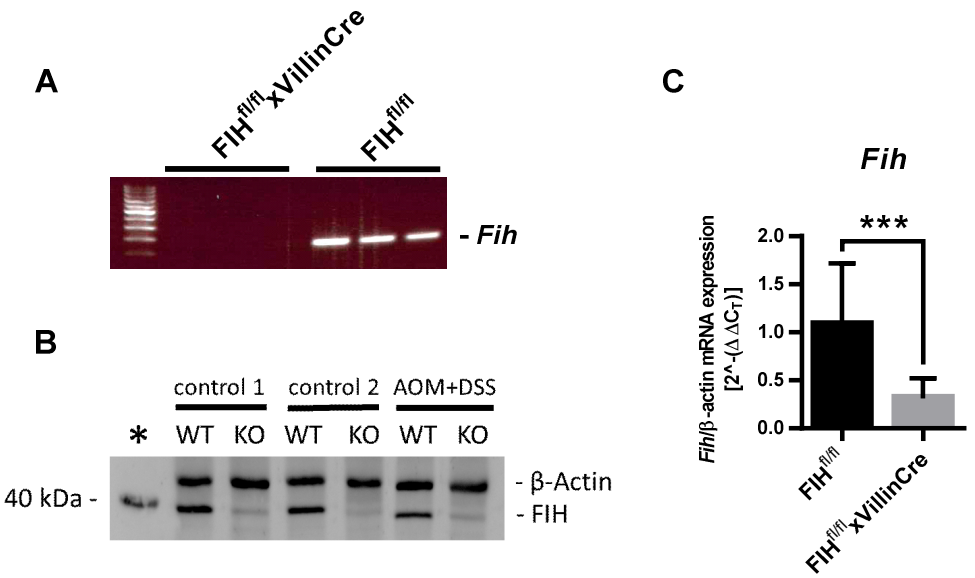

Figure 6-1: Knockout efficiency in the FIH$^{fl/fl}$xVillinCre mice proven by different methods. A: Photography of an agarose gel under UV light shows the results of a qualitative PCR of cDNA extracted from colon epithelial cells with exon 2-specific *Fih* primers (n = 3). B: Western Blot analysis of whole colon protein for FIH$^{fl/fl}$xVillinCre (KO) and FIH$^{fl/fl}$ (WT) mice. The FIH band was expected at 40 kDa in wildtype samples (FIH$^{fl/fl}$). β-actin serves as loading control of the immunoblot. * indicates the lane loaded with protein ladder (n = 3). C: *Fih* exon 2 mRNA expression from whole colon RNA was quantified by qPCR with normalization to the *β-actin* expression (mean ± SD, n = 20).

This decreased amount of FIH protein in the colon resulted in changes of HIF-1 target genes. In RNA samples from the whole colon of experimental control mice, *Phd3* expression is significantly increased in FIH$^{fl/fl}$xVillinCre mice (see Figure 6-2 A). Likewise, the expression of the HIF-1 target gene *Vegf* is substantially enhanced in FIH$^{fl/fl}$xVillinCre mice (see Figure 6-2 B, p = 0.06). A reduction of the HIF inhibitor FIH in the colon epithelium apparently leads to a stronger HIF-1 activation in the colon under normal conditions regarding C-TAD dependent target genes as *Phd3* and *Vegf*. Since FIH knockout mice show increased mRNA expression of HIF-1 target genes in the colon, these mice could be used for the investigation of the role of the FIH knockout on colorectal cancer development and colitis progression.

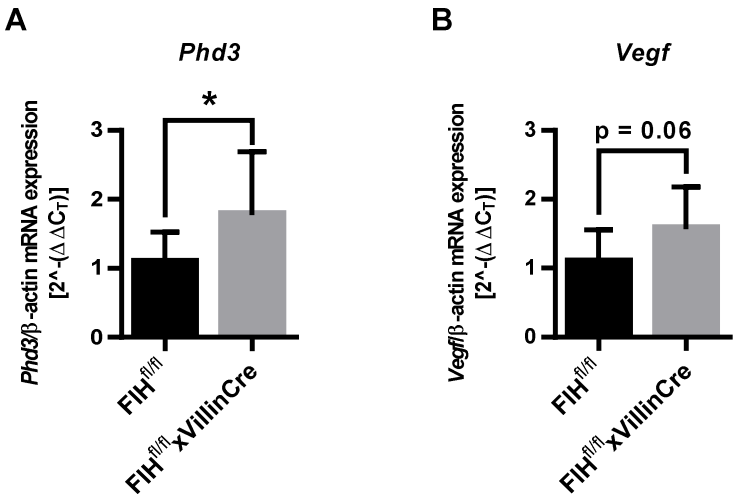

Figure 6-2: Expression of upregulated HIF-1 target genes in experimental control animals. The mRNA expression of C-TAD dependent HIF-1 target genes *Phd3* (A) and *Vegf* (B) in colon mRNA samples from FIH$^{fl/fl}$xVillinCre mice in comparison to wildtype animals, normalized to β-actin expression values (mean ± SD, n = 11).

RNA from the whole colon of exemplary DSS-AOM-treated mice as well as DSS-AOM-DMOG-treated and control mice was analyzed by RNAseq. The FIH knockout was clearly visible as a highly negative fold change in all animal groups (FIH$^{fl/fl}$xVillinCre mice compared to FIH$^{fl/fl}$ mice) (see Figure 6-3 A). Due to this strong reduction of *Fih* expression, the GO terms ‘cellular response to hypoxia’ and ‘cellular response to decreased oxygen levels’ appeared to be overrepresented in the set of downregulated genes in GO term analysis as *Fih* is one of them. The control mice also showed a higher mRNA expression of the HIF target genes *Phd3*, *Vegf*, and B-cell lymphoma 2 interacting protein 3 like (*Bnip3l*) (see Figure 6-3 B), all C-TAD dependent genes. In line with the qPCR data (see Figure 6-2), *Phd3* showed a higher fold change than *Vegf*.

The complete RNAseq data can be found on the enclosed data carrier. These data comprise lists of fold changes of all genes that occurred in the samples. FIH$^{fl/fl}$xVillinCre are always compared to FIH$^{fl/fl}$ mice in groups of untreated (control, n = 4), AOM-DSS-treated (n = 3) and AOM-DSS-DMOG-treated (n = 4) animals. Also added are lists of up- and downregulated GO terms with a p-value lower than 0.05 and of the IPAs with z-scores lower than -2 or above +2.

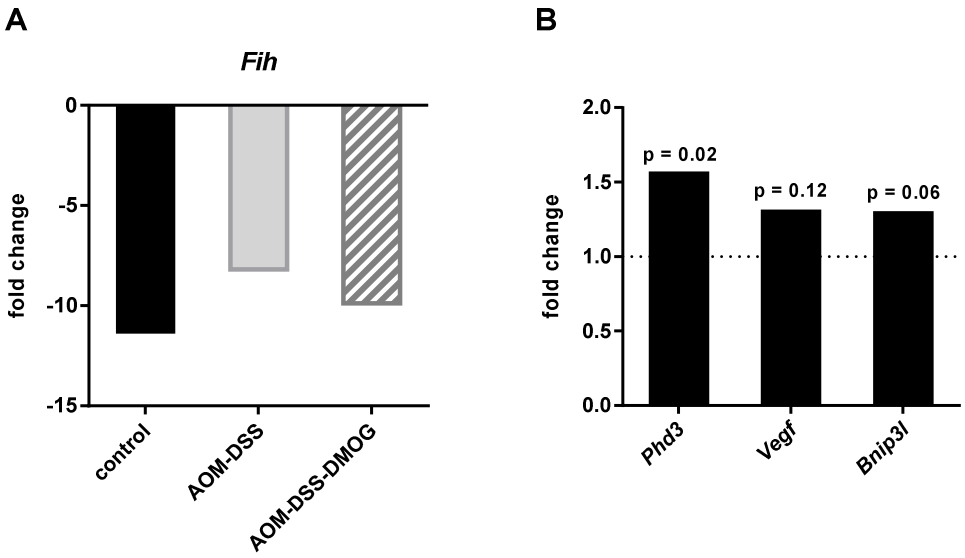

Figure 6-3: RNAseq data revealed a high FIH knockout efficiency. A: RNAseq results for the *Fih* gene. mRNA of *Fih* is strongly downregulated in FIH$^{fl/fl}$xVillinCre mice in comparison to FIH$^{fl/fl}$ littermates (mean, n = 4/3/4, p < 0.001 for all values). B: RNAseq results for the genes *Phd3*, *Vegf*, and *Bnip3l* for FIH$^{fl/fl}$xVillinCre mice compared to FIH$^{fl/fl}$ (means, n = 4).

6.2 Colitis progression and tumorigenesis in AOM-DSS-treated mice

To investigate the role of HIF activation and FIH knockout on tumor development after intestinal inflammation, FIH$^{fl/fl}$ and FIH$^{fl/fl}$xVillinCre mice were used in the AOM-DSS model. The mice were exposed to three periods of 1.5% DSS in the drinking water (4 to 5 days) and were injected with the carcinogen AOM twice (see Figure 5-1). During the DSS phases and a few days beyond that, the mice lost weight and showed disease symptoms like a softer stool and (occult and/or visible) blood in the feces and on the anus. These symptoms were summarized in a disease activity index (DAI), an indicator for the colitis progress.

FIH$^{fl/fl}$ and FIH$^{fl/fl}$xVillinCre mice lost weight due to the DSS treatment in comparison to control mice that got normal drinking water (see Figure 6-4 A), but there were no differences between FIH$^{fl/fl}$ and FIH$^{fl/fl}$xVillinCre mice. The bodyweight loss is an important factor for the

calculation of the DAI, but also symptoms like diarrhea and a bleeding anus are added to this score (see Table 5-4). The DAI increased during a DSS treatment with an increasing maximum per period. The DAI course indicated that the mice began to regenerate after a few days with normal drinking water, but with no significant score differences between $FIH^{fl/fl}$ and $FIH^{fl/fl}$xVillinCre mice at all (see Figure 6-4 B). The total DAI that the mice achieved during a DSS period suggested a tendency of a stronger DSS-induced colitis progress in $FIH^{fl/fl}$xVillinCre than in $FIH^{fl/fl}$ mice (see Figure 6-4 C) in the last DSS period.

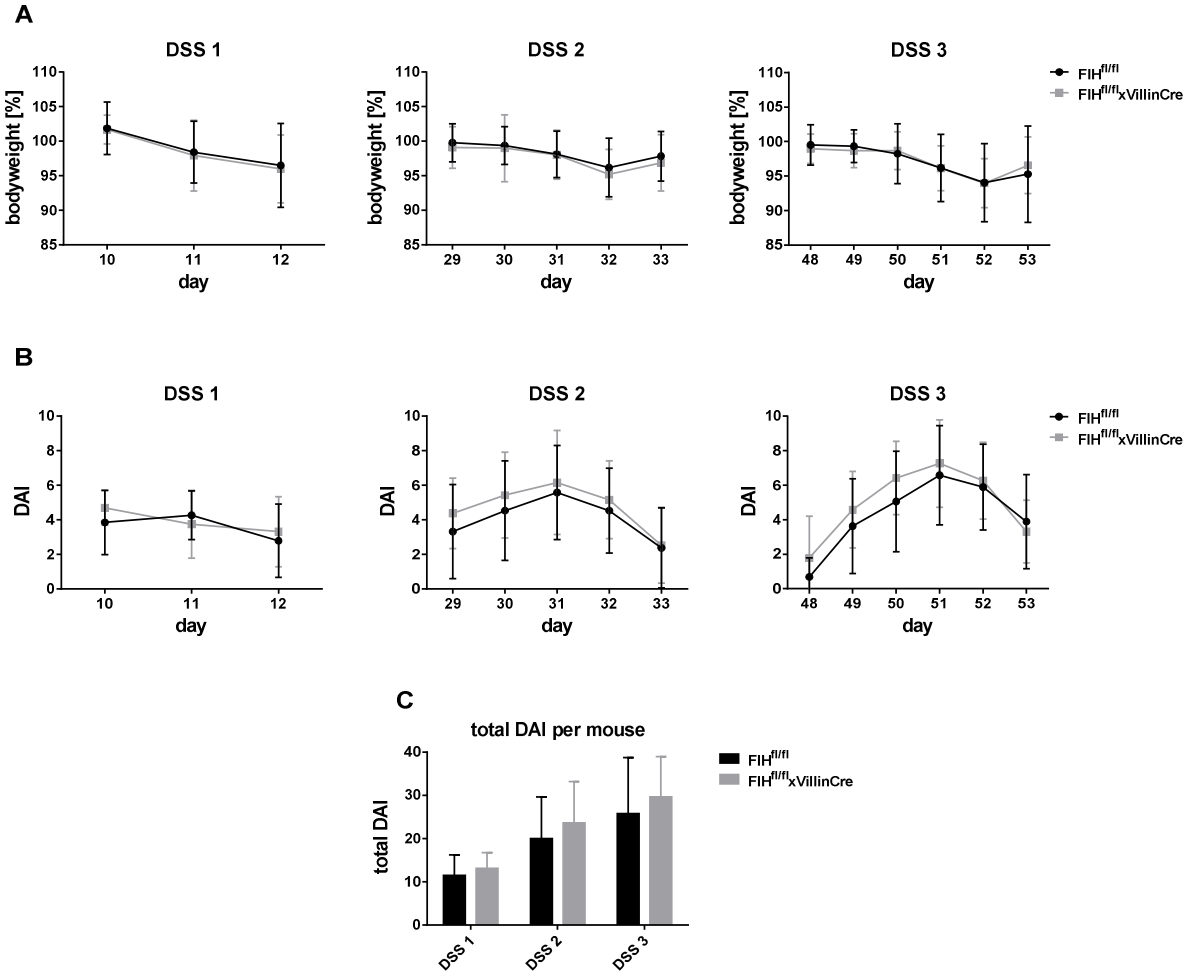

Figure 6-4: Disease progress showed no differences between wildtype and FIH knockout animals of the AOM-DSS model. A: Mice were weighed during the three DSS-treatments. Mean bodyweight percentage is shown for $FIH^{fl/fl}$ (black) and $FIH^{fl/fl}$xVillinCre (grey) mice. B: As a second index for the disease progress, the DAI was calculated in the DSS phases. The maximum possible DAI was 12. Mean DAIs of $FIH^{fl/fl}$ (black) and $FIH^{fl/fl}$xVillinCre (grey) animals are shown. C: The total DAI is the sum of all single DAIs from all days of one DSS phase of one mouse in the experiment. $FIH^{fl/fl}$ (black) and $FIH^{fl/fl}$xVillinCre (grey) mice are compared in each DSS phase (mean ± SD, n = 19).

After these three periods of DSS-induced intestinal inflammation, the experimental mice developed colorectal cancer. 17 days after the last DSS treatment had stopped, mice were sacrificed and analyzed for tumor development. About 20 single tumors grew in the colons of DSS-treated animals whereas the control mice that got the AOM injections without DSS treatment developed only a few small tumors (see Figure 6-5 A and B). The amount and size of tumors of a DSS-treated mouse even increased the weight of the colon significantly at constant colon length (see Figure 6-5 C and D). As there was a regeneration and tumor development phase of 2 weeks after the third DSS period, the colons of the treated animals did not show the typical shortening as they do when suffering from an acute colitis (Okayasu *et al.*, 1990).

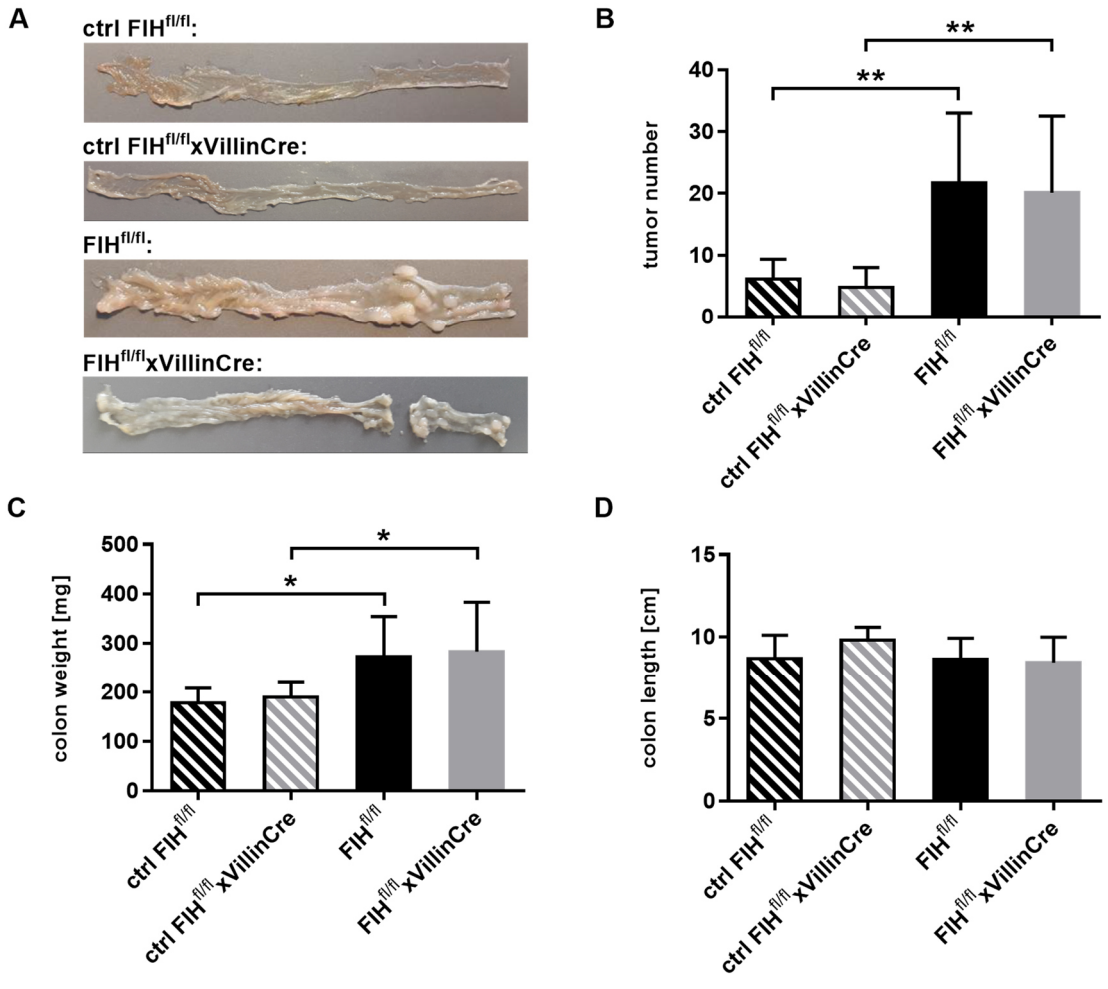

Figure 6-5: Tumor development in mice of the AOM-DSS mouse model. A: Photographic record of the opened colon after removing fecal remains from exemplary control and AOM-DSS-treated mice. B: Tumor numbers that were counted manually during preparation of control and DSS-treated, FlH$^{fl/fl}$ and FlH$^{fl/fl}$xVillinCre animals. C: Weight of the cleaned colons during preparation. Growth of big tumors resulted in an increased colon weight in DSS-treated animals. D: Lengths of the dissected and cleaned colons. B - D: Mean ± SD, n = 6 (controls), n = 19 (DSS-treated).

A closer look on the intestinal structure and the tumor microenvironment via H&E staining of about 1 cm of distal colon tissue from experimental mice did not reveal any differences between $FIH^{fl/fl}$xVillinCre and $FIH^{fl/fl}$ mice, either. Crypt structure was widely intact as the acute colitis had ended two weeks before preparation. For non-tumor sections of the intestine, a distinction between DSS-treated and control animals was not possible only by H&E staining (see Figure 6-6). The H&E stained tissue samples exhibited big protruding tumors as well as smaller integrated ones.

To illustrate the role of FIH in colonic tumors, the FIH protein was used as a target in an immunohistochemical staining. In $FIH^{fl/fl}$ mice and $FIH^{fl/fl}$xVillinCre mice, the epithelial FIH was hardly visible. In $FIH^{fl/fl}$ animals there was at least a faint brownish staining along the crypts which was missing in the $FIH^{fl/fl}$xVillinCre mice (see Figure 6-7). Tumor tissue showed a completely different picture: The complete tumors were positive for the FIH protein, in $FIH^{fl/fl}$ mice as well as in $FIH^{fl/fl}$xVillinCre mice (see Figure 6-7). Having a closer look at the localization of FIH it became clear that it translocated into the nucleus in several cells of the tumor, independently from the genotype.

As there was no significant effect of the FIH epithelial knockout on the disease progress during colitis periods or on the development of colorectal cancer in this model, another factor was added to the experimental setup. In a second approach, the hydroxylase inhibitor DMOG was applied three times during each DSS phase. This treatment was supposed to increase the amount of FIH substrate, which is HIF, as the prolyl hydroxylases were inhibited by DMOG. This might enhance the influence of FIH on the whole system and lead to more noticeable effects in the model.

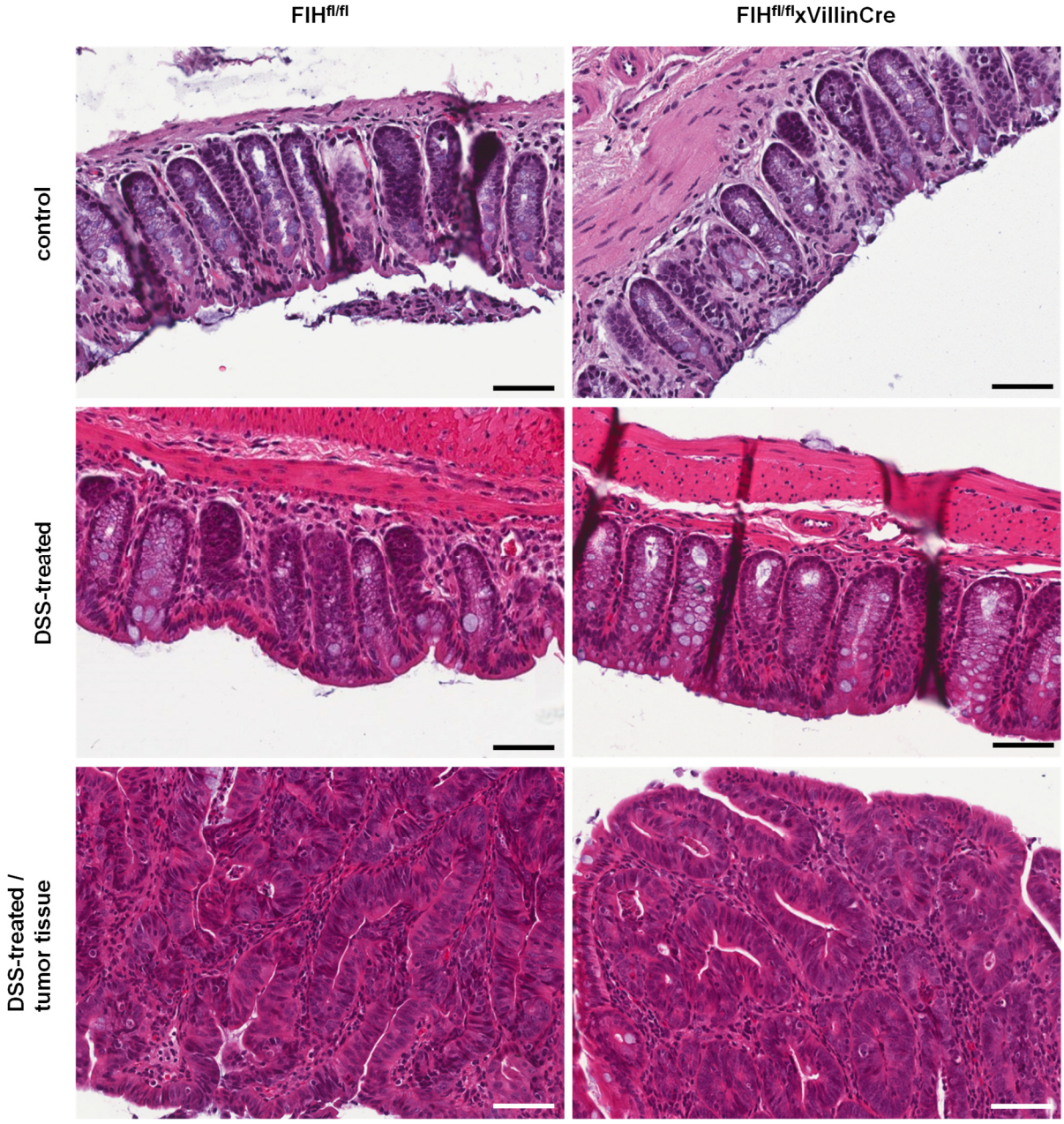

Figure 6-6: H&E staining of normal colon and tumor tissue. DSS-treated non-tumor colon tissue is comparable to tissue of control animals as there were two weeks of regeneration between the last colitis phase and preparation. Almost all slides of the distal colon part of DSS-treated mice showed regions of tumor tissue which is characterized by a chaotic and dense crypt structure. Non-tumor sections and tumor tissue from FIH$^{fl/fl}$ and FIH$^{fl/fl}$xVillinCre mice are not distinguishable. Scale bar = 50 µm.

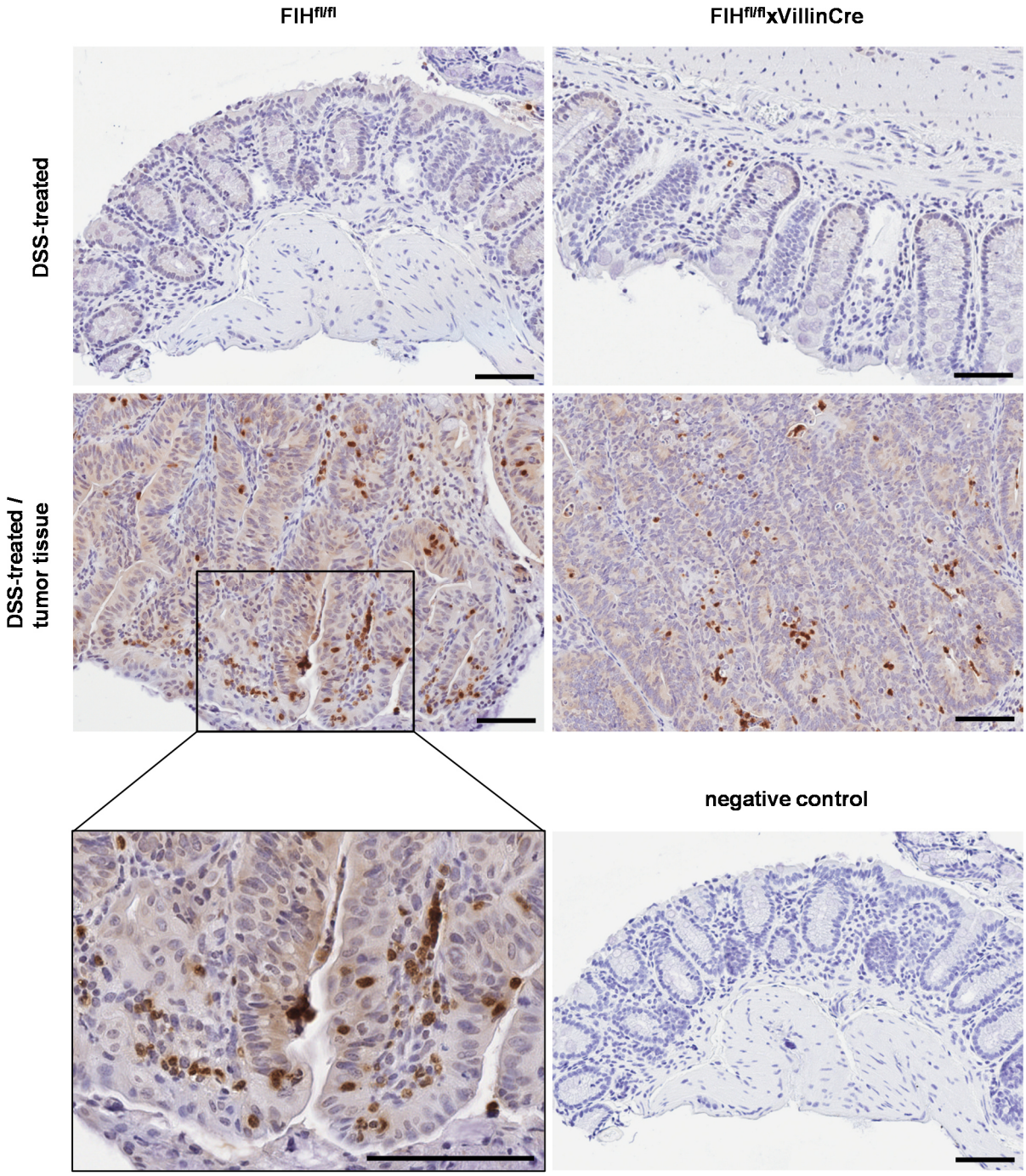

Figure 6-7: Immunohistochemical staining of FIH in AOM-DSS-treated mice. The colon tissue is shown with intact crypts from DSS-treated FIH$^{fl/fl}$ and FIH$^{fl/fl}$xVillinCre mice. In the middle row samples from tumor regions of DSS-treated animals are shown. One part of an FIH-positive tumor was magnified 4-fold for better visualization of FIH localization. The negative control reveals the specificity of the FIH antibody. Scale bar = 50 µm.

6.3 Colitis progression and tumorigenesis in AOM-DSS-DMOG-treated mice

DMOG was tested in cell culture (HBLAK) to ensure its functionality. In cell cultures, a DMOG treatment with a duration of minimum 1 hr and a concentration of at least 1 mM regularly leads to a remarkable stabilization of the HIF protein, which can be detected via Western Blot.

Here, the DMOG-treated cells showed a clear band for HIF-1α in the Western Blot analysis at about 120 kDa, which was expected. In untreated cells there is no HIF-1α signal detectable at all (see Figure 6-8). This result enables the usage of the DMOG in the mouse model.

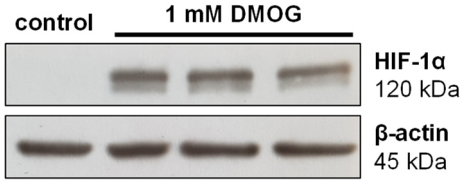

Figure 6-8: Positive functionality test of DMOG *in vitro*. To test DMOG functionality, a Western Blot analysis of control and DMOG-treated HBLAK cells was carried out. A HIF-1α band (~120 kDa) was clearly visible in the DMOG-treated cells, but not in the control lane. β-actin (~45 kDa) was used as a loading control and proved the existence of the protein lysate in all lanes.

The AOM-DSS-DMOG model was performed the same way as the AOM-DSS model with 3 phases of 1.5% DSS in the drinking water accompanied by DMOG administration and by recording weight loss, stool consistency and the hemoccult test results. These observations were summarized in the DAI. Both $FIH^{fl/fl}$ and $FIH^{fl/fl}$xVillinCre showed a DSS-induced weight loss and colitis disease progress (see Figure 6-9 A and B). The DAI of the $FIH^{fl/fl}$xVillinCre mice on day 5 of the last DSS phase was significantly decreased compared to the $FIH^{fl/fl}$ littermates. In addition to that, a tendency to a lower DAI in the $FIH^{fl/fl}$xVillinCre mice was observable on all the other days (see Figure 6-9 B). The total DAI, which is the sum of all DAIs of a mouse during one DSS phase, showed a lower value for the $FIH^{fl/fl}$xVillinCre mice as well (see Figure 6-9 C). In the third DSS phase, the disease progress is significantly reduced in $FIH^{fl/fl}$xVillinCre mice in comparison to their wildtype littermates.

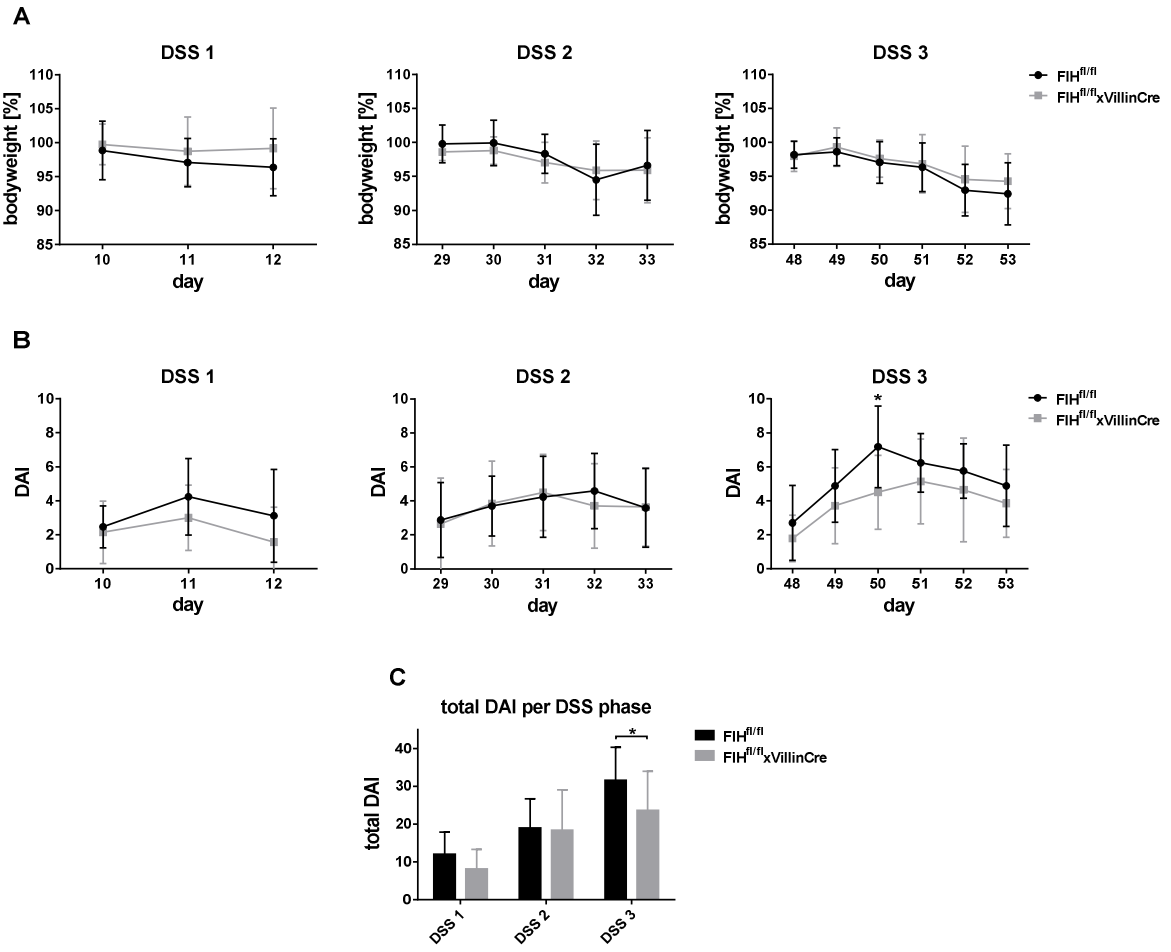

Figure 6-9: Colitis progress is reduced in FIH knockout mice of the AOM-DSS-DMOG model. A: Percentage of bodyweight of the DSS-treated mice during the three DSS periods. FIH$^{fl/fl}$ mice (black) are compared with the FIH knockout animals (grey). B: Calculated DAIs during the DSS-treatment. FIH$^{fl/fl}$xVillinCre mice (grey) and their wildtype littermates (black) are compared to each other. C: The sum of DAIs from one DSS phase per mouse makes the total DAI. This calculation was done for FIH$^{fl/fl}$ and FIH$^{fl/fl}$xVillinCre mice (mean ± SD, n = 17/14).

Once again, the outcome of the DSS-induced chronic colitis was the development of colorectal cancer. DSS-treated experimental mice showed a strong tumor growth in comparison to the control animals (see Figure 6-10 A and B) but without any differences between FIH$^{fl/fl}$ and FIH$^{fl/fl}$xVillinCre mice. Again, the amount and size of the tumors led to an increase of the colon weight at constant length (see Figure 6-10 C and D).

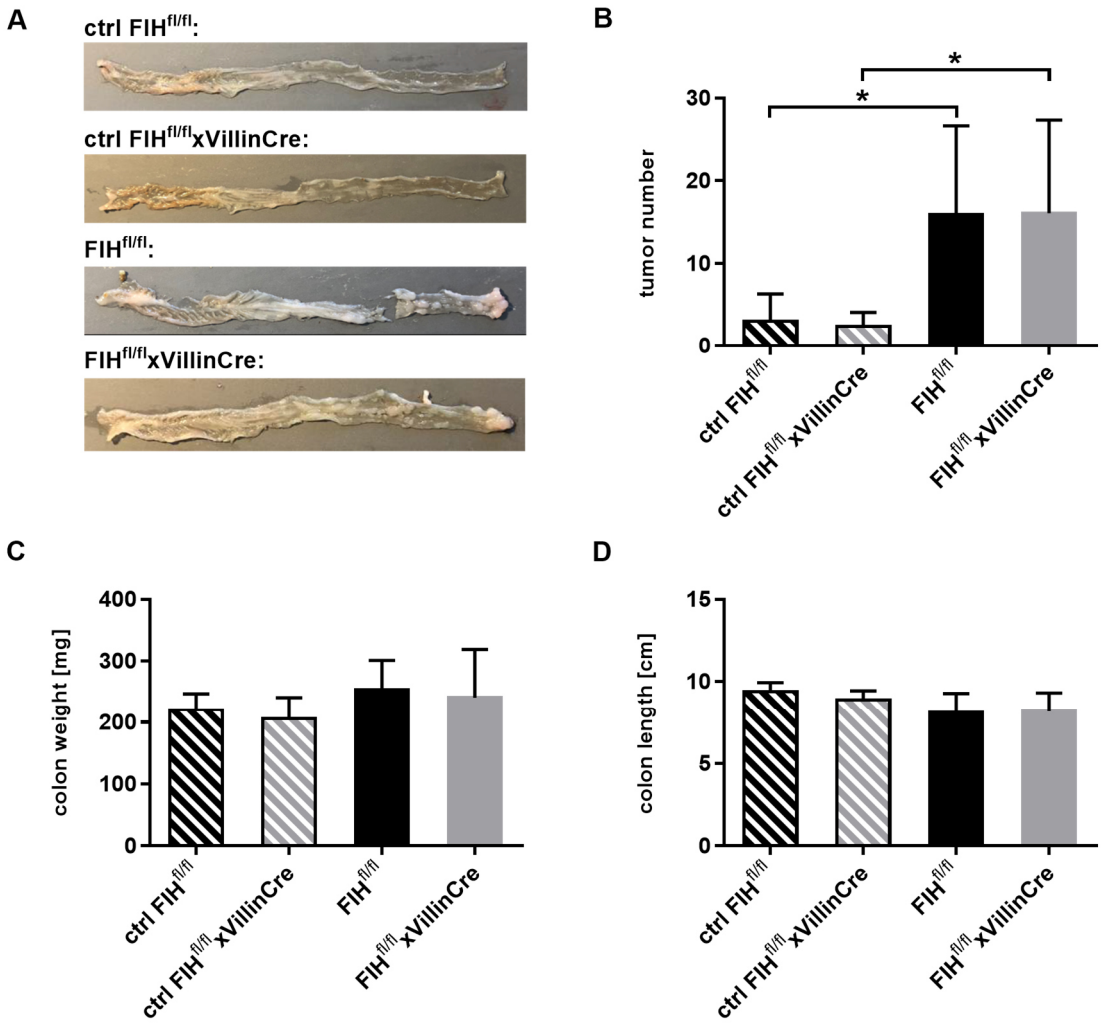

Figure 6-10: Tumor growth in the murine AOM-DSS-DMOG model. A: Exemplary photographs of the opened colon from control and AOM-DSS-DMOG-treated mice after fecal remains were washed out. B: Tumors were counted manually during preparation of control and DSS-treated, FIH$^{fl/fl}$ and FIH$^{fl/fl}$xVillinCre animals. C: Dissected colons were weighed for all mouse groups. Growth of big tumors resulted in the tendency of an increased colon weight in DSS-treated animals. D: Lengths of the dissected and cleaned colons. B - D: Mean ± SD, n = 5/5/14/16.

H&E staining of about 1 cm of distal colon tissue from AOM-DSS-DMOG-treated mice showed no differences between FIH$^{fl/fl}$xVillinCre and FIH$^{fl/fl}$ mice. Again, the tumors looked similar between the genotypes and the crypt structure of non-tumor areas was as intact as in control animals (see Figure 6-11).

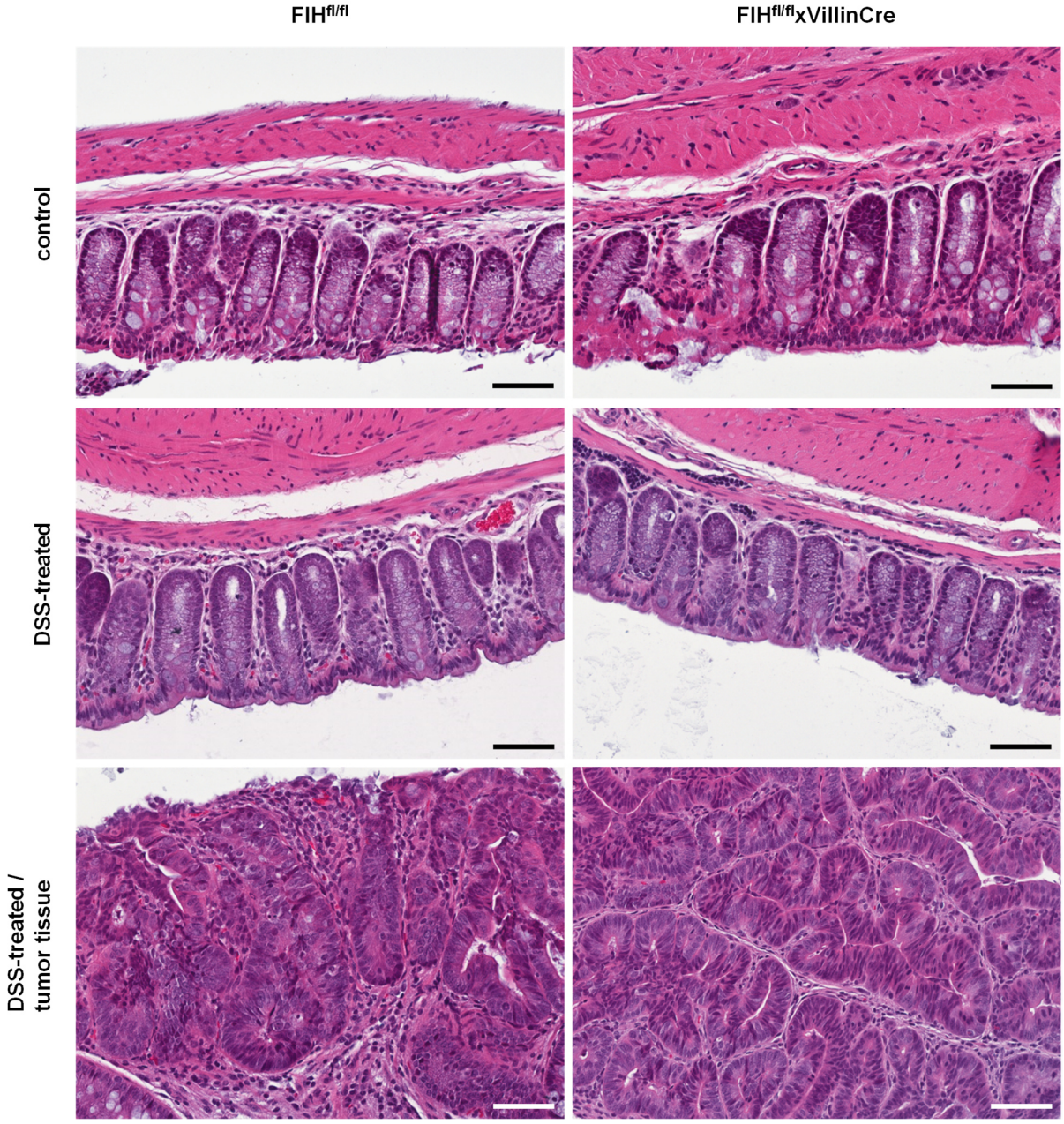

Figure 6-11: H&E stained colon tissue from AOM-DSS-DMOG-treated mice. Crypt structure of control and DSS-treated and FIH$^{fl/fl}$ and FIH$^{fl/fl}$xVillinCre mice two weeks after acute colitis are shown. Like in AOM-DSS-treated animals, tumors are characterized by a chaotic crypt structure. Scale bar = 50 µm.

6.4 Effects of AOM-DSS(-DMOG) treatment on splenic immune cells

Flow cytometry analysis shows the composition of immune cells inside the spleen during an inflammatory response. In the AOM-DSS model, there is no acute inflammation when the mice are sacrificed. But as the tendency to an enlarged spleen could be observed during the preparation of the experimental animals (see Figure 6-12), a flow cytometry analysis was performed to analyze the cellular composition of the spleens after AOM-DSS treatment.

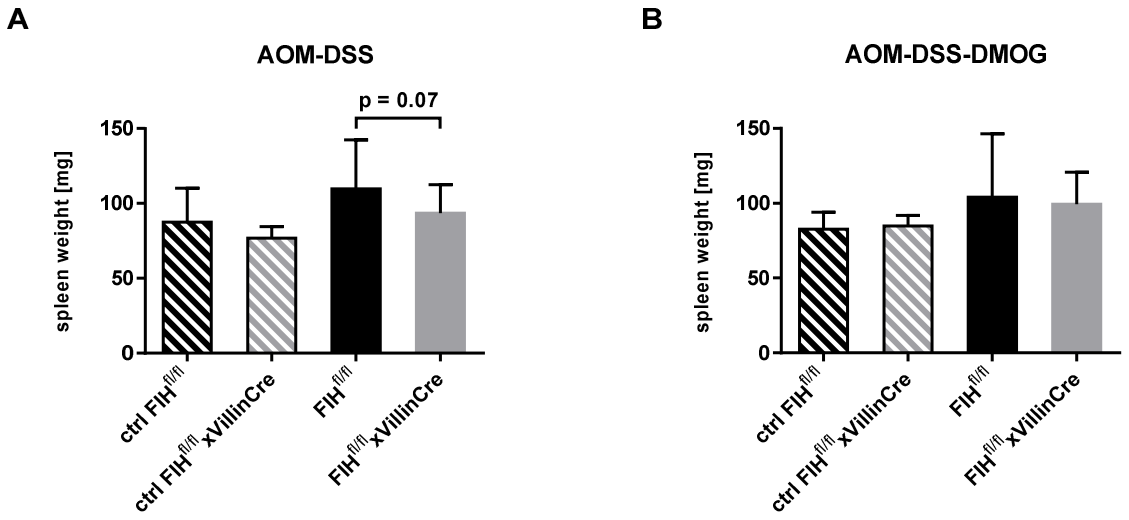

Figure 6-12: Spleen weight of experimental mice. A: The dissected spleens of mice from the AOM-DSS model were weighed before the cells were singularized. Striped bars represent control animals that were not treated with DSS. Filled bars show the spleen weight of DSS-treated FIH$^{fl/fl}$ and FIH$^{fl/fl}$xVillinCre animals (mean ± SD, n = 6/6/19/19). B: Dissected spleens from the AOM-DSS-DMOG model were also weighed before further usage (mean ± SD, n = 5/5/13/15).

Monocytes, which are CD11b$^+$, and dendritic cells, which are CD11c$^+$, were found in the spleen of FIH$^{fl/fl}$ mice to the same percentage (3 - 5%) as in FIH$^{fl/fl}$xVillinCre mice, irrespective of the DSS treatment (see Figure 6-13 A and B). However, with respect to the activity of these cells, spleens of DSS-treated FIH$^{fl/fl}$ and FIH$^{fl/fl}$xVillinCre mice showed an increased activation of monocytes compared to untreated control animals (CD11b$^+$CD86$^+$, see Figure 6-13 C). The activity of monocytes hereby seemed to be induced by DSS treatment, but unchanged by the FIH knockout. No differences at all were found in the activation of dendritic cells (CD11c$^+$CD86$^+$, see Figure 6-13 D).

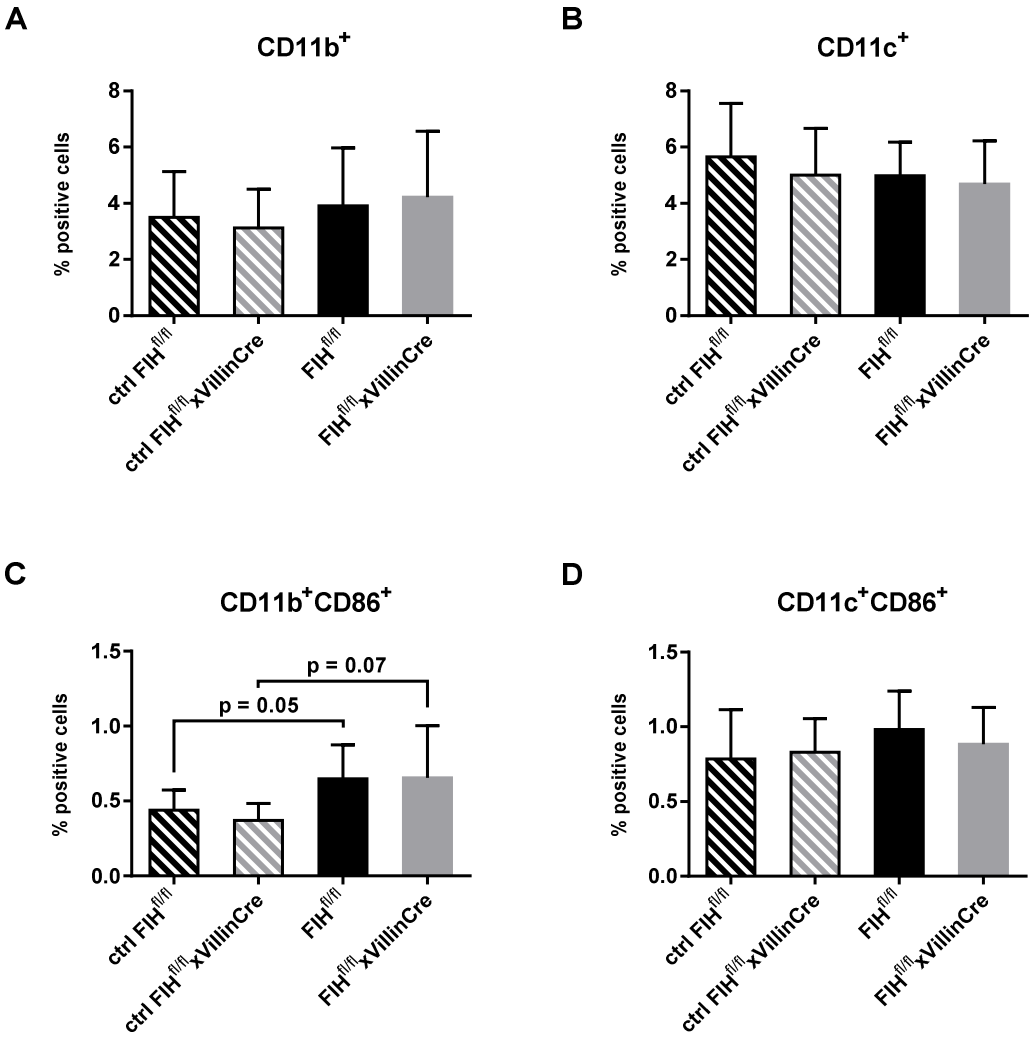

Figure 6-13: Flow cytometry analysis of the spleens of AOM-DSS-treated mice. Gates were set by testing only CD11b$^+$ and CD11c$^+$ cells for CD86 signals. A: Percentage of CD11b$^+$ cells in the spleen. B: Percentage of CD11c$^+$ cells in the singularized spleen cells. C: Percentage of splenic cells that were CD11b and CD86 positive. D: Percentage of CD11c$^+$ and CD86$^+$ cells. All: Mean ± SD, n = 6/6/14/14.

The same tendency was seen by the flow cytometry results of the AOM-DSS-DMOG-treated mice (statistical analysis needs to be handled with care here as there were too few mice): The number of active immune cells (CD11b$^+$CD86$^+$ and CD11c$^+$CD86$^+$) increased due to DSS treatment, although without significant differences between FIH$^{fl/fl}$ and FIH$^{fl/fl}$xVillinCre mice (see Figure 6-14 C and D). The number of activated dendritic cells (CD11c+CD86+, see Figure 6-14 D) increased significantly in wildtype animals which might be a hint to a stronger immune response in these animals compared to the FIH knockout mice. The amount of monocytes and dendritic cells (CD11b$^+$ and CD11c$^+$ cells) was not changed at all in all animal groups (see Figure 6-14 A and B).

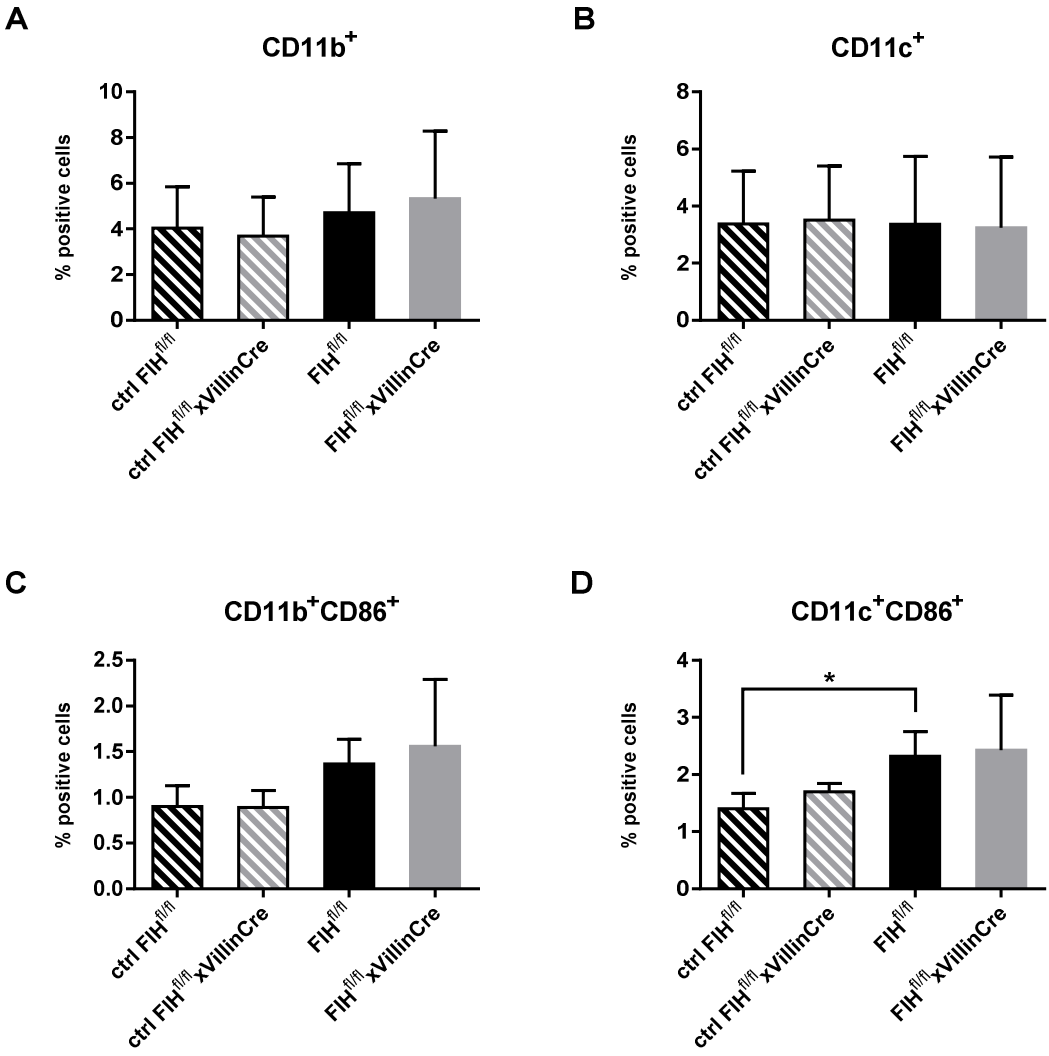

Figure 6-14: Flow cytometry analysis of spleen cells from mice of the AOM-DSS-DMOG model. Gates were set by testing only CD11b$^+$ and CD11c$^+$ cells for CD86 positivity. A: Percentage of CD11b$^+$ cells in the spleen. B: Percentage of CD11c$^+$ cells in all spleen cells. C: Percentage of splenic CD11b$^+$CD86$^+$ cells. D: Percentage of active dendritic cells (CD11c$^+$CD86$^+$). All: Mean ± SD, n = (2/2/4/5), therefore statistical analysis needs to be handled with care.

6.5 Immune response in the colon of AOM-DSS(-DMOG)-treated mice

Although there was a 2-week regeneration phase, in which tumors were expected to develop, remains of the inflammatory response of the mice against the third DSS-induced colitis period were still visible. This response was observable e.g. in an infiltration of immune cells like macrophages into the colon tissue. The mRNA expression of *F4/80* (or *Adgre1* gene), which is a marker for macrophages, was increased 5-fold in DSS-treated mice

compared to their littermates that got normal drinking water (see Figure 6-15 A). The FIH knockout seemed to have no effect on macrophage infiltration measured by qPCR in the AOM-DSS model as there was no difference in the *F4/80* expression between FIH$^{fl/fl}$ and FIH$^{fl/fl}$xVillinCre mice.

The RNAseq data also showed no significant changes in *F4/80* expression between the genotypes, but there was a tendency to a lower macrophage infiltration in the colon with DSS treatment in the FIH$^{fl/fl}$xVillinCre mice in comparison to the wildtypes (see Figure 6-15 B). In control animals, the difference in *F4/80* expression between the genotypes was gone.

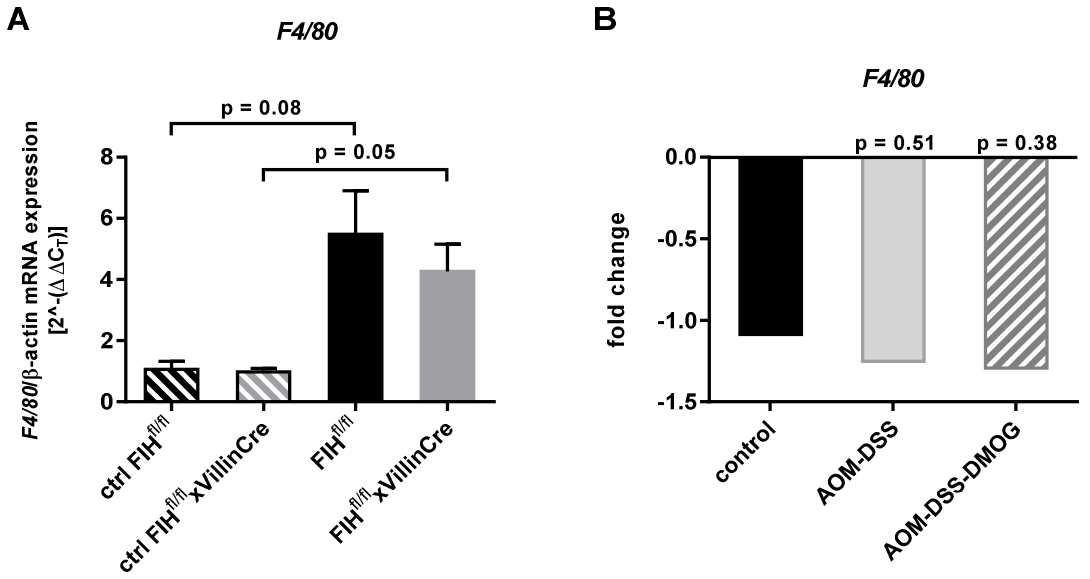

Figure 6-15: Increased expression of *F4/80* analyzed by qPCR and RNAseq. A: Isolated mRNA from the first AOM-DSS experiment was quantified regarding *F4/80* expression. *F4/80* values were normalized to β-actin expression and compared between control and DSS-treated animals as well as the genotypes (mean ± SD, n = 3/3/6/6). B: Analysis of the RNAseq data resulted in a reduced *F4/80* expression in FIH$^{fl/fl}$xVillinCre mice in comparison to their wildtype littermates from the three treatment groups (mean, n = 4/3/4).

An immunohistochemical staining for F4/80 was performed in the colon tissue of untreated and DSS-treated mice of the AOM-DSS and AOM-DSS-DMOG model. In untreated control mice, infiltrated macrophages were hardly found. Only few single F4/80 positive cells could be detected by the immunohistochemical staining (see Figure 6-16).

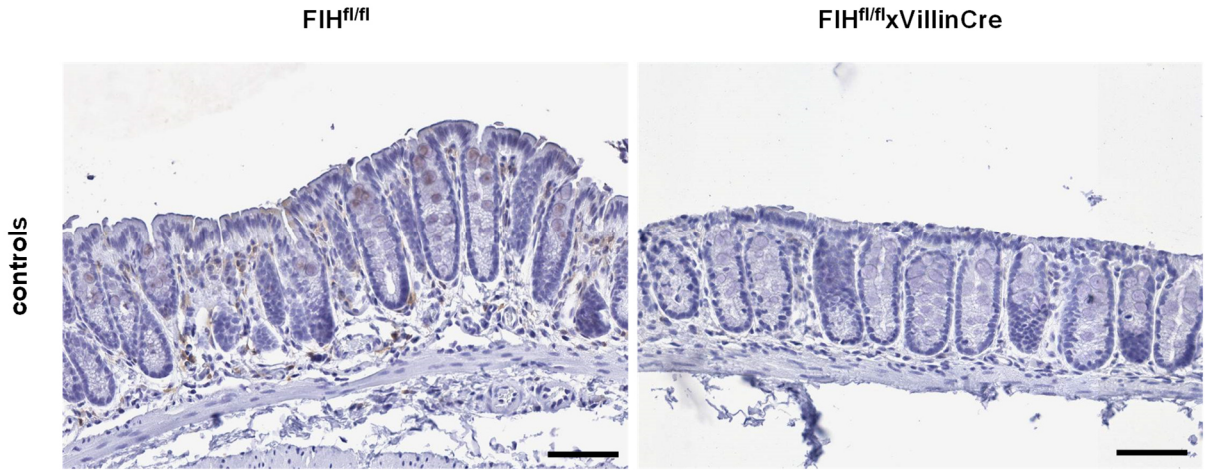

Figure 6-16: Immunohistochemical staining of F4/80 in control animals. Infiltrated macrophages were hardly detectable in the colons of untreated FIH$^{fl/fl}$ and FIH$^{fl/fl}$xVillinCre mice. Scale bar = 50 µm.

The distal colon regions of AOM-DSS-treated FIH$^{fl/fl}$xVillinCre mice were less infiltrated than those of FIH$^{fl/fl}$ mice (see Figure 6-17), corresponding to the lower DAI in the third DSS phase and the mRNA data from above. Also in colon tumors, the epithelial FIH knockout led to a lower amount of F4/80-positive cells in the tumor tissue compared to wildtype animals (see Figure 6-17). But not only had the total amount of infiltrated macrophages differed between the genotypes: also the affected layers were different. F4/80-positive cells were found mainly in the *Tunica mucosa* of the FIH$^{fl/fl}$xVillinCre mice, while in FIH$^{fl/fl}$ mice, they infiltrated also the *Tela submucosa*.

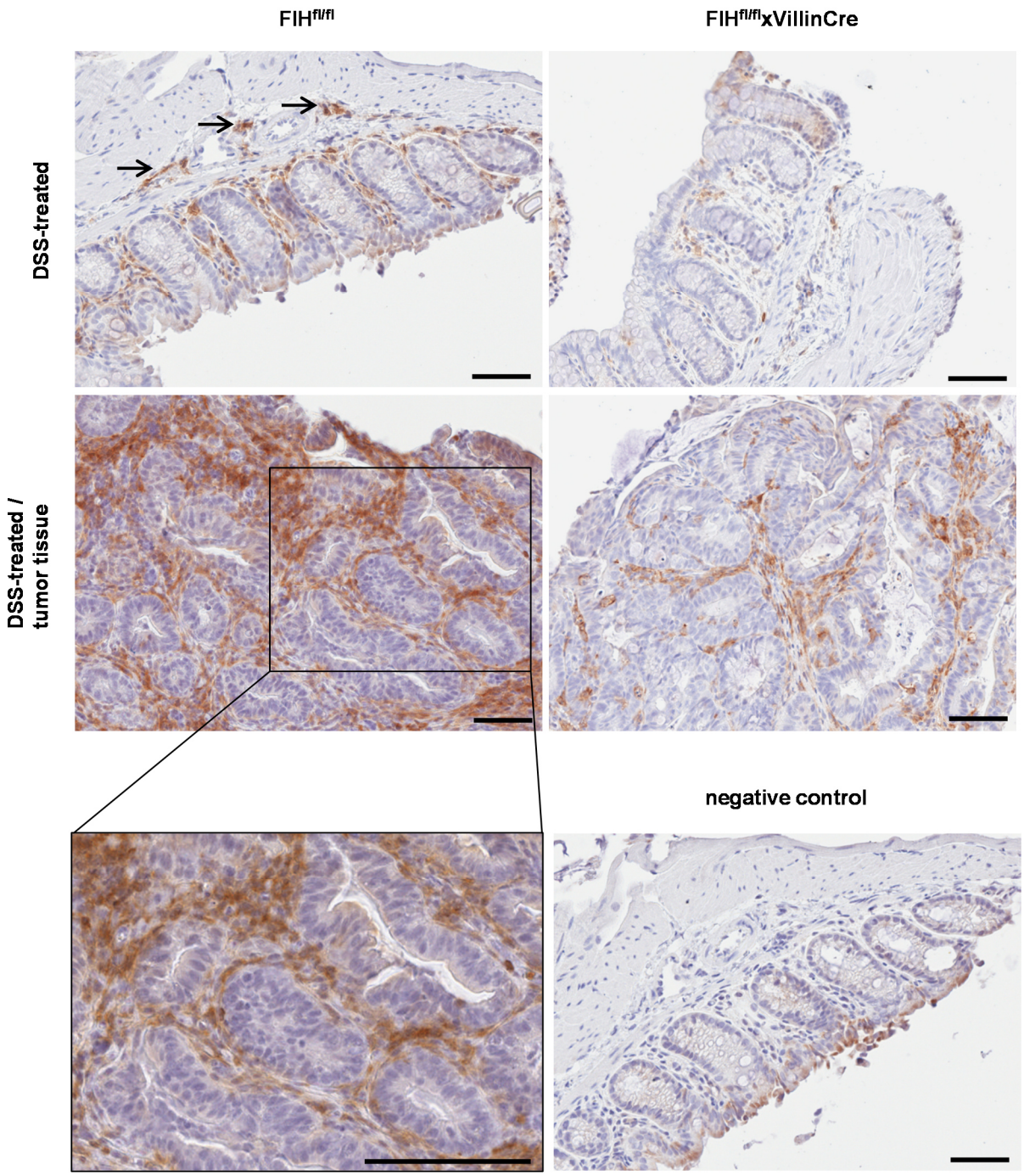

Figure 6-17: The number of F4/80-positive cells in DSS-AOM-treated colons was increased in wildtype compared to FIH knockout animals. Shown are representative immunohistochemical stainings of F4/80 in distal colon sections and colon tumors of AOM-DSS-treated mice. Black arrows indicate myeloid cells that migrated deeper into the tissue than into the *Tunica mucosa*. Scale bar = 50 µm.

The immunohistochemical staining of F4/80 in AOM-DSS-DMOG-treated mice showed the same results as the mouse model without DMOG but with a lower total amount of F4/80-positive cells. Again, wildtype animals had a much stronger immune reaction due to the DSS-treatment in normal colon tissue and inside the tumors than FIH knockout mice (see Figure 6-18).

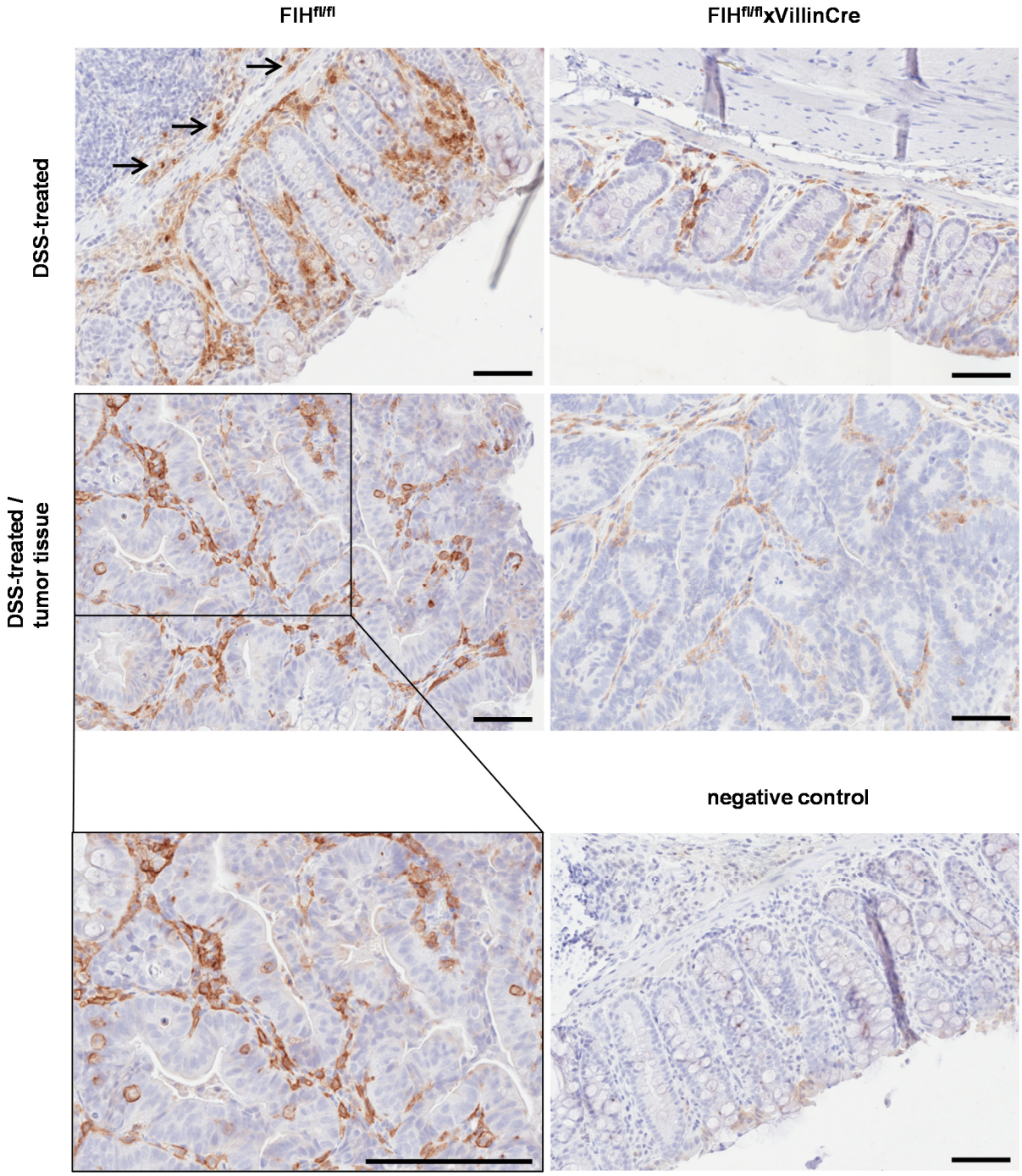

Figure 6-18: F4/80 expression was stronger in AOM-DSS-DMOG-treated wildtype than FIH knockout mice. Shown are representative immunohistochemical stainings of F4/80 in distal colon sections and tumors of AOM-DSS-DMOG-treated mice. Black arrows show macrophages that infiltrated not only the *Tunica mucosa* but also the *Tela submucosa*. Scale bar = 50 µm.

As many different genes are responsible for the immune response of an organism, the RNAseq data were analyzed with regard to this certain topic. Several immune response associated GO terms appeared in the set of downregulated genes in AOM-DSS-treated

FIH$^{fl/fl}$xVillinCre mice compared to FIH$^{fl/fl}$ mice (see Table 6-1), which confirmed the less pronounced immune reaction due to the FIH knockout.

Table 6-1: In AOM-DSS-treated FIH$^{fl/fl}$xVillinCre mice downregulated GO terms regarding the immune response. Listed are immune response associated GO terms that appeared in the set of downregulated genes in AOM-DSS-treated FIH$^{fl/fl}$xVillinCre (KO) mice compared to FIH$^{fl/fl}$ (WT) mice.

GO term	Enrichment of downregulated genes in KO vs. WT mice	p-value
'immune response'	1.7669	0.003162
'defense response'	2.1084	0.000005
'immune response-activating signal transduction'	2.4570	0.030917
'acute inflammatory response'	3.3516	0.033551
'B cell mediated immunity'	3.1573	0.041678
'immune response-regulating signaling pathway'	2.3013	0.042603

In the AOM-DSS-DMOG model, the FIH$^{fl/fl}$xVillinCre mice showed GO terms overrepresented in the set of downregulated genes compared to FIH$^{fl/fl}$ mice that were similar to those in Table 6-1 (see Table 6-2). Independently from the model, FIH$^{fl/fl}$xVillinCre animals seemed to have a reduced inflammatory response to the DSS treatment compared with their wildtype littermates. The values for fold enrichment of downregulated genes of the GO terms that appeared in both models were of comparable values with 1.7669 and 1.9993 for the 'immune response' and 2.1084 and 2.6274 for the 'defense response', respectively.

Table 6-2: RNAseq data showed downregulated immune response genes in FIH$^{fl/fl}$xVillinCre mice (AOM-DSS-DMOG model). Shown are GO terms that are associated with the immune response and appeared in the set of downregulated genes in AOM-DSS-DMOG-treated FIH$^{fl/fl}$xVillinCre (KO) mice compared to FIH$^{fl/fl}$ (WT) mice.

GO term	Fold enrichment of downregulated genes in KO vs. WT mice	p-value
'immune response'	1.9993	0.005549
'defense response'	2.6274	0.000030
'immune system process'	1.9642	0.000327
'defense response to bacterium'	3.4876	0.008033
'inflammatory response'	2.5111	0.008445
'T cell activation'	2.4353	0.099980

Focusing on single gene expression, many immune response associated genes could be found that were substantially downregulated in FIH$^{fl/fl}$xVillinCre mice compared to the wildtype animals. These genes were e.g. *Nos2* (*Inos*; inducible NO synthase) and arginase-1 (*Arg1*), which are expressed by macrophages and normally enhanced in inflammation, *Cd4* and forkhead box P3 (*Foxp3*), markers for regulatory T-cells, *Cd8a*, specific for cytotoxic T-cells, and *Il6*, an IBD-associated pro-inflammatory cytokine. These genes were all substantially downregulated in AOM-DSS-DMOG-treated FIH$^{fl/fl}$xVillinCre mice compared to their wildtype littermates with a fold change of -2 to -6 (see Figure 6-19). In control animals, these genes showed no changes in their expression between the different genotypes (maximum fold change was -2).

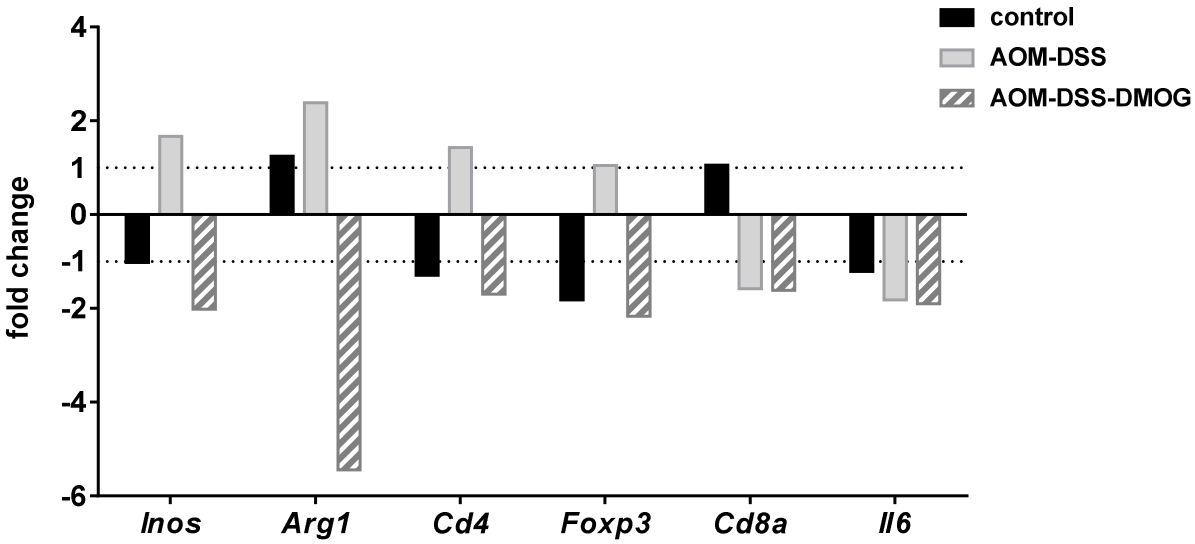

Figure 6-19: Fold change values from the RNAseq data for immune response genes. Fold changes represent the down- or upregulation of certain immune response genes in FIH$^{fl/fl}$xVillinCre mice in comparison to FIH$^{fl/fl}$ animals (n = 4/3/4).

An IPA of the RNAseq data resulted in a list of transcription factors, which were activated (positive z-score) or inhibited (negative z-score) in their transcriptional activity, assessed by the expression of their target molecules from an integrated dataset. This allows an indirect analysis of protein activity via the gathered RNAseq data. Some of these transcription factors, e.g. interferon regulatory transcription factors (IRFs), belonged to the headword immune response and showed an inhibition in AOM-DSS-treated FIH$^{fl/fl}$xVillinCre mice compared to FIH$^{fl/fl}$ mice (see Figure 6-20). Other transcription factors have tumor suppressing qualities, e.g. SRY-box 4 (SOX4), E2F transcriptions factor 3 (E2F3), tumor

protein p53 (TP53) and lysine-specific methyltransferase 2D (KMT2D), or metabolic functions as Kruppel-like factor 3 (KLF3). All these proteins have an absolute value of the z-score larger than 2. This value is independent from the expression fold change of the transcription factors themselves which had not significantly changed.

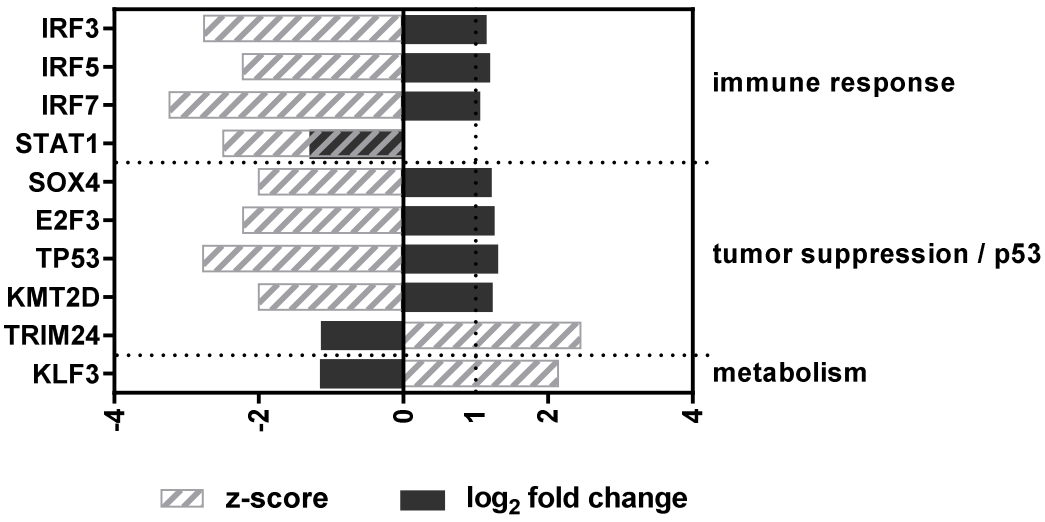

Figure 6-20: IPA results of the RNAseq data from the AOM-DSS model. All transcription factors that appeared in the IPA due to a z-score higher than 2 or below -2 (grey) are represented. A z-score in this range means a significant increase (positive z-score) or decrease (negative z-score) in expression of the downstream genes regulated by this transcription factor. Compared are FIH$^{fl/fl}$xVillinCre mice with FIH$^{fl/fl}$ mice. Fold changes of the transcription factor expression are illustrated as black bars (n = 3).

6.6 Levels of HIF and hypoxia in AOM-DSS(-DMOG)-treated mice

Pimonidazole was injected into the mice to enable staining of hypoxic areas in the colon tissue. The luminal part of the colon showed a positive staining in the AOM-DSS- and AOM-DSS-DMOG-treated mice (see Figure 6-21 and Figure 6-22, upper row). Thus, the oxygen level in the colon epithelium was low. Luminal Hypoxyprobe^{TM}-1 staining was not affected by the epithelial FIH knockout in the FIH$^{fl/fl}$xVillinCre mice. Tumor areas were completely but only slightly positive for Hypoxyprobe^{TM}-1 staining (see Figure 6-21 and Figure 6-22, middle row). Primarily the outer parts of a tumor showed a signal for hypoxia. Again, there were no differences between FIH$^{fl/fl}$ and FIH$^{fl/fl}$xVillinCre mice, neither in the AOM-DSS nor in the AOM-DSS-DMOG mouse model.

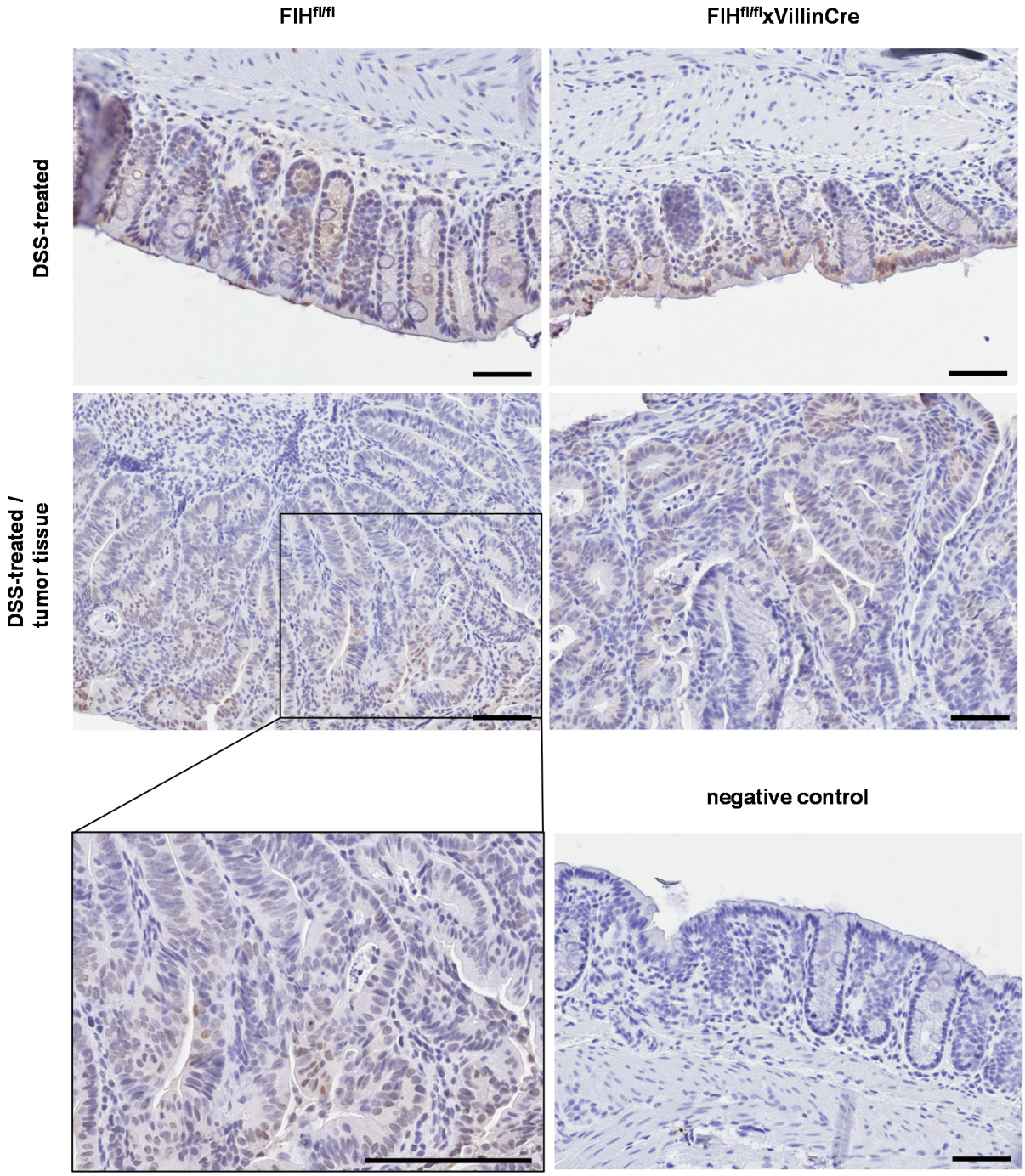

Figure 6-21: Immunohistochemical Hypoxyprobe™-1 staining of colon tissue of AOM-DSS-treated mice. Animals were injected with pimonidazole 1 hr before preparation. Hypoxic areas show a brownish staining. The negative control proves the specificity of the faint brownish staining in antibody-treated samples. Normal colon crypt structures as well as tumor regions are shown from FIH$^{fl/fl}$ and FIH$^{fl/fl}$xVillinCre animals. Scale bar = 50 µm.

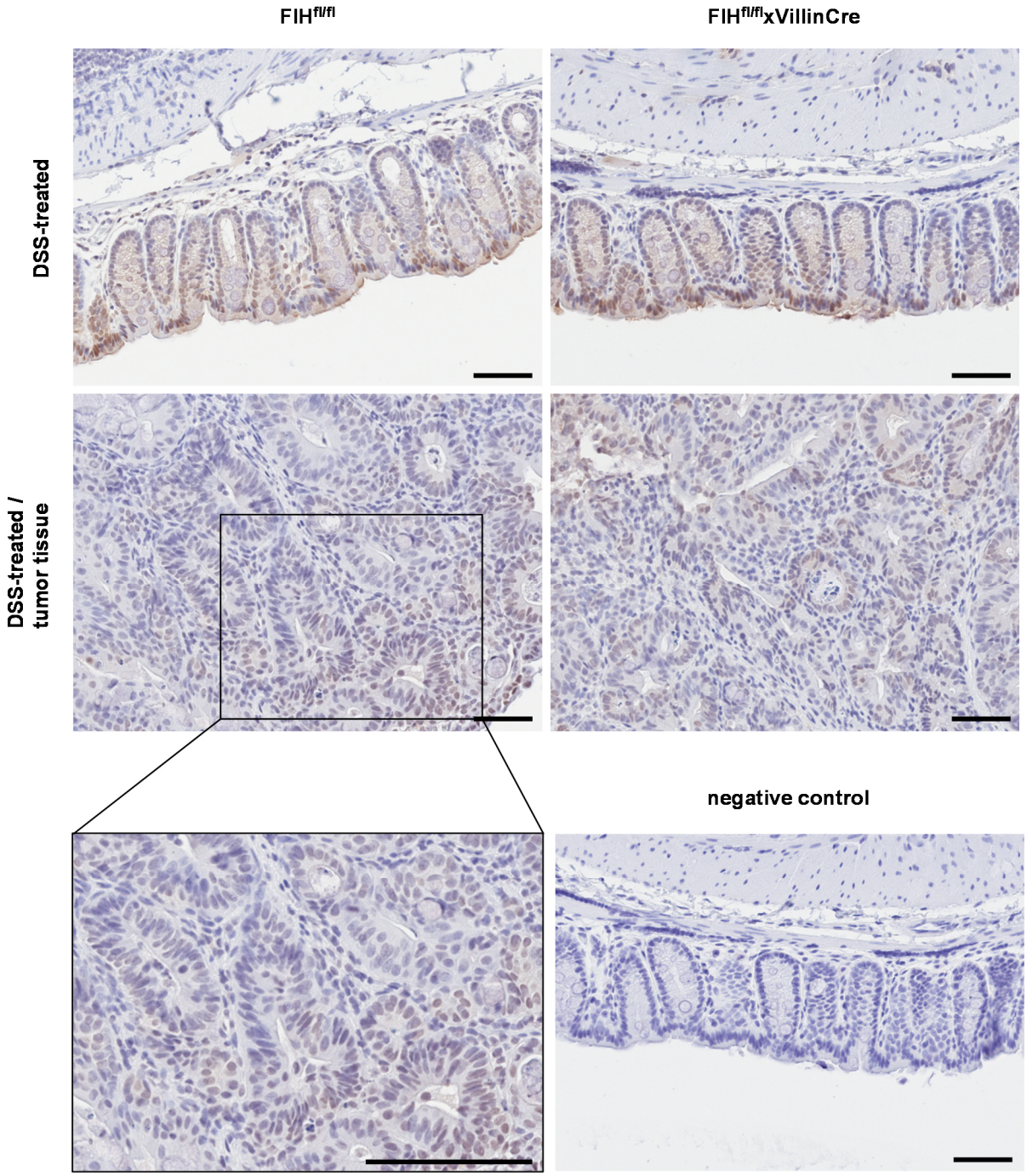

Figure 6-22: Immunhistochemical Hypoxyprobe™-1 staining of colon tissue of AOM-DSS-DMOG-treated mice. 1 hr before preparation, mice were injected with pimonidazole to enable the staining of hypoxic regions. The negative control reveals the specificity of the antibodies. Here, colon crypt structures and tumor areas from FIH$^{fl/fl}$ and FIH$^{fl/fl}$xVillinCre mice are shown. Scale bar = 50 µm.

HIF-1α and HIF-2α are known to accumulate in the nucleus of hypoxic cells. Tissue areas positive for Hypoxyprobe^{TM}-1 staining are therefore supposed to contain more HIF positive stained cells than tissue with a normal oxygen level. DAB staining of the HIF-1α and HIF-2α proteins in the colon of AOM-DSS-DMOG-treated mice confirmed this assumption. The epithelial cells in the luminal part of the colon were mainly positive for HIF-1α while the cell nuclei that were localized deeper, in the mucosa and submucosa, showed no signal for HIF-1α (see Figure 6-23). The same results were gained by detection of HIF-2α protein (see Figure 6-24). In colon tumor tissue, HIF-1α and HIF-2α positive cells were mainly found in the outer parts of a tumor. Here, the signals for HIF-1α and HIF-2α were stronger than the faint Hypoxyprobe^{TM}-1 staining.

In colon crypts, the amount of HIF-1α as well as of HIF-2α was the same in FIH$^{fl/fl}$xVillinCre mice and their wildtype littermates (see Figure 6-23 and Figure 6-24, upper panels). Thus, the lack of FIH led to no changes in stabilization of the HIF-α subunit in the colon epithelium. In tumor tissue, there were no differences between the genotypes, either. Similar results were gained by stainings of colon tissue from AOM-DSS-treated mice (see supplementary Figure 9-1 and Figure 9-2).

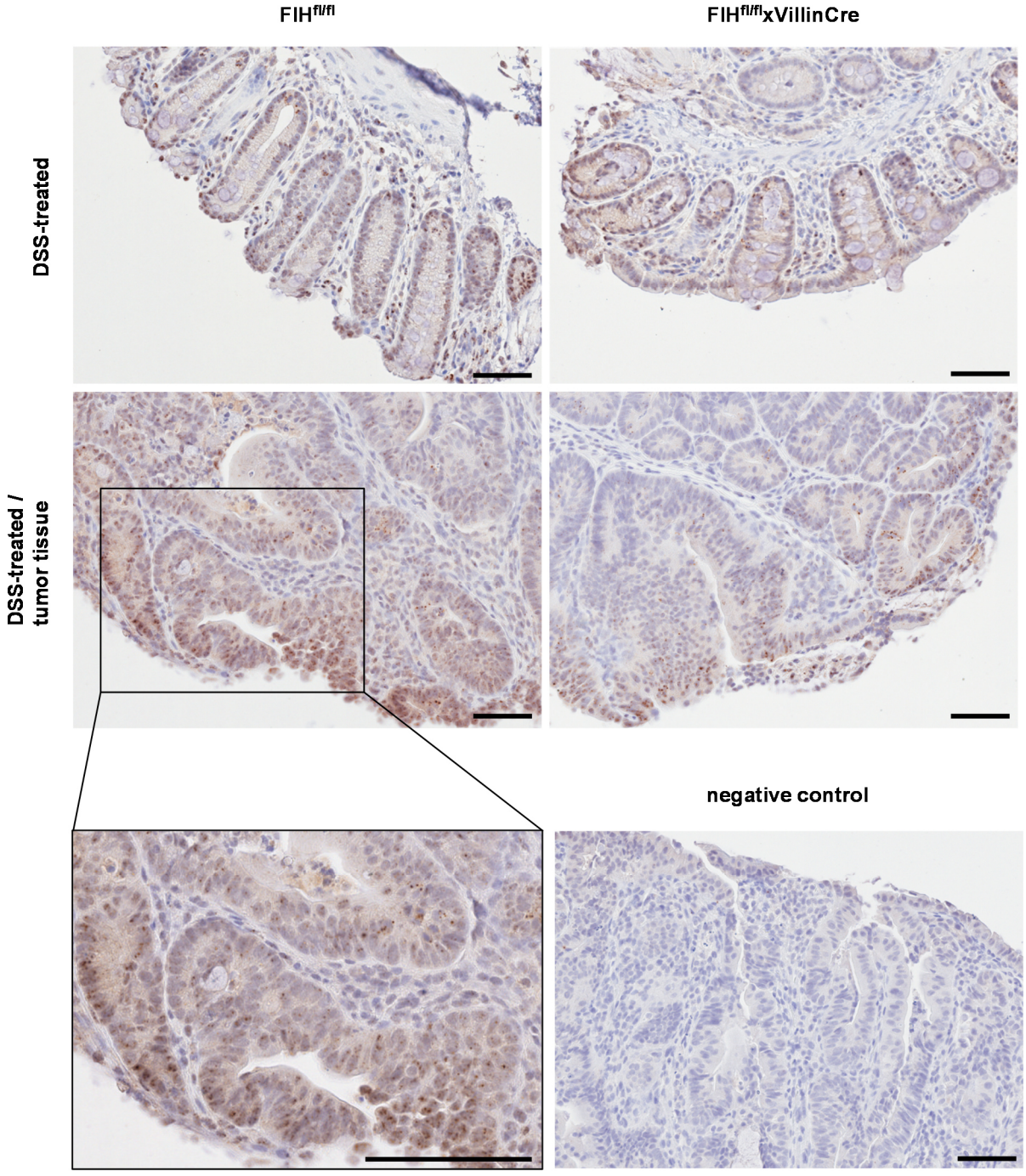

Figure 6-23: HIF-1α protein staining in AOM-DSS-DMOG-treated mice. Distal colon sections of AOM-DSS-treated FIH$^{fl/fl}$ and FIH$^{fl/fl}$xVillinCre mice showed HIF-1α positive cell nuclei in the epithelium. In the tumor tissues, HIF-1α can be found mainly in the outer parts of the tumors. In the negative control, no unspecific staining was visible at all. Scale bar = 50 µm.

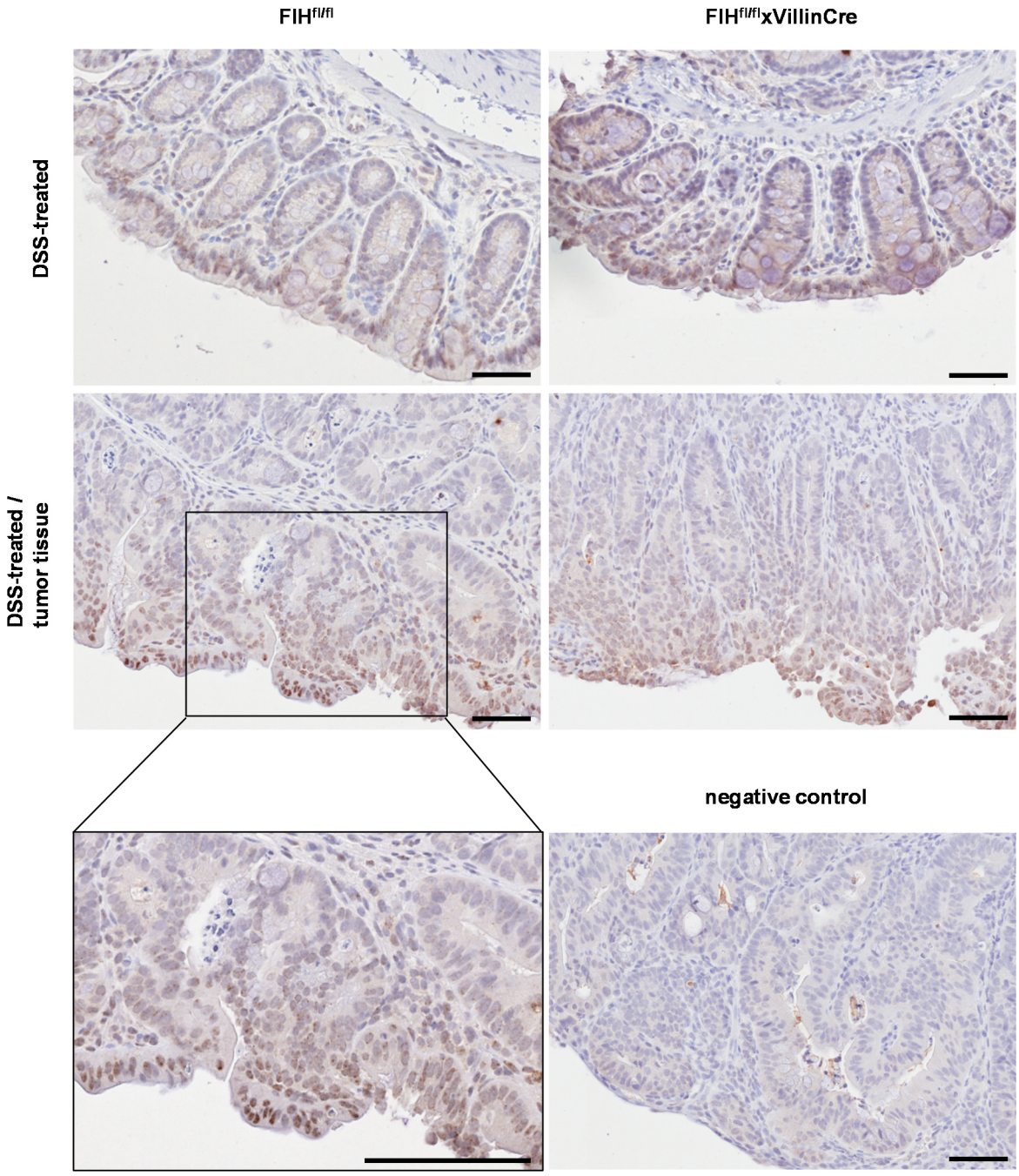

Figure 6-24: Immunohistochemical staining of HIF-2α in mice from the AOM-DSS-DMOG model. As for HIF-1α, positive nuclei were found mainly on the luminal side of the colon of FIH$^{fl/fl}$ and FIH$^{fl/fl}$xVillinCre mice. The tumors showed more HIF-2α positive cells in the outer regions than in the middle of the tumor. The negative control proved the specificity of the antibodies. Scale bar = 50 µm.

Additionally to the immunohistochemical protein staining of HIF-1α and -2α, *in situ* hybridization with RNAscope® was conducted to have a look on mRNA expression changes. First, the negative control lacking the probes for *Hif1a* and *Hif2a* revealed the specificity of the staining (see supplementary Figure 9-3). Detection of *Hif1a* expression in tumor tissue of

AOM-DSS-DMOG-treated FIH$^{fl/fl}$xVillinCre and FIH$^{fl/fl}$ mice showed a high amount of HIF-1α mRNA expressing cells (see Figure 6-25 upper panel). *Hif1a* positive cells were found in the complete tumor areas and did not seem to be cell type specific. *Hif2a* positive cells, in contrast, built a specific pattern like they were all close to blood vessels (see Figure 6-25 lower panel). This staining was also observed in the complete tumors. No differences between FIH$^{fl/fl}$xVillinCre and FIH$^{fl/fl}$ mice could be observed with respect to *Hif1a* and *-2a* mRNA expression. The same results were observed using samples from the AOM-DSS model (see supplementary Figure 9-4).

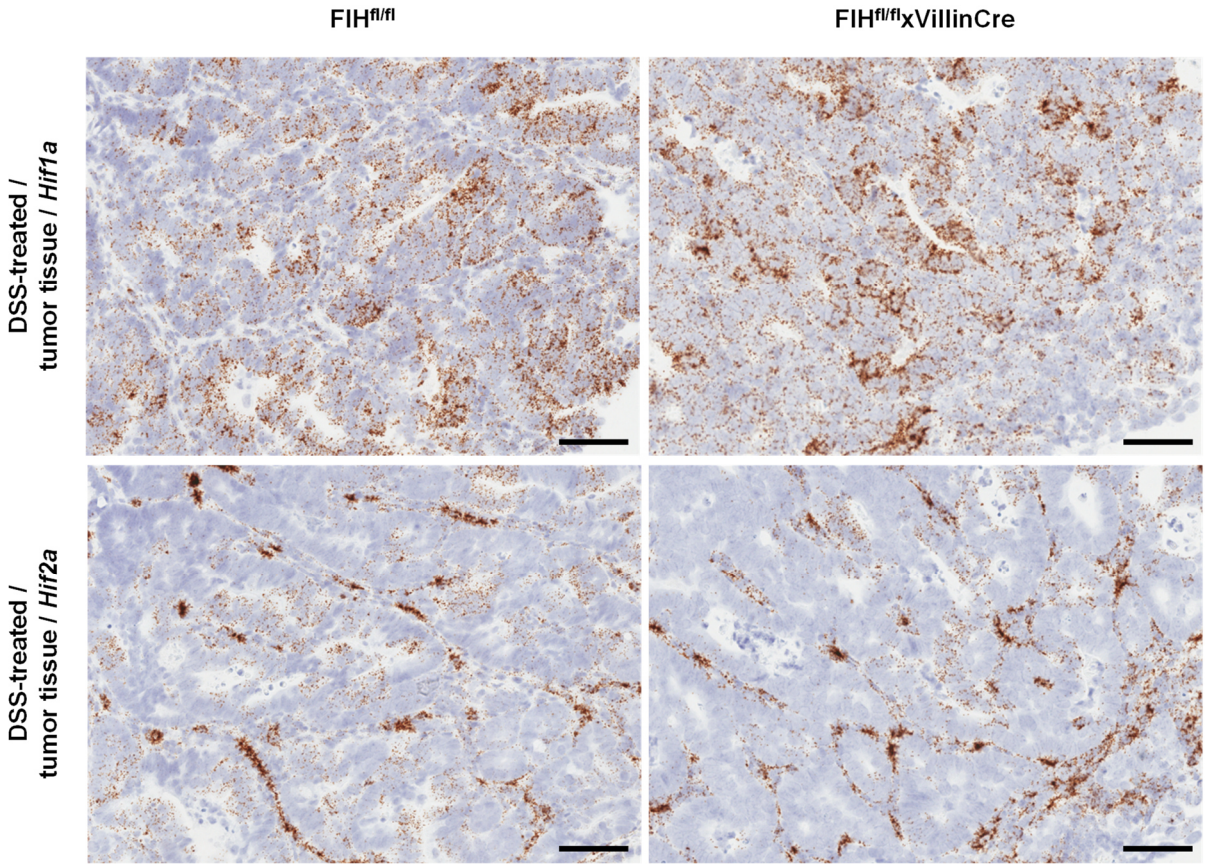

Figure 6-25: RNAscope® for *Hif1a* and *Hif2a* in tumor tissue of AOM-DSS-DMOG-treated mice. *Hif1a* is expressed throughout the complete tumor tissue in FIH$^{fl/fl}$ and FIH$^{fl/fl}$xVillinCre mice. *Hif2a* in contrast is expressed only in endothelial cells. Scale bar = 50 µm.

6.7 Protein-protein interaction of HIF and FIH via co-immunoprecipitation

An *in vitro* co-immunoprecipitation was conducted to verify the interaction between the fluorophore-tagged FIH and its substrate HIF-1α. Therefore, cells were transfected with the mCitrine-HIF-1α construct resulting in the expression of the HIF-1α protein tagged with the fluorophore mCitrine. The same cells were transfected with mCherry-FIH that led to production of mCherry-tagged FIH protein. mCitrine-HIF-1α was then pulled by GFP-specific microbeads. As the same protein lysate contained mCherry-tagged FIH, FIH was pulled together with HIF-1α if the interaction took place. mCherry was then detected after SDS-PAGE loaded with the microbead prey and subsequent transfer to a Western Blot membrane.

The detection of mCherry verified the interaction of tagged HIF-1α and FIH *in vitro* after overexpression of both plasmids in HEK293T cells (see Figure 6-26 A). While there was a clear band for FIH-mCherry that had the expected size of about 70 kDa (~40 kDa FIH + ~30 kDa fluorophore) in the lane with mCitrine-HIF-1α + FIH-mCherry transfected cells, the mCherry-FIH construct generated two bands of different sizes: ~65 and ~80 kDa.

There was no mCherry detected in the Co-IP of negative controls with mCitrine-HIF-1α + mCherry-C1 (empty vector) and soluble mCitrine + mCherry-FIH. The positive control Co-IP of mCitrine-HIF-1α + mCherry-ARNT, showed the expected mCherry-ARNT band of about 120 kDa (ARNT: ~90 kDa).

Detection of mCherry with an RFP-specific antibody and mCitrine with a GFP-specific antibody in protein lysates of the transfected cells revealed the expression of the mCitrine and mCherry constructs (see Figure 6-26 C and D). Fluorophores alone were supposed to have a size of about 30 kDa, mCitrine-HIF-1α of about 150 kDa (HIF-1α: ~120 kDa) and FIH-mCherry of ~70 kDa.

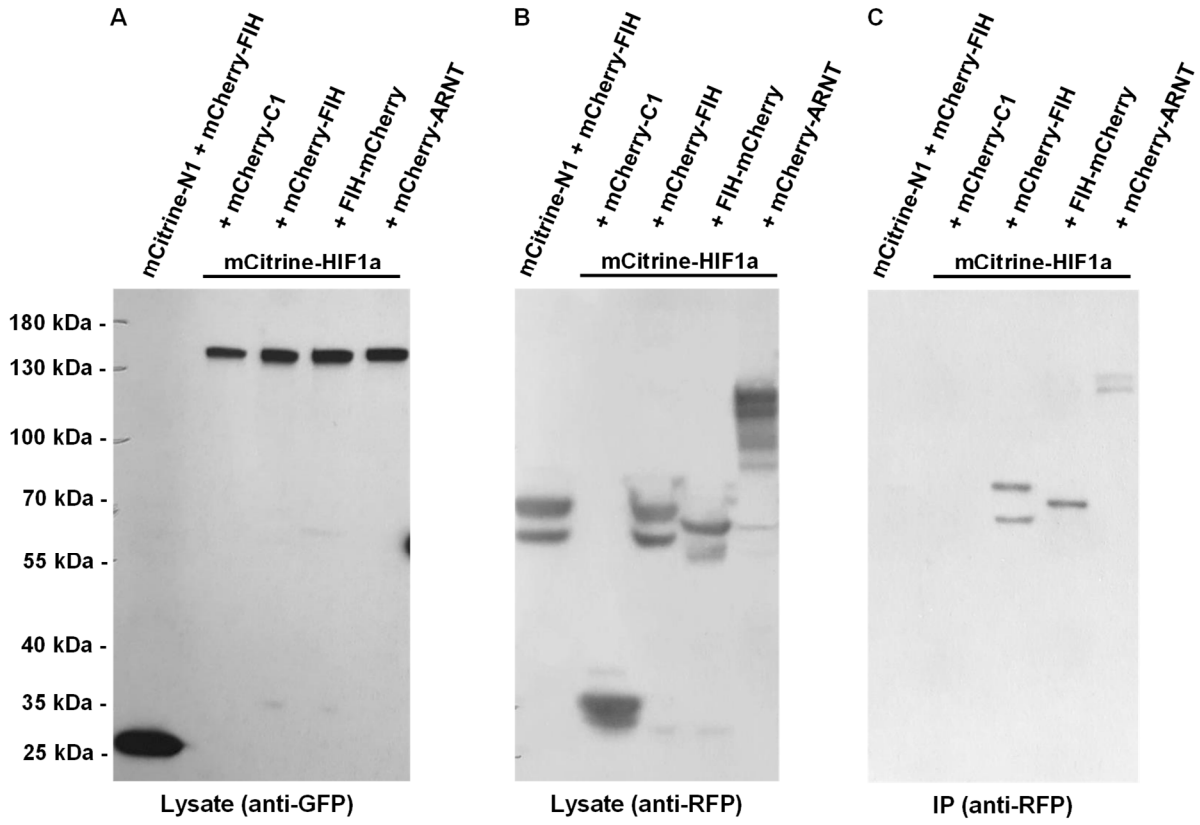

Figure 6-26: Co-IP proved the interaction of fluorophore-tagged HIF-1α and FIH in HEK293T cell lysates. Three different immunoblots for two different antibodies (anti-RFP and anti-GFP) and Co-IP samples (precipitate of the IP and whole cell lysate) are shown. A: Detection of mCherry in the protein lysates validates the successful transfection of the HEK293T cells with the mCherry constructs. B: Detection of mCitrine by a GFP-antibody in the protein lysates shows the overexpression of the mCitrine constructs in the transfected HEK293T cells. C: Detection of mCherry by an RFP-antibody in the precipitate of the microbead prey. mCitrine-HIF-1α and FIH-mCherry transfected cell lysates were supposed to prove the interaction of tagged HIF-1α and FIH in vitro. The negative controls mCitrine-HIF-1α + mCherry-C1 and mCitrine-N1 + mCherry-FIH showed empty lanes, while the bands in the IP lane of mCitrine-HIF-1α + mCherry-ARNT transfected cells acted as proof of concept.

6.8 Protein-protein interaction of HIF and FIH via seFRET

HEK293T and U2OS cells were transfected with plasmids containing the sequence for different fluorophores, e.g. mTurquoise2, mCitrine, mKO2 and mCherry. The proteins of interest, which were HIF-1α, ARNT and FIH, were tagged with these fluorophores and the cells were transfected successfully with the constructs (see Figure 6-27). As the transfection efficiency and reliability were higher in HEK293T than in U2OS cells, more FRET measurements were realized with the HEK293T cell line.

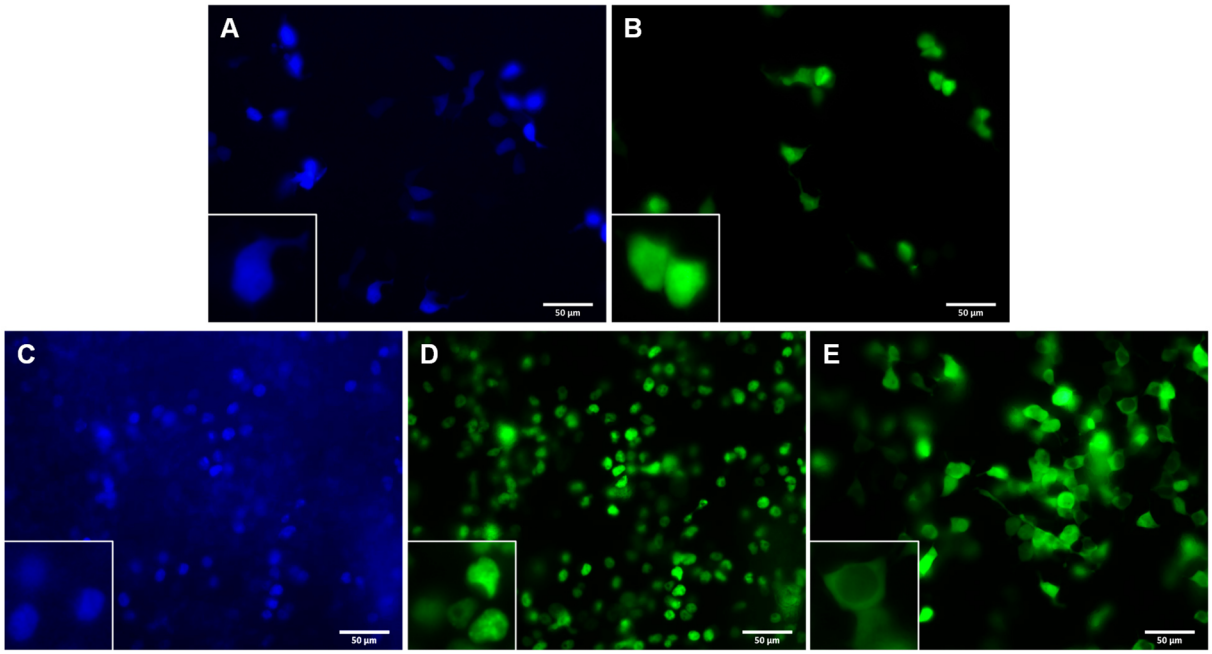

Figure 6-27: Exemplary microscopic pictures from transfected HEK293T cells. Cells were transfected with a construct for soluble mTurquoise2 (A), soluble mCitrine (B), mTurquoise2-HIF-1α (C), mCitrine-ARNT (D) and mCitrine-FIH (E). HIF-1α and ARNT translocated into the nucleus, while FIH is mostly found in the cytosol. Soluble fluorophores were distributed throughout the whole cell. Scale bar = 50 µm.

As a positive control for the seFRET setup, the interaction between CFP-HIF-2α and YFP-ARNT was measured. This FRET pair was tested before and had given a reliable positive signal (Hu *et al.*, 2016). The achieved FRET efficiency of this pair in U2OS cells was 0.35 (see Figure 6-28). The negative control (soluble CFP + YFP) showed no signal at all.

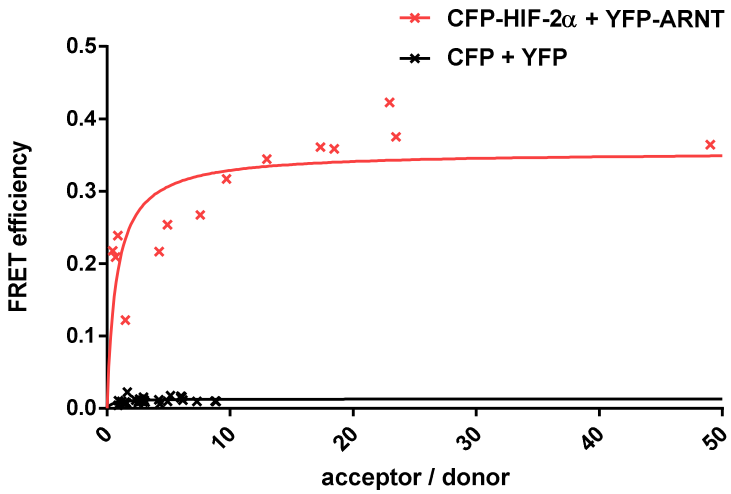

Figure 6-28: seFRET measurement of CFP-HIF-2α and YFP-ARNT constructs. U2OS cells were transfected with CFP or CFP-HIF-2α and YFP or YFP-ARNT plasmids (efficiency of HIF-2α and ARNT = 0.35, n = 14). Transfection with soluble CFP and YFP served as negative control (efficiency = 0.01, n = 27). Ratio of acceptor to the donor is plotted against the calculated FRET efficiency. The saturation curve was calculated with a non-linear fit (Michaelis-Menten: $Y = V_{max} * X / (K_m + X)$).

seFRET measurements for HIF-1α + ARNT and HIF-1α + FIH were carried out with the optimized fluorophores: mTurquoise2 as donor and mCitrine as acceptor fluorophore. For the negative control, cells were transfected with mTurquoise2-HIF-1α or -ARNT + soluble mCitrine (see Figure 6-29) and measured the same day with the same setup as the samples for interaction studies. The calculated FRET efficiency was quite high for negative controls: 0.04 - 0.19. The evaluation of the interaction measurements between HIF-1α and FIH constructs is therefore difficult. Samples with mTurquoise2-HIF-1α + mCitrine-ARNT as well as the other way round (mTurquoise2-ARNT + mCitrine-HIF-1α) showed no FRET efficiency higher than the corresponding negative control (see Figure 6-29 A and B). The same result was observed for mTurquoise2-HIF-1α and mCitrine-FIH: FRET efficiency was positive as viewed in absolute terms, but lower than the corresponding negative control (see Figure 6-29 C).

The donor/acceptor ratio substantially differed between samples with HIF-1α or ARNT fused to the donor molecule. As HIF-1α is degraded under normoxia, the amount of stable mTurquoise2-HIF-1α is much lower than of mTurquoise2-ARNT and mCitrine-HIF-1α is lower than mCitrine-ARNT. Therefore, the donor/acceptor ratio for mTurquoise2-HIF-1α/mCitrine-ARNT was very high in some cells (>100) while mTurquoise2-ARNT/mCitrine-HIF-1α never reached a ratio higher than 4 (see Figure 6-29 A and B). Like ARNT, FIH is a stable protein under normoxia which is why the donor/acceptor ratio for mTurquoise2-HIF-1α/mCitrine-FIH showed values up to 1000.

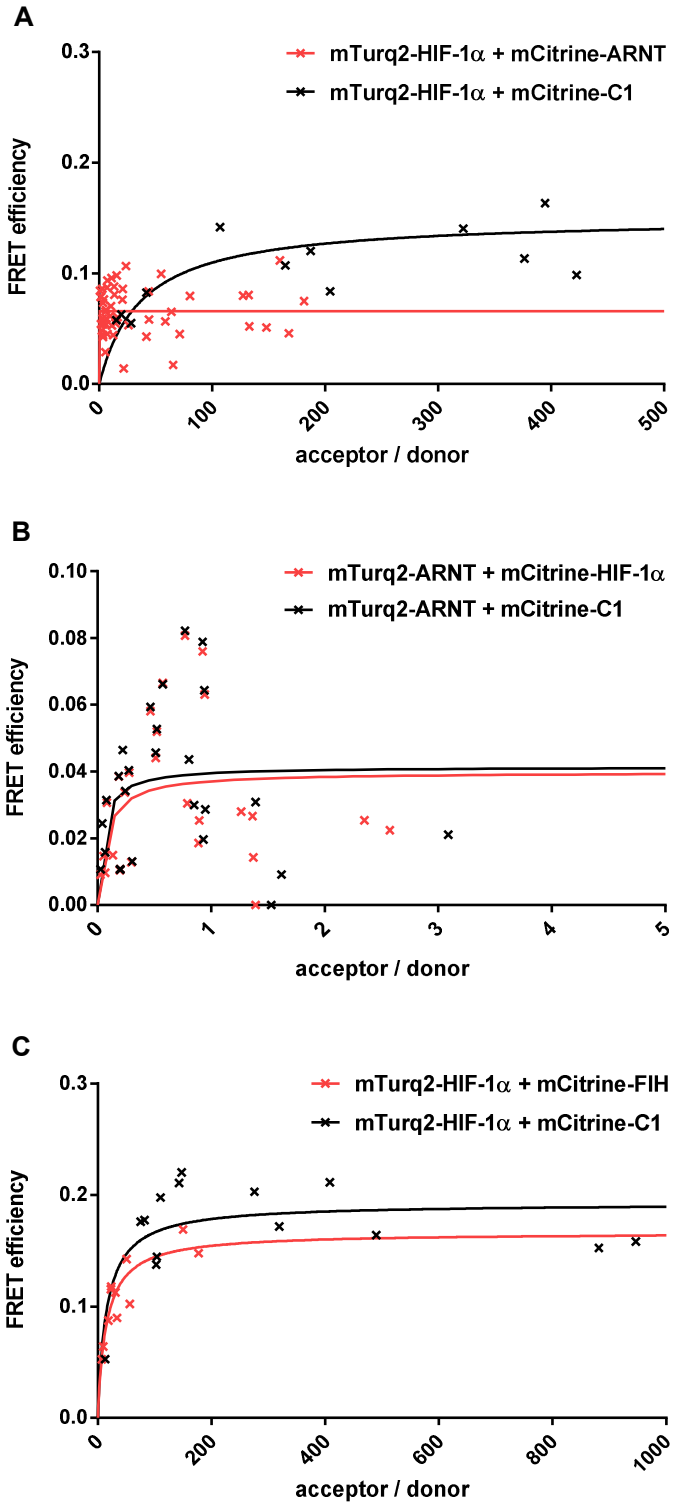

Figure 6-29: Interaction measurements with seFRET for HIF-1α with ARNT and FIH. A: HEK293T cells were transfected with mTurq2-HIF-1α and mCitrine-ARNT constructs (FRET efficiency = 0.07, n = 58, red). Combination of Turq2-HIF-1α and soluble mCitrine-C1 was used as negative control (efficiency = 0.15, n = 23, black). B: U2OS cells were transfected with mTurq2-ARNT and mCitrine-HIF-1α (FRET efficiency = 0.04, n = 27, red). The plasmids mTurq2-ARNT and soluble mCitrine-C1 served as negative control (efficiency = 0.04, n = 26, black). C: HEK293T cells were transfected with mTurq2-HIF-1α and mCitrine-FIH for interaction studies of HIF-1α and FIH (FRET efficiency = 0.17, n = 11, red). As a negative control, cells were transfected with mTurq2-HIF-1α and mCitrine-C1 (efficiency = 0.19, n = 17, black). All saturation curves: non-linear regression (Michaelis-Menten: $Y = V_{max} * X / (K_m + X)$).

As the measurements with the FRET pair mTurquoise2 and mCitrine did not validate the *in vivo* interaction between HIF-1α and FIH, it was needed to optimize the setup. One option was to change the fluorophores as the steric hindrance for the potential interactions of the tagged protein can be dependent on the fluorophore. As a new acceptor, FIH was tagged with mKO2. This time, the negative control (mTurquoise2-HIF-1α + mKO2) showed a FRET efficiency of 0.00. In cells transfected with mTurquoise2-HIF-1α and mKO2-ARNT, a FRET efficiency of 0.07 was calculated, clearly positive in comparison to the negative control (see Figure 6-30). The analysis of the mTurquoise2-HIF-1α + mKO2-FIH sample showed diverse results. Several cells showed a FRET efficiency clearly above the negative control, but some cells had a calculated efficiency of nearly 0, leading to a calculated efficiency of 0.01 (see Figure 6-30).

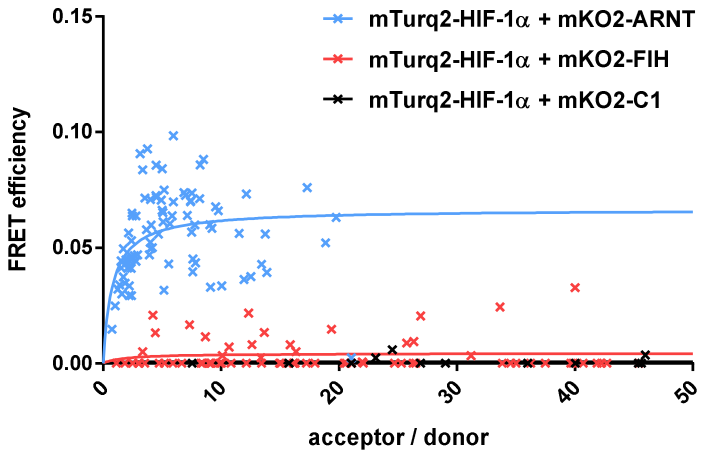

Figure 6-30: Measurements of seFRET between mTurq2-HIF-1α and mKO2-ARNT or mKO2-FIH. HEK293T cells were transfected with mTurq2-HIF-1α and soluble mKO2-C1 as a negative control (FRET efficiency = 0.00, n = 17, black) as well as mTurq2-HIF-1α and mKO2-ARNT as a positive control (efficiency = 0.07, n = 87, blue). Interaction of HIF-1α with FIH was studied with the constructs mTurq2-HIF-1α and mKO2-FIH (efficiency = 0.01, n = 82, red). Saturation curves: non-linear regression (Michaelis-Menten: $Y = V_{max} * X / (K_m + X)$).

6.9 Protein-protein interaction of HIF and FIH via FLIM

FLIM is an alternative method to measure protein-protein interaction via FRET. HEK293T cells were transfected with mCitrine-HIF-1α and mCherry-FIH or -ARNT constructs as well as with negative (mCitrine-HIF-1α + mCherry-N1) and positive (linked mCherry-mCitrine) controls. The measurement of the donor fluorescence lifetime in the negative control compared to the samples (as positive FRET decreases the fluorescence lifetime of the donor molecule) then results in the interacting fraction α. An α of 0 means that no donor molecule is

in close proximity to any acceptor; α = 1 would mean that every donor has a positive FRET with an acceptor. Negative arithmetic means of α-values from one cell can occur as artifacts from the mean calculations.

The positive control shows the highest possible α-value in this setup, which is not 1 due to e.g. rotation of the fluorophores. Therefore, the linker's interacting fraction here is 0.60 (see Figure 6-31). Cells transfected with mCitrine-HIF-1α + mCherry-ARNT reached an α-value of 0.09, which is still significantly higher than the negative control with a mean value of -0.10. The measurement of mCitrine-HIF-1α + FIH-mCherry resulted in an α-value of 0.03. Compared to the negative control, this sample was clearly positive ($p < 0.0001$), although the absolute value was low.

As it is visible in the merged image of the sample, mCitrine-HIF-1α and FIH-mCherry seem to be localized in different compartments. The overexpressed HIF-1α accumulated in the nucleus while FIH is predominantly localized in the cytoplasm. For this reason, it should be checked if the analysis for the mCitrine-HIF-1α + FIH-mCherry images could be repeated with ROIs particularly imbedding the nuclei or only cytoplasmatic regions, respectively. As the clear differentiation of nucleus and plasma was not possible in all intensity maps of this experiment, this specific analysis was not possible.

Certain enzyme inhibitors are supposed to prolong the time of interaction between the enzyme and its substrate as the substrate cannot be modified by the enzyme. The successful reaction leads to the release of the substrate. In interaction studies like FRET measurements, the application of an inhibitor could increase the signal for the interaction due to the prolonged contact. Here, DMOG was used as an inhibitor of FIH in a FLIM measurement of FIH and HIF-1α interaction.

The negative control in this measurement led to an α-value of 0.09 (see Figure 6-32). This divergence from the former results revealed the importance of the controls in each experiment. Besides, the positive control, in which the linked fluorophore construct was inserted into the cells, showed a higher value than before (α = 0.67). Transfection of mCitrine-HIF-1α + mCherry-ARNT resulted in a significant increase of the α-value compared to the negative control, which proved the known interaction of HIF-1α and ARNT in living HEK293T cells (α = 0.24), again. The lifetime of mCitrine was decreased in mCitrine-HIF-1α and FIH-mCherry transfected cells resulting in a significantly increased α-value (α = 0.17). DMOG treatment even enhanced the signal for the interaction of HIF-1α and FIH to an α-value of 0.38 and also the signal for HIF-1α and ARNT to 0.31. These enhancements of the signals were significant and showed the usefulness of DMOG-treatment in *in vitro* measurements.

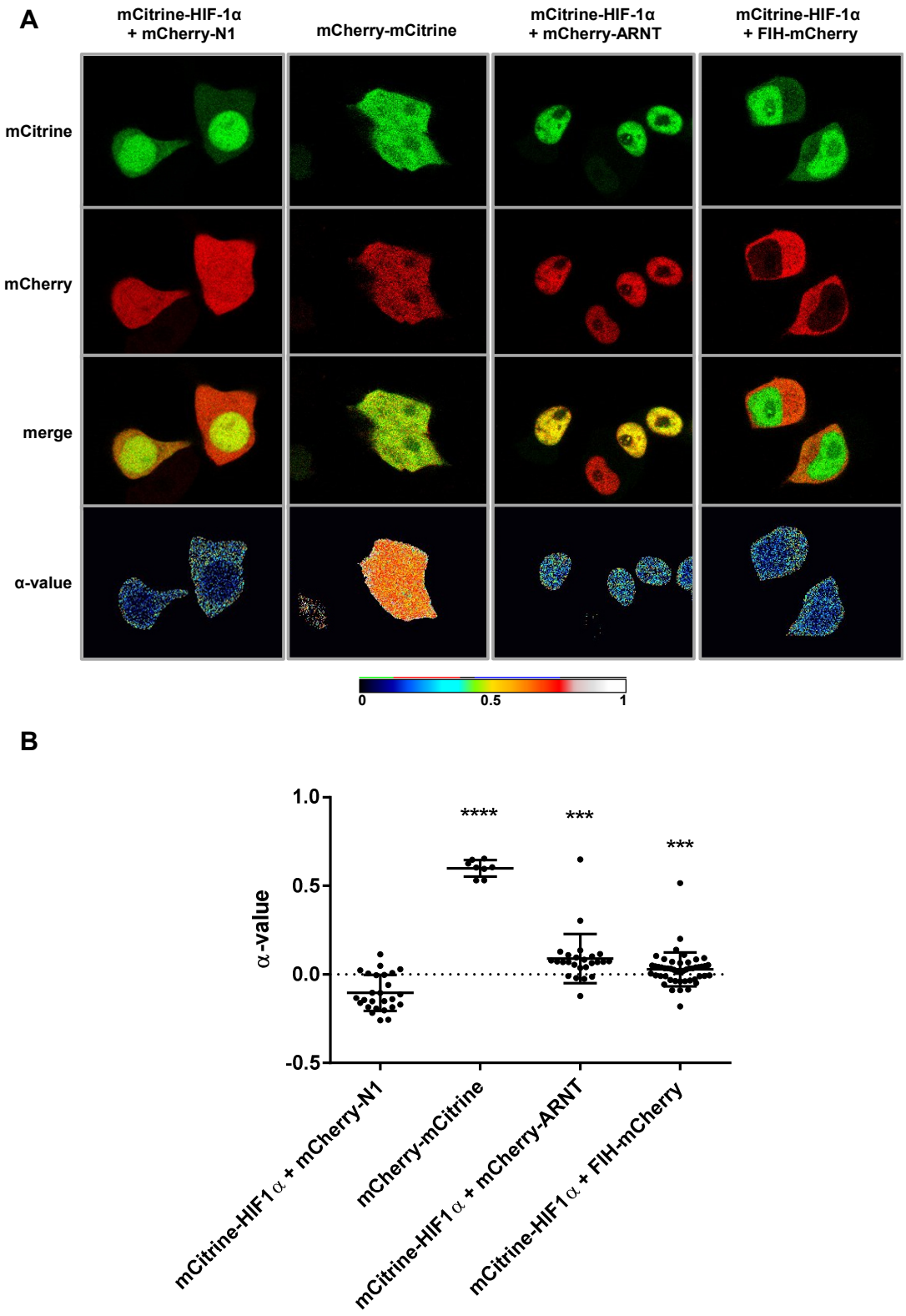

Figure 6-31: FLIM measurements of fluorophore-tagged HIF-1α and ARNT / FIH in HEK293T cells. A: Exemplary false color pictures of transfected cells in the channels for mCitrine and mCherry, a merged picture and the α-values with a color bar from 0 to 1. The first lane shows cells transfected with mCitrine-HIF-1α and mCherry-N1 as negative control, the second lane represents the positive control with linked donor and acceptor fluorophore. The third and fourth lane show pictures of the constructs of interest mCitrine-HIF-1α and mCherry-ARNT/-FIH. B: Mean α-values for single cells from two independent experiments. Indicated significances refer to the negative control (n = 26/8/25/49).

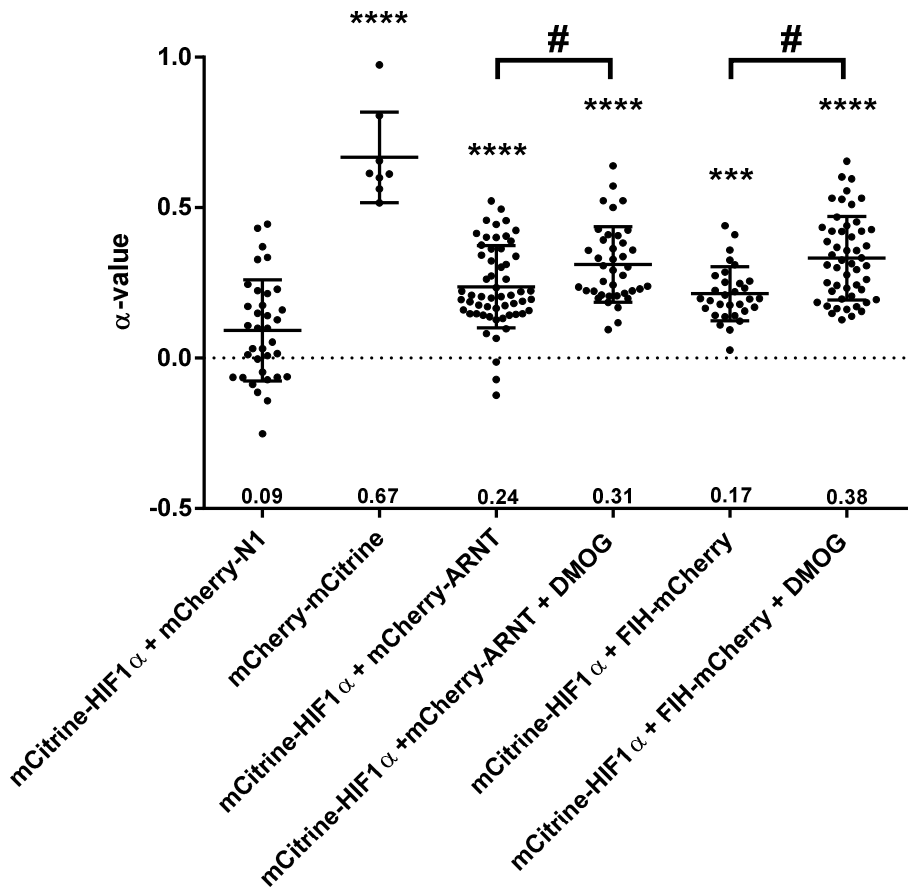

Figure 6-32: FLIM measurements of HIF-1α and ARNT or FIH under the treatment of the hydroxylase inhibitor DMOG and without. Mean α-values for single cells from two independent experiments ± SD, n = 35/8/57/39/31/51, indicated significances with * refer to the negative control, #: p < 0.01.

7 Discussion

7.1 Colon epithelial FIH knockout has no effect on tumor development in the AOM-DSS colon cancer mouse model

To study the role of HIF and its regulator FIH on cancer development in the colitis-associated CRC mouse model, an efficient FIH knockout in colon epithelial cells from $FIH^{fl/fl}$xVillinCre mice had to be proven.

Isolated epithelial cells from $FIH^{fl/fl}$xVillinCre as well as samples from the whole colon showed an efficient FIH knockout. In these mice, FIH mRNA expression was ~70% reduced in comparison to $FIH^{fl/fl}$ littermates (see Figure 6-1). This reduction of the asparagine hydroxylase FIH led to an increase of HIF activity in the colon epithelium: The expression of HIF C-TAD-dependent target genes like *Phd3*, *Vegf* and *Bnip3l* was substantially enhanced (see Figure 6-2 and Figure 6-3). The heterozygously expressed Cre recombinase was therefore sufficient to induce a colon epithelial FIH knockout with a measurable effect on HIF target genes, even in whole colon samples.

$FIH^{fl/fl}$xVillinCre mice and their wildtype littermates were used for the AOM-DSS CRC mouse model. With the help of this well-established model for colorectal tumor development after induction of a chronic colitis by DSS treatment it is possible to study chemical or genetic effects on the progress of the disease and tumor growth.

Mice were treated with AOM and DSS and were sacrificed two weeks after the last DSS administration. During the experiment, the disease progress was monitored by recording the body weight, stool consistency and occurrence of blood in the feces. The body weight loss was quite smooth with less than 10%, compared to acute colitis models with DSS concentrations of 2.5 to 5%, where mice with a similar genetic background loose more than 10% of their body weight (Backer *et al.*, 2017, Vowinkel *et al.*, 2004). All disease factors together resulted in a disease activity index between 2 and 8 during DSS treatments, which was not different between $FIH^{fl/fl}$ and $FIH^{fl/fl}$xVillinCre mice (see Figure 6-4). Consequentially, there was no difference in tumor development quantified by tumor number or colon weight between $FIH^{fl/fl}$xVillinCre animals and their wildtype littermates (see Figure 6-5). But it was possible to clearly distinguish between DSS-treated mice and control animals. In control mice, only small nodes occurred in the colon which could be seen as the baseline of the manual counting. In contrast, DSS-treated animals had about 20 single tumors in their colon. This additional tumor tissue significantly increased the colon weight from a mean of ~180 mg in control animals to ~270 mg in DSS-treated animals. The H&E staining and photographs of colons of AOM-DSS-treated animals showed tumor growth and structures similar to those from the literature (Tanaka *et al.*, 2003, Parang *et al.*, 2016, Thaker *et al.*, 2012, Greten *et*

al., 2004), although the number of AOM injections, the DSS concentration and the length and number of DSS cycles vary between these studies.

Previous work by (Chen *et al.*, 2015a) showed that FIH inhibits tumor cell proliferation, migration, invasion and colony formation in CRC cells *in vitro*. They observed decreased levels of the HIF target genes *Glut1* and *Vegf* due to an increase of FIH. Here, *Vegf* expression levels were increased in colon RNA samples from $FIH^{fl/fl}$xVillinCre animals due to the FIH knockout (see Figure 6-2 and Figure 6-3) but with no effect on tumor growth.

Because of the missing effect on tumor growth by the FIH knockout, $FIH^{fl/fl}$ and $FIH^{fl/fl}$xVillinCre normal colon tissue and tumor tissue from experimental mice were checked for FIH expression. Immunohistochemical staining of the FIH protein showed a faint cytoplasmic signal in normal colon tissue cells, but a strong nuclear staining in many tumor cells (see Figure 6-7). Tumor microenvironment is supposed to have low oxygen levels and therefore stabilizes the HIF-1α subunit. Moreover, it is known that FIH translocates into the nucleus together with its substrate HIF-1α under hypoxia (Wang *et al.*, 2018). Both effect are possibly the reason for the detectable FIH in the nuclei of colon tumor cells in the AOM-DSS mouse model. As the FIH protein was detectable in tumors of $FIH^{fl/fl}$ and in $FIH^{fl/fl}$xVillinCre mice, colon tumor cells cannot completely be derived from epithelial colon cells. These FIH positive cells could be immune cells that infiltrated the tumor microenvironment, e.g. tumor-associated macrophages (TAMs) which build the largest group of the myeloid infiltrate (Vitale *et al.*, 2019). Altered gene expression of epithelial cells during the process of cancer development is another possible explanation for the presence of FIH in the tumors of $FIH^{fl/fl}$xVillinCre mice, as the FIH knockout is dependent on the usage of the Villin promoter. Possibly, tumor cells reduce the transcription of villin protein and therefore also of the Cre recombinase. Kitahara *et al.* (2001) showed in cDNA microarrays that gene expression is changed during colorectal carcinogenesis between normal epithelium and tumor tissue. Nevertheless, the data herein for knockout efficiency in the qPCR and RNAseq data showed a strong decrease in the *Fih* expression (see Figure 6-2 and Figure 6-3).

As there were no noticeable differences between wildtype and FIH knockout mice regarding CRC development in the AOM-DSS model, the hydroxylase inhibitor DMOG was added to the model to increase the effect of the FIH knockout in the colon epithelium. DMOG stabilizes HIF-α as the PHDs are inhibited and the proteasomal degradation is repressed.

7.2 Colon epithelial knockout of FIH attenuates the disease progress in the AOM-DSS-DMOG colon cancer mouse model

In the AOM-DSS-DMOG model, mice were exactly treated as in the AOM-DSS model, but with an additional, repetitive DMOG administration during the DSS phases. DMOG inhibits

hydroxylases like the PHDs and FIH and therefore enhances the amount of HIF during the administration periods. While the activity of DMOG decays, the effect of the FIH knockout is supposed to be strengthened as its substrate HIF-α is available in great quantities. This effect of an increased amount of HIF due to DMOG-treatment was shown in several studies (Lando *et al.*, 2002b, Jaakkola *et al.*, 2001) and was here proven in cell culture experiments with HBLAK cells that were incubated with 1 mM DMOG for 4 hrs (see Figure 6-8).

$FIH^{fl/fl}$ and $FIH^{fl/fl}$xVillinCre mice were treated with AOM-DSS and DMOG. Again, the disease progress was monitored by the DAI and the bodyweight loss (see Figure 6-9). In the third period of DSS administration, $FIH^{fl/fl}$ mice showed a significantly higher DAI than $FIH^{fl/fl}$xVillinCre mice on day 50 of the experiment. Additionally, the total DAI of the third DSS phase was significantly reduced in the FIH knockout animals compared to their wildtype littermates. Thus, loss of epithelial FIH in the colon led to a reduced disease progress during the third DSS administration under DMOG treatment. Compared to the results of the AOM-DSS model, AOM-DSS-DMOG-treated wildtype mice showed no altered disease progress contrary to the results of Cummins *et al.* (2008), who observed a protective role of DMOG in a mouse model of DSS-induced acute colitis.

Although the colitis was less severe in $FIH^{fl/fl}$xVillinCre mice, there was no difference in the CRC development. Tumor number and colon weight were not altered between $FIH^{fl/fl}$xVillinCre and $FIH^{fl/fl}$ animals (see Figure 6-10). Thus, the decrease of colitis severity did not lead to a reduced tumor growth, at leat not until termination of the experiment. Effects of the reduced disease progress on either the starting point of carcinogenesis or on the further tumor growth after day 68 of the experiment could not be studied in this mouse model.

7.3 FIH knockout in the colon epithelium decreases the inflammatory response in a chronic colitis

The inflammatory response that is part of the colitis progress was investigated. First, we investigated the immune cells of the spleen as the spleen weight tended to be increased in $FIH^{fl/fl}$ mice in both CRC models (see Figure 6-12). But there were no changes in the number of monocytes ($Cd11b^{+}$) or dendritic cells ($CD11c^{+}$) in the spleens of $FIH^{fl/fl}$ DSS-treated and $FIH^{fl/fl}$xVillinCre DSS-treated mice in flow cytometry experiments (see Figure 6-13 and Figure 6-14). Alone, a tendency of an increased amount of activated immune cells ($CD86^{+}$) was observed in comparison to the untreated control mice. As the flow cytometry results from different experiments could not be bundled due to experiment specific compensations and staining efficiency, the results needed to be treated with caution due to the low number of

samples, which is why only tendencies could be determined. Still, no differences between FIH$^{fl/fl}$xVillinCre and FIH$^{fl/fl}$ were seen, independent from DMOG treatment.

When having a direct look into the colon by mRNA and immunohistochemical analysis, the infiltration of immune cells into DSS-treated tissue was clearly visible: F4/80 positive macrophages were found in a much higher amount in DSS-treated animals than in controls (see Figure 6-15 A, Figure 6-16 and Figure 6-17). This result corresponds to former work on acute colitis where F4/80 positive immune cells infiltrated into the inflamed colon (Backer *et al.*, 2017, Nunes *et al.*, 2018, Ohkawara *et al.*, 2008). Even at the end of the two weeks of regeneration after the last DSS treatment in our AOM-DSS model, the remains of macrophage invasion into the colon were still visible.

In qPCR analyses, there was a tendency to a diminished AOM-DSS-dependent induction of *f4/80* expression in FIH$^{fl/fl}$xVillinCre mice in comparison to FIH$^{fl/fl}$ mice (see Figure 6-15). In the immunohistochemical staining, this difference between the genotypes was much stronger. In all DSS-treated animals, normal colon tissue with intact crypts was slightly infiltrated by macrophages. In colons of FIH$^{fl/fl}$ mice, more F4/80-positive cells were found than in FIH$^{fl/fl}$xVillinCre mice. In addition to the higher amount of macrophages in wildtype animals, they infiltrated deeper into the tissue affecting the *Tela submucosa* more than in FIH knockout mice. In the tumor tissue, the difference between FIH knockout animals and wildtype ones is clearly visible: tumors of FIH$^{fl/fl}$ animals were full of F4/80-positive cells while the amount of these cells was substantially reduced in FIH$^{fl/fl}$xVillinCre mice (see Figure 6-17). This result was observed in AOM-DSS-treated as well as in AOM-DSS-DMOG-treated animals (see Figure 6-18). These F4/80 positive macrophages might not have infiltrated into the colon tissue solely due to the colitis but were also recruited by chemokines from the tumor site (Yahaya *et al.*, 2019).

This phenomenon of a discrepancy between qPCR and immunohistochemistry may be due to the high amount of normal colon tissue that was used for RNA isolation. In immunohistochemical studies, it is possible to look for specific tissue regions which is not possible with our protocol for RNA isolation.

Other immune response genes despite *F4/80* confirmed the generally lower immune response in FIH$^{fl/fl}$xVillinCre mice. Analysis of RNAseq data from DSS-treated animals showed several genes that were downregulated in the FIH$^{fl/fl}$xVillinCre mice in comparison to the wildtype animals (see Figure 6-19). The amount of regulatory (*Cd4* and *Foxp3*) and cytotoxic T cells (*Cd8a*) as well as of macrophages identified by *Inos* and *Arg1* was reduced in the FIH knockout mice. The sum of the reduced expression of several immune cell genes was reflected in so-called GO terms derived from the RNAseq data (see Table 6-1 and Table 6-2). In colon tissues induction of GO terms belonging to the general immune response of human IBD patients was shown by Cheng *et al.* (2019). In our study, GO terms like ‘immune

response', 'acute inflammatory response' or 'T cell activation' were overrepresented in the set of downregulated genes in FIH$^{fl/fl}$xVillinCre compared to FIH$^{fl/fl}$ mice. This result was independent from the mouse model: In AOM-DSS- and in AOM-DSS-DMOG-treated mice the outcome of the RNAseq analysis was similar, like it was seen for immunohistochemical F4/80 staining. Thus, these results on the molecular level seem to be much more sensitive than the macroscopic analyses by bodyweight and DAI. For the macroscopic differences, DMOG-treatment was needed to reveal the effect of the knockout. Besides the immune response genes, differences in transcription factor activities with different downstream target functions were identified by RNAseq analysis (Ingenuity Pathway Analysis, IPA, see Figure 6-20). Some of these transcription factors belong to the group of immune response regulating factors as the IRFs and STAT1. STAT1 is already known to be repressed by HIF-1 (Ivanov *et al.*, 2007), which fits to our observation of a decreased STAT1 activity in FIH$^{fl/fl}$xVillinCre mice compared to wildtype animals. STAT1 was already protein of interest in studies for inflammation-associated colorectal carcinogenesis: Leon-Cabrera *et al.* (2018) showed that STAT1 deficiency promotes intestinal damage and proliferation in early-stage tumors and diminishes apoptosis in advanced tumors which is accompanied with a dysregulation of immune cell recruitment. But like in our study, tumor number was not changed due to the decreased STAT1 activity (Leon-Cabrera *et al.*, 2018).

Other transcription factors with decreased downstream target functions have a tumor suppressing function. The negative z-score for the p53 protein is especially interesting and surprising as it is known that p53 levels increased with FIH inhibition (Wang *et al.*, 2019). Thus, the FIH knockout was expected to lead to a positive z-score and therefore to an upregulation of the expression of the p53 downstream genes. A possible explanation could once again be that the whole colon was considered for RNA analysis including many other cells than the FIH lacking epithelial cells. Alternatively, the reduced p53 activity could be caused by the AOM and DSS treatment. Previously it was shown that p53 is reduced in mice treated with AOM, DSS or AOM-DSS (Zheng *et al.*, 2016). Increased levels of SOX4 were shown to be associated with CRC progression (Wang *et al.*, 2016). Reduced SOX4 activity like in the FIH$^{fl/fl}$xVillinCre mice is therefore supposed to suppress CRC cell proliferation, but this effect could not be seen by tumor counting or colon weighting (see Figure 6-5). Similarly, to SOX4, the transcription factor E2F3 was found upregulated in CRC tissue samples from human patients (Chang *et al.*, 2015). E2F3 regulates genes that determine the G1/S transition in the cell cycle leading to proliferation defects in E2F3$^{-/-}$ MEFs (Humbert *et al.*, 2000). The reduced transcriptional activity of E2F3 in our mice lacking epithelial FIH did not lead to substantial differences in tumor growth at the time point the experiment was terminated. TRIM24 is assumed to act as an oncogene in CRC as its knockdown leads to a reduced cell growth in human colorectal cancer cells (HCT116) (Wang *et al.*, 2014). The

increased activity of TRIM24 in AOM-DSS-treated FIH$^{fl/fl}$xVillinCre mice compared to FIH$^{fl/fl}$ mice (see Figure 6-20) could counteract the tumor suppressing effects of SOX4 and E2F3 downregulation. Effects of all these proliferation regulating transcription factors may need a detailed analysis at early-stage tumor development, which was not the aim of this study but is of great interest for future experiments.

The question arising from these results is what the mechanisms are behind the differences between FIH$^{fl/fl}$ and FIH$^{fl/fl}$xVillinCre mice. Tumor tissue of colons of FIH$^{fl/fl}$ and of FIH$^{fl/fl}$xVillinCre mice showed the same amount of FIH-positive cells (see Figure 6-7). Thus, the effect of the epithelial FIH knockout on the HIF activity in the tumor cells is probably quite low. This was confirmed by HIF protein staining in the same tissues (see Figure 6-23). No differences on HIF-1 stabilization between the genotypes were detected. Overall, the protein amount of HIF-1 was low in most parts of the colon tumors. Alone the tumor edges showed HIF-1-positive cells. This could be due to the lower oxygen level in these tumor areas as it can be assumed by looking at the Hypoxyprobe™ staining (see Figure 6-21 and Figure 6-22). The overall low amount of HIF-1α found in the colon slices could also be caused by the preparation procedure. The cleaned and opened colons were exposed to the room air with 21% oxygen while tumors were counted and samples were taken. This time period could be enough to allow degradation of the HIF-1α protein that was stabilized in hypoxic inflammation and cancer.

On mRNA level, no effects of the epithelial FIH knockout on *Hif1a* expression were detectable by *in situ* hybridization, either. The staining proved the ubiquitous expression of *Hif1a* (Ema *et al.*, 1997) in colon tumors, but without showing any differences between FIH$^{fl/fl}$ and FIH$^{fl/fl}$xVillinCre animals or the treatment (see Figure 6-25).

Similar results were gained by the detection of the HIF-2α protein and mRNA. HIF-2α protein expression did not show changes between FIH$^{fl/fl}$ and FIH$^{fl/fl}$xVillinCre mice (see Figure 6-24). As for HIF-1α, positively stained cells were detected only at the tumor edges. In the RNAscope® samples, *Hif2a* mRNA was spotted throughout the complete tumors, but only in a certain cell type (see Figure 6-25). The staining pattern suggests an endothelial specific *Hif2a* expression as it was described in the literature (Tian *et al.*, 1997).

Significant differences in HIF stabilization or expression due to the FIH knockout could have been a cause for the changes in the immune response between FIH$^{fl/fl}$ and FIH$^{fl/fl}$xVillinCre mice. Relations between HIF activity and the colitis progress are already known. For instance, it was found that neutrophil recruitment in a colitis-associated CRC mouse model was directly dependent on an increased HIF-2 activity (Triner *et al.*, 2017). Karhausen *et al.* (2004) reported that a number of barrier-protective genes was induced by HIF-1 as an innate protective mechanism for mucosal integrity. Here, there were no differences in the expression of these genes found in the RNAseq data of both AOM-DSS- and AOM-DSS-

DMOG-treated FIH$^{fl/fl}$ and FIH$^{fl/fl}$xVillinCre mice (see RNAseq data, tables of gene expression).

The colon epithelial FIH knockout had decreased the inflammatory response and colitis progress under DMOG treatment in a mouse model for colitis-associated CRC. Still, there was no effect on tumor growth after the chronic colitis although it was expected that a milder disease progress would lead to a less severe cancer development. Possibly, the activation of HIF target genes negates the positive effects of a milder inflammation by promoting tumor development. A stronger stabilization of HIF-1α or HIF-2α was not found in immunohistochemical staining of colon tissue from AOM-DSS(-DMOG)-treated mice, but the induction of HIF target genes (*Phd3*, *Vegf*) was measurable via qPCR. Additionally, other FIH substrates might play a role for cancer development and neither these substrates nor their possible role have been determined by now. Further detailed studies will be necessary to work out the complete mechanism that lies behind these observations that are summarized in Figure 7-1.

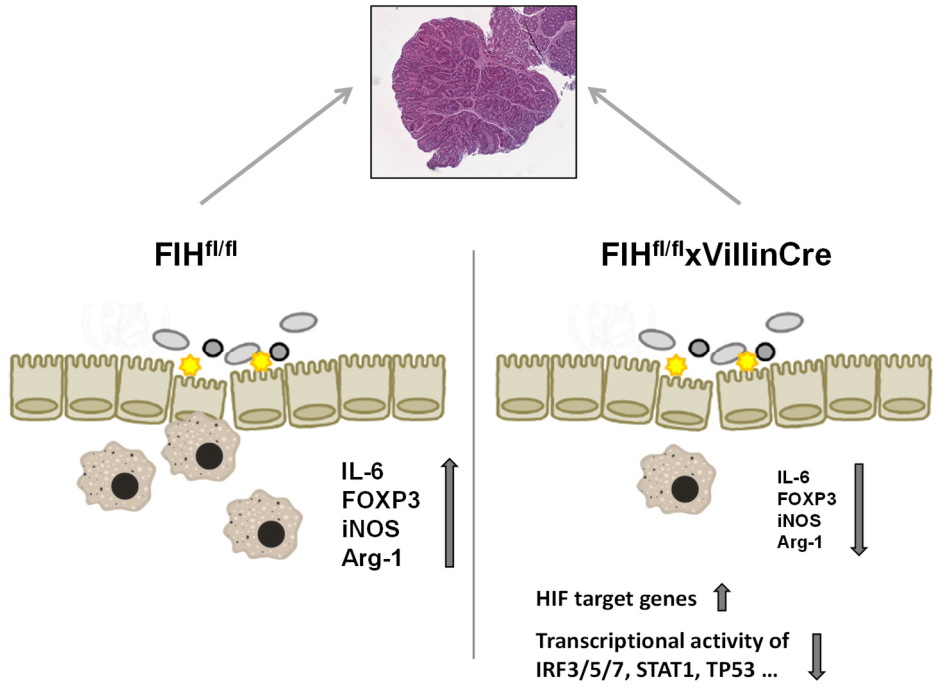

Figure 7-1: Graphical summary of the results from the experimental mouse models for CRC development. FIH$^{fl/fl}$xVillinCre mice showed reduced macrophage infiltration as well as lower immune response gene expression resulting in a less severe colitis progress after AOM-DSS-DMOG-treatment. But, the emerging tumors did not differ in amount, size or structure between the genotypes.

7.4 The interaction of HIF-1α and FIH

Interaction studies for HIF-1α and FIH were carried out by seFRET and FLIM measurements in living cells as well as by Co-IP. Co-IPs have already been used to prove the interaction between HIF-1α and its regulator FIH (Mahon *et al.*, 2001). Here, we used the Co-IP method to validate that our tagged HIF-1α and FIH proteins were able to interact with each other despite the attached fluorophores.

Western Blot analysis of the Co-IP revealed an unexpected result with the mCherry-FIH construct. Upon Co-IP of mCherry-FIH with mCitrine-HIF-1α, two bands were detected by the RFP antibody (see Figure 6-26). This indicated that mCherry was fused to either of both FIH fusion proteins that were at least partially correct since it interacted with mCitrine-HIF-1α. Strikingly, FIH-mCherry exhibited the calculated size of 70 kDa, while mCherry-FIH expression resulted in the two variants of ~65 and ~80 kDa. The Co-IP revealed the *in vitro* interaction between HIF-1α and FIH, but with the expression of a protein which is still unknown but encoded by the mCherry-FIH construct.

seFRET measurements were validated by a positive control (HIF-2α + ARNT), as FRET between HIF-α and ARNT was previously reported (Konietzny *et al.*, 2009, Wotzlaw *et al.*, 2007, Hu *et al.*, 2016). Here, the measurement with CFP-HIF-2α and YFP-ARNT revealed the correct usage of the setup (see Figure 6-28) with a calculated FRET efficiency of 0.35. State-of-the-art fluorophores with advantages like enhanced photostability, superior brightness, low autofluorescence and well-defined spectral characteristics (Day *et al.*, 2009) were implemented in order to optimize the dynamic range and reliability of seFRET measurements. mTurquoise2, mKO2 and mCitrine match the used filter sets and lasers better than CFP and YFP. Furthermore, HIF-1α was used instead of HIF-2α since the aim of the FRET studies is to show the interaction of HIF-α with FIH and FIH interacts more efficiently with HIF-1α than HIF-2α (Koivunen *et al.*, 2004). As a negative control, the tagged donor construct in combination with the soluble acceptor fluorophore was used. All these changes resulted in measurements with negative controls that showed high FRET efficiencies in comparison with the actual samples where interaction was expected (see Figure 6-29). Thus, the interpretation of the results from the HIF-1α + FIH measurement is very problematic (see Figure 6-29 C). The interaction of HIF-1α and FIH could not be proven in these seFRET experiments. Measurements for HIF-1α and ARNT were negative, either, and are therefore hardly comparable to the literature. The results were independent from the cell type (HEK293T or U2OS) or from the combination of donor and acceptor. HIF-1α tagged with the donor mTurquoise2 showed similar results with mCitrine-tagged ARNT as ARNT with mTurquoise2 as the donor with mCitrine-HIF-1α as the acceptor (see Figure 6-29 A and B).

As a first optimization of the setup, mKO2 was used as the acceptor fluorophore. Interestingly, the negative control appeared completely negative in this experiment. In comparison, mTurq2-HIF-1α + mKO2-ARNT showed a clear positive signal with a FRET efficiency of 0.07. The results of the measurement with mTurq2-HIF-1α and mKO2-FIH were diverse. Some cells showed no interaction at all with an efficiency of 0 as the negative control. But some cells reached an efficiency value of 0.3 which was not observed in the negative control (see Figure 6-30). Possibly, these cells with a high FRET efficiency had grown very dense to other cells and lived under hypoxic conditions that influenced the interaction between HIF-1α and FIH. To study the effect of hypoxia, seFRET measurements should be conducted in a hypoxic chamber with low oxygen levels for all cells in the samples. Another explanation could lie in the localization of HIF-1α and FIH. Having a look at the pictures from the fluorescence microscope (see Figure 6-27 C and E), it can be seen that FIH was mainly located in the cytoplasm while HIF-1α accumulated in the nucleus. An analysis that considers these cell compartments individually might reveal a correlation between localization and FRET efficiency. First differentiated analyses were done in the Bachelor's thesis of Rebecca Mohr showing no differences in efficiency values from cytoplasm and nucleus analyses (Mohr, 2018).

In the Co-IP experiments, the mCherry-FIH construct showed a band that could not be assigned to the expected fusion protein (see Figure 6-26). In mCitrine-FIH as well as mCherry-FIH, the FIH protein was tagged on to the C-terminus. Possibly, tagging a fluorophore to this terminus prevents interaction of the FIH protein or leads to a still unknown mechanism that ends in the two bands of the Western Blot and the negative seFRET results. This does not explain the measurements with the construct mKO2-FIH, which were partly positive, and the difficulties of showing the interaction between HIF-1α and ARNT. But as every fluorophore is derived from a different organism and has diverse properties, the effects on the tagged protein can vary from construct to construct and can be influenced by the experimental conditions.

These experiments thus need to be repeated in the future to prove the interaction of HIF-1α and FIH in living cells by seFRET. With a reproducible FRET measurement that shows the interaction of HIF-1α and FIH it would then be possible to observe the effect of mutations in HIF-α, the presence of inhibitors or a different HIF-α subunit on the interaction capability as it was done for the interaction of HIF-1α and p300 (Kim *et al.*, 2014) or HIF-α and ARNT (Kim *et al.*, 2015) (Pisarenko, 2017). To apply an alternative and quantitative method for *in vivo* interaction studies using the FRET principle, FLIM experiments were conducted additionally.

FLIM measurements for the proof of HIF-1α/FIH interaction *in vivo* were carried out with the mCitrine-HIF-1α and FIH-mCherry constructs, which are appropriate for the FLIM setup, but

not suitable for our seFRET system due to laser wavelength limitations. A negative and positive control revealed the functionality of the method itself and the appropriateness of HEK293T cells for this method. As a control for a FLIM suitable HIF-1α-tagged protein, the interaction of HIF-1α and ARNT was measured. The mean α-value of mCitrine-HIF-1α and mCherry-ARNT transfected cells was significantly increased in comparison to the negative control and confirmed the usability of the setup for our interaction studies. Measurements with the constructs of interest mCitrine-HIF-1α and FIH-mCherry resulted in an α-value of 0.03. This was significantly higher than the negative control although the absolute value was low (see Figure 6-31). The FLIM measurements therefore revealed the interaction of HIF-1α and FIH *in vivo*.

As FRET measurements for HIF-1α and PHD2 showed positive results after DMOG treatment (Pientka *et al.*, 2012), DMOG was added before the measurement. In these experiments, the basic level of the α-values was higher than in the measurements before: the negative control had an α of 0.09, while HIF-1α + ARNT was at 0.24. Again, the interaction of HIF-1α and FIH showed a lower value than HIF-1α and ARNT (α = 0.17). DMOG treatment led to a significantly increased α-value in both samples mCitrine-HIF-1α + mCherry-ARNT (α = 0.31) and mCitrine-HIF-1α + mCherry-FIH (α = 0.38) (see Figure 6-32). In the measurements for HIF-1α and ARNT, DMOG could have led to a higher amount of unhydroxylated HIF-1α, as the PHDs and FIH were inhibited, and therefore to a stronger interaction signal with ARNT. The α-value for HIF-1α + FIH increased even more due to the DMOG treatment. Possibly, the inhibition of FIH by the 2-oxoglutarate analog DMOG also led to a prolonged interaction of FIH with its substrate HIF-1α resulting in a higher α-value. The experiments with DMOG confirmed the former results of a positive FRET signal in the FLIM measurements of HIF-1α and FIH. As the next step it would be interesting to measure the interaction of HIF-1α with FIH under hypoxia. Depending on the interaction mechanism, it could prolong the interaction similarly to DMOG treatment or it might prevent the interaction at all. For HIF-1α/ARNT interaction studies with the seFRET system, no differences between normoxic and hypoxic measurements could be found (Konietzny *et al.*, 2009).

So far, interaction studies using FLIM with the HIF-1α protein are rare. Conformational changes in the HIF-3α inhibitory PAS domain due to binding to HIF-1α were demonstrated (Kasai *et al.*, 2017). The interaction of HIF-1α and ARNT, which served as a positive control in this study, was also revealed by FLIM (Prost-Fingerle *et al.*, 2017, Schutzhold *et al.*, 2018).

8 References

Agoff, S. N., Brentnall, T. A., Crispin, D. A., Taylor, S. L., Raaka, S., Haggitt, R. C., Reed, M. W., Afonina, I. A., Rabinovitch, P. S., Stevens, A. C., Feng, Z. & Bronner, M. P. 2000. The role of cyclooxygenase 2 in ulcerative colitis-associated neoplasia. *Am J Pathol,* 157**,** 737-45.

An, W. G., Kanekal, M., Simon, M. C., Maltepe, E., Blagosklonny, M. V. & Neckers, L. M. 1998. Stabilization of wild-type p53 by hypoxia-inducible factor 1alpha. *Nature,* 392**,** 405-8.

Arthur, J. C., Perez-Chanona, E., Muhlbauer, M., Tomkovich, S., Uronis, J. M., Fan, T. J., Campbell, B. J., Abujamel, T., Dogan, B., Rogers, A. B., Rhodes, J. M., Stintzi, A., Simpson, K. W., Hansen, J. J., Keku, T. O., Fodor, A. A. & Jobin, C. 2012. Intestinal inflammation targets cancer-inducing activity of the microbiota. *Science,* 338**,** 120-3.

Backer, V., Cheung, F. Y., Siveke, J. T., Fandrey, J. & Winning, S. 2017. Knockdown of myeloid cell hypoxia-inducible factor-1alpha ameliorates the acute pathology in DSS-induced colitis. *PLoS One,* 12**,** e0190074.

Becker, C., Fantini, M. C., Wirtz, S., Nikolaev, A., Lehr, H. A., Galle, P. R., Rose-John, S. & Neurath, M. F. 2005. IL-6 signaling promotes tumor growth in colorectal cancer. *Cell Cycle,* 4**,** 217-20.

Bertout, J. A., Patel, S. A. & Simon, M. C. 2008. The impact of O2 availability on human cancer. *Nat Rev Cancer,* 8**,** 967-75.

Bonello, S., Zahringer, C., Belaiba, R. S., Djordjevic, T., Hess, J., Michiels, C., Kietzmann, T. & Gorlach, A. 2007. Reactive oxygen species activate the HIF-1alpha promoter via a functional NFkappaB site. *Arterioscler Thromb Vasc Biol,* 27**,** 755-61.

Campbell, E. L., Bruyninckx, W. J., Kelly, C. J., Glover, L. E., Mcnamee, E. N., Bowers, B. E., Bayless, A. J., Scully, M., Saeedi, B. J., Golden-Mason, L., Ehrentraut, S. F., Curtis, V. F., Burgess, A., Garvey, J. F., Sorensen, A., Nemenoff, R., Jedlicka, P., Taylor, C. T., Kominsky, D. J. & Colgan, S. P. 2014. Transmigrating neutrophils shape the mucosal microenvironment through localized oxygen depletion to influence resolution of inflammation. *Immunity,* 40**,** 66-77.

Chan, M. C., Holt-Martyn, J. P., Schofield, C. J. & Ratcliffe, P. J. 2016. Pharmacological targeting of the HIF hydroxylases--A new field in medicine development. *Mol Aspects Med,* 47-48**,** 54-75.

Chang, S. W., Yue, J., Wang, B. C. & Zhang, X. L. 2015. miR-503 inhibits cell proliferation and induces apoptosis in colorectal cancer cells by targeting E2F3. *Int J Clin Exp Pathol,* 8**,** 12853-60.

Chang, W. C., Coudry, R. A., Clapper, M. L., Zhang, X., Williams, K. L., Spittle, C. S., Li, T. & Cooper, H. S. 2007. Loss of p53 enhances the induction of colitis-associated neoplasia by dextran sulfate sodium. *Carcinogenesis,* 28**,** 2375-81.

Chen, D., Li, M., Luo, J. & Gu, W. 2003. Direct interactions between HIF-1 alpha and Mdm2 modulate p53 function. *J Biol Chem,* 278**,** 13595-8.

Chen, T., Ren, Z., Ye, L. C., Zhou, P. H., Xu, J. M., Shi, Q., Yao, L. Q. & Zhong, Y. S. 2015a. Factor inhibiting HIF1alpha (FIH-1) functions as a tumor suppressor in human colorectal cancer by repressing HIF1alpha pathway. *Cancer Biol Ther,* 16**,** 244-52.

Chen, Y., Zhang, H. S., Fong, G. H., Xi, Q. L., Wu, G. H., Bai, C. G., Ling, Z. Q., Fan, L., Xu, Y. M., Qin, Y. Q., Yuan, T. L., Sun, H. & Fang, J. 2015b. PHD3 Stabilizes the Tight Junction Protein Occludin and Protects Intestinal Epithelial Barrier Function. *J Biol Chem,* 290**,** 20580-9.

Cheng, C., Hua, J., Tan, J., Qian, W., Zhang, L. & Hou, X. 2019. Identification of differentially expressed genes, associated functional terms pathways, and candidate diagnostic biomarkers in inflammatory bowel diseases by bioinformatics analysis. *Exp Ther Med,* 18**,** 278-288.

Churchill-Davidson, I., Sanger, C. & Thomlinson, R. H. 1955. High-pressure oxygen and radiotherapy. *Lancet,* 268**,** 1091-5.

Clapper, M. L., Cooper, H. S. & Chang, W. C. 2007. Dextran sulfate sodium-induced colitis-associated neoplasia: a promising model for the development of chemopreventive interventions. *Acta Pharmacol Sin,* 28**,** 1450-9.

Clayton, A. H., Hanley, Q. S. & Verveer, P. J. 2004. Graphical representation and multicomponent analysis of single-frequency fluorescence lifetime imaging microscopy data. *J Microsc,* 213**,** 1-5.

Cockman, M. E., Lancaster, D. E., Stolze, I. P., Hewitson, K. S., Mcdonough, M. A., Coleman, M. L., Coles, C. H., Yu, X., Hay, R. T., Ley, S. C., Pugh, C. W., Oldham, N. J., Masson, N., Schofield, C. J. & Ratcliffe, P. J. 2006. Posttranslational hydroxylation of ankyrin repeats in IkappaB proteins by the hypoxia-inducible factor (HIF) asparaginyl hydroxylase, factor inhibiting HIF (FIH). *Proc Natl Acad Sci U S A,* 103**,** 14767-72.

Coskun, M. 2014. Intestinal epithelium in inflammatory bowel disease. *Front Med (Lausanne),* 1**,** 24.

Cramer, T., Yamanishi, Y., Clausen, B. E., Forster, I., Pawlinski, R., Mackman, N., Haase, V. H., Jaenisch, R., Corr, M., Nizet, V., Firestein, G. S., Gerber, H. P., Ferrara, N. & Johnson, R. S. 2003. HIF-1alpha is essential for myeloid cell-mediated inflammation. *Cell,* 112**,** 645-57.

Cummins, E. P., Berra, E., Comerford, K. M., Ginouves, A., Fitzgerald, K. T., Seeballuck, F., Godson, C., Nielsen, J. E., Moynagh, P., Pouyssegur, J. & Taylor, C. T. 2006. Prolyl hydroxylase-1 negatively regulates IkappaB kinase-

beta, giving insight into hypoxia-induced NFkappaB activity. *Proc Natl Acad Sci U S A,* 103**,** 18154-9.

Cummins, E. P., Seeballuck, F., Keely, S. J., Mangan, N. E., Callanan, J. J., Fallon, P. G. & Taylor, C. T. 2008. The hydroxylase inhibitor dimethyloxalylglycine is protective in a murine model of colitis. *Gastroenterology,* 134**,** 156-65.

Day, R. N. & Davidson, M. W. 2009. The fluorescent protein palette: tools for cellular imaging. *Chem Soc Rev,* 38**,** 2887-921.

Del Peso, L., Castellanos, M. C., Temes, E., Martin-Puig, S., Cuevas, Y., Olmos, G. & Landazuri, M. O. 2003. The von Hippel Lindau/hypoxia-inducible factor (HIF) pathway regulates the transcription of the HIF-proline hydroxylase genes in response to low oxygen. *J Biol Chem,* 278**,** 48690-5.

Deschoemaeker, S., Di Conza, G., Lilla, S., Martin-Perez, R., Mennerich, D., Boon, L., Hendrikx, S., Maddocks, O. D., Marx, C., Radhakrishnan, P., Prenen, H., Schneider, M., Myllyharju, J., Kietzmann, T., Vousden, K. H., Zanivan, S. & Mazzone, M. 2015. PHD1 regulates p53-mediated colorectal cancer chemoresistance. *EMBO Mol Med,* 7**,** 1350-65.

Ema, M., Taya, S., Yokotani, N., Sogawa, K., Matsuda, Y. & Fujii-Kuriyama, Y. 1997. A novel bHLH-PAS factor with close sequence similarity to hypoxia-inducible factor 1alpha regulates the VEGF expression and is potentially involved in lung and vascular development. *Proc Natl Acad Sci U S A,* 94**,** 4273-8.

Escribese, M. M., Sierra-Filardi, E., Nieto, C., Samaniego, R., Sanchez-Torres, C., Matsuyama, T., Calderon-Gomez, E., Vega, M. A., Salas, A., Sanchez-Mateos, P. & Corbi, A. L. 2012. The prolyl hydroxylase PHD3 identifies proinflammatory macrophages and its expression is regulated by activin A. *J Immunol,* 189**,** 1946-54.

Fandrey, J., Gorr, T. A. & Gassmann, M. 2006. Regulating cellular oxygen sensing by hydroxylation. *Cardiovasc Res,* 71**,** 642-51.

Fearon, E. R. & Vogelstein, B. 1990. A genetic model for colorectal tumorigenesis. *Cell,* 61**,** 759-67.

Fluck, K., Breves, G., Fandrey, J. & Winning, S. 2016. Hypoxia-inducible factor 1 in dendritic cells is crucial for the activation of protective regulatory T cells in murine colitis. *Mucosal Immunol,* 9**,** 379-90.

Ford, A. C., Moayyedi, P. & Hanauer, S. B. 2013. Ulcerative colitis. *Bmj,* 346**,** f432.

Förster, T. 1948. Zwischenmolekulare Energiewanderung und Fluoreszenz. *Annalen der Physik,* 437**,** 55-75.

Frede, S., Stockmann, C., Freitag, P. & Fandrey, J. 2006. Bacterial lipopolysaccharide induces HIF-1 activation in human monocytes via p44/42 MAPK and NF-kappaB. *Biochem J,* 396**,** 517-27.

Fujii, S., Fujimori, T., Kawamata, H., Takeda, J., Kitajima, K., Omotehara, F., Kaihara, T., Kusaka, T., Ichikawa, K., Ohkura, Y., Ono, Y., Imura, J., Yamaoka, S., Sakamoto, C., Ueda, Y. & Chiba, T. 2004. Development of colonic neoplasia in p53 deficient mice with experimental colitis induced by dextran sulphate sodium. *Gut,* 53**,** 710-6.

Gorelik, L. & Flavell, R. A. 2000. Abrogation of TGFbeta signaling in T cells leads to spontaneous T cell differentiation and autoimmune disease. *Immunity,* 12**,** 171-81.

Grecco, H. E., Roda-Navarro, P. & Verveer, P. J. 2009. Global analysis of time correlated single photon counting FRET-FLIM data. *Opt Express,* 17**,** 6493-508.

Greten, F. R., Eckmann, L., Greten, T. F., Park, J. M., Li, Z. W., Egan, L. J., Kagnoff, M. F. & Karin, M. 2004. IKKbeta links inflammation and tumorigenesis in a mouse model of colitis-associated cancer. *Cell,* 118**,** 285-96.

Grossman, S. R. 2001. p300/CBP/p53 interaction and regulation of the p53 response. *Eur J Biochem,* 268**,** 2773-8.

Hatoum, O. A., Miura, H. & Binion, D. G. 2003. The vascular contribution in the pathogenesis of inflammatory bowel disease. *Am J Physiol Heart Circ Physiol,* 285**,** H1791-6.

Henze, A. T. & Acker, T. 2010. Feedback regulators of hypoxia-inducible factors and their role in cancer biology. *Cell Cycle,* 9**,** 2749-63.

Hindryckx, P., De Vos, M., Jacques, P., Ferdinande, L., Peeters, H., Olievier, K., Bogaert, S., Brinkman, B., Vandenabeele, P., Elewaut, D. & Laukens, D. 2010. Hydroxylase inhibition abrogates TNF-alpha-induced intestinal epithelial damage by hypoxia-inducible factor-1-dependent repression of FADD. *J Immunol,* 185**,** 6306-16.

Hirsila, M., Koivunen, P., Gunzler, V., Kivirikko, K. I. & Myllyharju, J. 2003. Characterization of the human prolyl 4-hydroxylases that modify the hypoxia-inducible factor. *J Biol Chem,* 278**,** 30772-80.

Hochreiter, B., Kunze, M., Moser, B. & Schmid, J. A. 2019. Advanced FRET normalization allows quantitative analysis of protein interactions including stoichiometries and relative affinities in living cells. *Sci Rep,* 9**,** 8233.

Hockel, M. & Vaupel, P. 2001. Tumor hypoxia: definitions and current clinical, biologic, and molecular aspects. *J Natl Cancer Inst,* 93**,** 266-76.

Hu, J., Bernardini, A. & Fandrey, J. 2016. Optical Analysis of Hypoxia Inducible Factor (HIF)-1 Complex Assembly: Imaging of Cellular Oxygen Sensing. *Adv Exp Med Biol,* 903**,** 247-58.

Huang, L. E., Gu, J., Schau, M. & Bunn, H. F. 1998. Regulation of hypoxia-inducible factor 1alpha is mediated by an O2-dependent degradation domain via the ubiquitin-proteasome pathway. *Proc Natl Acad Sci U S A,* 95**,** 7987-92.

Humbert, P. O., Verona, R., Trimarchi, J. M., Rogers, C., Dandapani, S. & Lees, J. A. 2000. E2f3 is critical for normal cellular proliferation. *Genes Dev,* 14**,** 690-703.

Ivanov, S. V., Salnikow, K., Ivanova, A. V., Bai, L. & Lerman, M. I. 2007. Hypoxic repression of STAT1 and its downstream genes by a pVHL/HIF-1 target DEC1/STRA13. *Oncogene,* 26**,** 802-12.

Jaakkola, P., Mole, D. R., Tian, Y. M., Wilson, M. I., Gielbert, J., Gaskell, S. J., Von Kriegsheim, A., Hebestreit, H. F., Mukherji, M., Schofield, C. J., Maxwell, P. H., Pugh, C. W. & Ratcliffe, P. J. 2001. Targeting of HIF-alpha to the von Hippel-Lindau ubiquitylation complex by O2-regulated prolyl hydroxylation. *Science,* 292**,** 468-72.

Jiang, B. H., Zheng, J. Z., Leung, S. W., Roe, R. & Semenza, G. L. 1997. Transactivation and inhibitory domains of hypoxia-inducible factor 1alpha. Modulation of transcriptional activity by oxygen tension. *J Biol Chem,* 272**,** 19253-60.

Kai, Y., Takahashi, I., Ishikawa, H., Hiroi, T., Mizushima, T., Matsuda, C., Kishi, D., Hamada, H., Tamagawa, H., Ito, T., Yoshizaki, K., Kishimoto, T., Matsuda, H. & Kiyono, H. 2005. Colitis in mice lacking the common cytokine receptor gamma chain is mediated by IL-6-producing CD4+ T cells. *Gastroenterology,* 128**,** 922-34.

Karhausen, J., Furuta, G. T., Tomaszewski, J. E., Johnson, R. S., Colgan, S. P. & Haase, V. H. 2004. Epithelial hypoxia-inducible factor-1 is protective in murine experimental colitis. *J Clin Invest,* 114**,** 1098-106.

Kasai, S., Kajimoto, S., Ito, Y., Saito, T., Yasumoto, K. I., Tokunaga, M., Sakata-Sogawa, K., Fukumura, H. & Sogawa, K. 2017. Conformational changes in inhibitory PAS domain protein associated with binding of HIF-1alpha and Bcl-xL in living cells. *J Biochem,* 161**,** 291-296.

Kim, J. J., Shajib, M. S., Manocha, M. M. & Khan, W. I. 2012. Investigating intestinal inflammation in DSS-induced model of IBD. *J Vis Exp*.

Kim, S. H., Hwang, D., Park, H., Yang, E. G., Chung, H. S. & Kim, S. Y. 2015. The action of HIF-3alpha variants on HIF-2alpha-HIF-1beta heterodimer formation is directly probed in live cells. *Exp Cell Res,* 336**,** 329-37.

Kim, S. Y., Lee, M. J., Na, Y. R., Kim, S. Y. & Yang, E. G. 2014. Visualization of hypoxia-inducible factor 1alpha-p300 interactions in live cells by fluorescence resonance energy transfer. *J Cell Biochem,* 115**,** 271-80.

Kitahara, O., Furukawa, Y., Tanaka, T., Kihara, C., Ono, K., Yanagawa, R., Nita, M. E., Takagi, T., Nakamura, Y. & Tsunoda, T. 2001. Alterations of gene expression during colorectal carcinogenesis revealed by cDNA microarrays

after laser-capture microdissection of tumor tissues and normal epithelia. *Cancer Res,* 61**,** 3544-9.

Koivunen, P., Hirsila, M., Gunzler, V., Kivirikko, K. I. & Myllyharju, J. 2004. Catalytic properties of the asparaginyl hydroxylase (FIH) in the oxygen sensing pathway are distinct from those of its prolyl 4-hydroxylases. *J Biol Chem,* 279**,** 9899-904.

Konietzny, R., Konig, A., Wotzlaw, C., Bernadini, A., Berchner-Pfannschmidt, U. & Fandrey, J. 2009. Molecular imaging: into in vivo interaction of HIF-1alpha and HIF-2alpha with ARNT. *Ann N Y Acad Sci,* 1177**,** 74-81.

Laemmli, U. K. 1970. Cleavage of structural proteins during the assembly of the head of bacteriophage T4. *Nature,* 227**,** 680-5.

Lakatos, P. L. & Lakatos, L. 2008. Risk for colorectal cancer in ulcerative colitis: changes, causes and management strategies. *World J Gastroenterol,* 14**,** 3937-47.

Lancaster, D. E., Mcneill, L. A., Mcdonough, M. A., Aplin, R. T., Hewitson, K. S., Pugh, C. W., Ratcliffe, P. J. & Schofield, C. J. 2004. Disruption of dimerization and substrate phosphorylation inhibit factor inhibiting hypoxia-inducible factor (FIH) activity. *Biochem J,* 383**,** 429-37.

Lando, D., Peet, D. J., Gorman, J. J., Whelan, D. A., Whitelaw, M. L. & Bruick, R. K. 2002a. FIH-1 is an asparaginyl hydroxylase enzyme that regulates the transcriptional activity of hypoxia-inducible factor. *Genes Dev,* 16**,** 1466-71.

Lando, D., Peet, D. J., Whelan, D. A., Gorman, J. J. & Whitelaw, M. L. 2002b. Asparagine hydroxylation of the HIF transactivation domain a hypoxic switch. *Science,* 295**,** 858-61.

Lawson, M. M., Thomas, A. G. & Akobeng, A. K. 2006. Tumour necrosis factor alpha blocking agents for induction of remission in ulcerative colitis. *Cochrane Database Syst Rev***,** Cd005112.

Leon-Cabrera, S., Vazquez-Sandoval, A., Molina-Guzman, E., Delgado-Ramirez, Y., Delgado-Buenrostro, N. L., Callejas, B. E., Chirino, Y. I., Perez-Plasencia, C., Rodriguez-Sosa, M., Olguin, J. E., Salinas, C., Satoskar, A. R. & Terrazas, L. I. 2018. Deficiency in STAT1 Signaling Predisposes Gut Inflammation and Prompts Colorectal Cancer Development. *Cancers (Basel),* 10.

Liang, K., Ding, X. Q., Lin, C. & Kang, Y. J. 2015. Featured Article: Hypoxia-inducible factor-1alpha dependent nuclear entry of factor inhibiting HIF-1. *Exp Biol Med (Maywood),* 240**,** 1446-51.

Linke, S., Stojkoski, C., Kewley, R. J., Booker, G. W., Whitelaw, M. L. & Peet, D. J. 2004. Substrate requirements of the oxygen-sensing asparaginyl hydroxylase factor-inhibiting hypoxia-inducible factor. *J Biol Chem,* 279**,** 14391-7.

Livak, K. J. & Schmittgen, T. D. 2001. Analysis of relative gene expression data using real-time quantitative PCR and the 2(-Delta Delta C(T)) Method. *Methods,* 25**,** 402-8.

Lopez, A., Pouillon, L., Beaugerie, L., Danese, S. & Peyrin-Biroulet, L. 2018. Colorectal cancer prevention in patients with ulcerative colitis. *Best Pract Res Clin Gastroenterol,* 32-33**,** 103-109.

Lowry, O. H., Rosebrough, N. J., Farr, A. L. & Randall, R. J. 1951. Protein measurement with the Folin phenol reagent. *J Biol Chem,* 193**,** 265-75.

Macdonald, T. T. & Monteleone, G. 2005. Immunity, inflammation, and allergy in the gut. *Science,* 307**,** 1920-5.

Madison, B. B., Dunbar, L., Qiao, X. T., Braunstein, K., Braunstein, E. & Gumucio, D. L. 2002. Cis elements of the villin gene control expression in restricted domains of the vertical (crypt) and horizontal (duodenum, cecum) axes of the intestine. *J Biol Chem,* 277**,** 33275-83.

Mahon, P. C., Hirota, K. & Semenza, G. L. 2001. FIH-1: a novel protein that interacts with HIF-1alpha and VHL to mediate repression of HIF-1 transcriptional activity. *Genes Dev,* 15**,** 2675-86.

Maxwell, P. H., Wiesener, M. S., Chang, G. W., Clifford, S. C., Vaux, E. C., Cockman, M. E., Wykoff, C. C., Pugh, C. W., Maher, E. R. & Ratcliffe, P. J. 1999. The tumour suppressor protein VHL targets hypoxia-inducible factors for oxygen-dependent proteolysis. *Nature,* 399**,** 271-5.

Mohr, R. 2018. Protein-protein interaction studies for FIH and HIF via FRET. Bachelor Thesis. Rhine-Waal University of applied Sciences. *unpublished*.

Moser, S. C., Bensaddek, D., Ortmann, B., Maure, J. F., Mudie, S., Blow, J. J., Lamond, A. I., Swedlow, J. R. & Rocha, S. 2013. PHD1 links cell-cycle progression to oxygen sensing through hydroxylation of the centrosomal protein Cep192. *Dev Cell,* 26**,** 381-92.

Muniz, L. R., Knosp, C. & Yeretssian, G. 2012. Intestinal antimicrobial peptides during homeostasis, infection, and disease. *Front Immunol,* 3**,** 310.

Munkholm, P. 2003. Review article: the incidence and prevalence of colorectal cancer in inflammatory bowel disease. *Aliment Pharmacol Ther,* 18 Suppl 2**,** 1-5.

Neurath, M. F. 2014. Cytokines in inflammatory bowel disease. *Nat Rev Immunol,* 14**,** 329-42.

Nunes, N. S., Kim, S., Sundby, M., Chandran, P., Burks, S. R., Paz, A. H. & Frank, J. A. 2018. Temporal clinical, proteomic, histological and cellular immune responses of dextran sulfate sodium-induced acute colitis. *World J Gastroenterol,* 24**,** 4341-4355.

Ogino, T., Nishimura, J., Barman, S., Kayama, H., Uematsu, S., Okuzaki, D., Osawa, H., Haraguchi, N., Uemura, M., Hata, T., Takemasa, I., Mizushima, T., Yamamoto, H., Takeda, K., Doki, Y. & Mori, M. 2013. Increased Th17-inducing activity of CD14+ CD163 low myeloid cells in intestinal lamina propria of patients with Crohn's disease. *Gastroenterology,* 145**,** 1380-91.e1.

Ohkawara, T., Mitsuyama, K., Takeda, H., Asaka, M., Fujiyama, Y. & Nishihira, J. 2008. Lack of macrophage migration inhibitory factor suppresses innate immune response in murine dextran sulfate sodium-induced colitis. *Scand J Gastroenterol,* 43**,** 1497-504.

Ohkusa, T. 1985. [Production of experimental ulcerative colitis in hamsters by dextran sulfate sodium and changes in intestinal microflora]. *Nihon Shokakibyo Gakkai Zasshi,* 82**,** 1327-36.

Okayasu, I., Hatakeyama, S., Yamada, M., Ohkusa, T., Inagaki, Y. & Nakaya, R. 1990. A novel method in the induction of reliable experimental acute and chronic ulcerative colitis in mice. *Gastroenterology,* 98**,** 694-702.

Palazon, A., Tyrakis, P. A., Macias, D., Velica, P., Rundqvist, H., Fitzpatrick, S., Vojnovic, N., Phan, A. T., Loman, N., Hedenfalk, I., Hatschek, T., Lovrot, J., Foukakis, T., Goldrath, A. W., Bergh, J. & Johnson, R. S. 2017. An HIF-1alpha/VEGF-A Axis in Cytotoxic T Cells Regulates Tumor Progression. *Cancer Cell,* 32**,** 669-683.e5.

Parang, B., Barrett, C. W. & Williams, C. S. 2016. AOM/DSS Model of Colitis-Associated Cancer. *Methods Mol Biol,* 1422**,** 297-307.

Pientka, F. K., Hu, J., Schindler, S. G., Brix, B., Thiel, A., Johren, O., Fandrey, J., Berchner-Pfannschmidt, U. & Depping, R. 2012. Oxygen sensing by the prolyl-4-hydroxylase PHD2 within the nuclear compartment and the influence of compartmentalisation on HIF-1 signalling. *J Cell Sci,* 125**,** 5168-76.

Pisarenko, I. 2017. Interaktionsanalyse der Hypoxia-induzierbaren Trankriptionsfaktoren HIF-2alpha und ARNT unter Berücksichtigung der Einflussnahme durch den HIF-2alpha-Liganden N-(3-Chloro-5-fluorophenyl)-4-nitrobenzo[c][1,2,5]oxadiazol-5-amine und verschiedener HIF-2alpha-Mutationen. PhD Thesis. University of Duisburg-Essen.

Prost-Fingerle, K., Hoffmann, M. D., Schutzhold, V., Cantore, M. & Fandrey, J. 2017. Optical analysis of cellular oxygen sensing. *Exp Cell Res,* 356**,** 122-127.

Rodriguez, J., Herrero, A., Li, S., Rauch, N., Quintanilla, A., Wynne, K., Krstic, A., Acosta, J. C., Taylor, C., Schlisio, S. & Von Kriegsheim, A. 2018. PHD3 Regulates p53 Protein Stability by Hydroxylating Proline 359. *Cell Rep,* 24**,** 1316-1329.

Rodriguez, J., Pilkington, R., Garcia Munoz, A., Nguyen, L. K., Rauch, N., Kennedy, S., Monsefi, N., Herrero, A., Taylor, C. T. & Von Kriegsheim, A. 2016. Substrate-Trapped Interactors of PHD3 and FIH Cluster in Distinct Signaling Pathways. *Cell Rep,* 14**,** 2745-60.

Schmitz, H., Barmeyer, C., Fromm, M., Runkel, N., Foss, H. D., Bentzel, C. J., Riecken, E. O. & Schulzke, J. D. 1999. Altered tight junction structure contributes to the impaired epithelial barrier function in ulcerative colitis. *Gastroenterology,* 116**,** 301-9.

Scholz, C. C., Rodriguez, J., Pickel, C., Burr, S., Fabrizio, J. A., Nolan, K. A., Spielmann, P., Cavadas, M. A., Crifo, B., Halligan, D. N., Nathan, J. A., Peet, D. J., Wenger, R. H., Von Kriegsheim, A., Cummins, E. P. & Taylor, C. T. 2016. FIH Regulates Cellular Metabolism through Hydroxylation of the Deubiquitinase OTUB1. *PLoS Biol,* 14**,** e1002347.

Schultz, M., Tonkonogy, S. L., Sellon, R. K., Veltkamp, C., Godfrey, V. L., Kwon, J., Grenther, W. B., Balish, E., Horak, I. & Sartor, R. B. 1999. IL-2-deficient mice raised under germfree conditions develop delayed mild focal intestinal inflammation. *Am J Physiol,* 276**,** G1461-72.

Schutzhold, V., Fandrey, J. & Prost-Fingerle, K. 2018. Fluorescence Lifetime Imaging Microscopy (FLIM) as a Tool to Investigate Hypoxia-Induced Protein-Protein Interaction in Living Cells. *Methods Mol Biol,* 1742**,** 45-53.

Sellon, R. K., Tonkonogy, S., Schultz, M., Dieleman, L. A., Grenther, W., Balish, E., Rennick, D. M. & Sartor, R. B. 1998. Resident enteric bacteria are necessary for development of spontaneous colitis and immune system activation in interleukin-10-deficient mice. *Infect Immun,* 66**,** 5224-31.

Semenza, G. L. 2010. Defining the role of hypoxia-inducible factor 1 in cancer biology and therapeutics. *Oncogene,* 29**,** 625-34.

Semenza, G. L. 2013. HIF-1 mediates metabolic responses to intratumoral hypoxia and oncogenic mutations. *J Clin Invest,* 123**,** 3664-71.

Shaner, N. C., Steinbach, P. A. & Tsien, R. Y. 2005. A guide to choosing fluorescent proteins. *Nat Methods,* 2**,** 905-9.

Siegel, R. L., Miller, K. D., Fedewa, S. A., Ahnen, D. J., Meester, R. G. S., Barzi, A. & Jemal, A. 2017. Colorectal cancer statistics, 2017. *CA Cancer J Clin,* 67**,** 177-193.

Sim, J., Cowburn, A. S., Palazon, A., Madhu, B., Tyrakis, P. A., Macias, D., Bargiela, D. M., Pietsch, S., Gralla, M., Evans, C. E., Kittipassorn, T., Chey, Y. C. J., Branco, C. M., Rundqvist, H., Peet, D. J. & Johnson, R. S. 2018. The Factor Inhibiting HIF Asparaginyl Hydroxylase Regulates Oxidative Metabolism and Accelerates Metabolic Adaptation to Hypoxia. *Cell Metab,* 27**,** 898-913.e7.

Stewart, B. W., Wild, C.P., Editors 2015. World Cancer Report 2014. Lyon, France: International Agency for Research on Cancer.

Tanaka, T., Kohno, H., Suzuki, R., Hata, K., Sugie, S., Niho, N., Sakano, K., Takahashi, M. & Wakabayashi, K. 2006. Dextran sodium sulfate strongly promotes colorectal carcinogenesis in Apc(Min/+) mice: inflammatory stimuli

by dextran sodium sulfate results in development of multiple colonic neoplasms. *Int J Cancer,* 118**,** 25-34.

Tanaka, T., Kohno, H., Suzuki, R., Yamada, Y., Sugie, S. & Mori, H. 2003. A novel inflammation-related mouse colon carcinogenesis model induced by azoxymethane and dextran sodium sulfate. *Cancer Sci,* 94**,** 965-73.

Taniguchi, C. M., Miao, Y. R., Diep, A. N., Wu, C., Rankin, E. B., Atwood, T. F., Xing, L. & Giaccia, A. J. 2014. PHD inhibition mitigates and protects against radiation-induced gastrointestinal toxicity via HIF2. *Sci Transl Med,* 6**,** 236ra64.

Terzic, J., Grivennikov, S., Karin, E. & Karin, M. 2010. Inflammation and colon cancer. *Gastroenterology,* 138**,** 2101-2114.e5.

Thaker, A. I., Shaker, A., Rao, M. S. & Ciorba, M. A. 2012. Modeling colitis-associated cancer with azoxymethane (AOM) and dextran sulfate sodium (DSS). *J Vis Exp*.

Tian, H., Mcknight, S. L. & Russell, D. W. 1997. Endothelial PAS domain protein 1 (EPAS1), a transcription factor selectively expressed in endothelial cells. *Genes Dev,* 11**,** 72-82.

Towbin, H., Staehelin, T. & Gordon, J. 1979. Electrophoretic transfer of proteins from polyacrylamide gels to nitrocellulose sheets: procedure and some applications. *Proc Natl Acad Sci U S A,* 76**,** 4350-4.

Triner, D., Xue, X., Schwartz, A. J., Jung, I., Colacino, J. A. & Shah, Y. M. 2017. Epithelial Hypoxia-Inducible Factor 2alpha Facilitates the Progression of Colon Tumors through Recruiting Neutrophils. *Mol Cell Biol,* 37.

Ullah, K., Rosendahl, A. H., Izzi, V., Bergmann, U., Pihlajaniemi, T., Maki, J. M. & Myllyharju, J. 2017. Hypoxia-inducible factor prolyl-4-hydroxylase-1 is a convergent point in the reciprocal negative regulation of NF-kappaB and p53 signaling pathways. *Sci Rep,* 7**,** 17220.

Ungaro, R., Mehandru, S., Allen, P. B., Peyrin-Biroulet, L. & Colombel, J. F. 2017. Ulcerative colitis. *Lancet,* 389**,** 1756-1770.

Van Der Sluis, M., De Koning, B. A., De Bruijn, A. C., Velcich, A., Meijerink, J. P., Van Goudoever, J. B., Buller, H. A., Dekker, J., Van Seuningen, I., Renes, I. B. & Einerhand, A. W. 2006. Muc2-deficient mice spontaneously develop colitis, indicating that MUC2 is critical for colonic protection. *Gastroenterology,* 131**,** 117-29.

Van Uden, P., Kenneth, N. S. & Rocha, S. 2008. Regulation of hypoxia-inducible factor-1alpha by NF-kappaB. *Biochem J,* 412**,** 477-84.

Van Welden, S., Selfridge, A. C. & Hindryckx, P. 2017. Intestinal hypoxia and hypoxia-induced signalling as therapeutic targets for IBD. *Nat Rev Gastroenterol Hepatol,* 14**,** 596-611.

Vaupel, P. & Harrison, L. 2004. Tumor hypoxia: causative factors, compensatory mechanisms, and cellular response. *Oncologist,* 9 Suppl 5**,** 4-9.

Verveer, P. J., Squire, A. & Bastiaens, P. I. 2000. Global analysis of fluorescence lifetime imaging microscopy data. *Biophys J,* 78**,** 2127-37.

Vitale, I., Manic, G., Coussens, L. M., Kroemer, G. & Galluzzi, L. 2019. Macrophages and Metabolism in the Tumor Microenvironment. *Cell Metab,* 30**,** 36-50.

Vowinkel, T., Kalogeris, T. J., Mori, M., Krieglstein, C. F. & Granger, D. N. 2004. Impact of dextran sulfate sodium load on the severity of inflammation in experimental colitis. *Dig Dis Sci,* 49**,** 556-64.

Wang, B., Li, Y., Tan, F. & Xiao, Z. 2016. Increased expression of SOX4 is associated with colorectal cancer progression. *Tumour Biol,* 37**,** 9131-7.

Wang, G. L., Jiang, B. H., Rue, E. A. & Semenza, G. L. 1995a. Hypoxia-inducible factor 1 is a basic-helix-loop-helix-PAS heterodimer regulated by cellular O2 tension. *Proc Natl Acad Sci U S A,* 92**,** 5510-4.

Wang, G. L. & Semenza, G. L. 1995b. Purification and characterization of hypoxia-inducible factor 1. *J Biol Chem,* 270**,** 1230-7.

Wang, J., Zhu, J., Dong, M., Yu, H., Dai, X. & Li, K. 2014. Knockdown of tripartite motif containing 24 by lentivirus suppresses cell growth and induces apoptosis in human colorectal cancer cells. *Oncol Res,* 22**,** 39-45.

Wang, P., Guan, D., Zhang, X. P., Liu, F. & Wang, W. 2019. Modeling the regulation of p53 activation by HIF-1 upon hypoxia. *FEBS Lett,* 593**,** 2596-2611.

Wang, Y., Zhong, S., Schofield, C. J., Ratcliffe, P. J. & Lu, X. 2018. Nuclear entry and export of FIH are mediated by HIF1alpha and exportin1, respectively. *J Cell Sci,* 131.

Wenger, R. H. 2002. Cellular adaptation to hypoxia: O2-sensing protein hydroxylases, hypoxia-inducible transcription factors, and O2-regulated gene expression. *Faseb j,* 16**,** 1151-62.

Wigerup, C., Pahlman, S. & Bexell, D. 2016. Therapeutic targeting of hypoxia and hypoxia-inducible factors in cancer. *Pharmacol Ther,* 164**,** 152-69.

Wotzlaw, C., Gneuss, S., Konietzny, R. & Fandrey, J. 2010. Nanoscopy of the cellular response to hypoxia by means of fluorescence resonance energy transfer (FRET) and new FRET software. *PMC Biophys,* 3**,** 5.

Wotzlaw, C., Otto, T., Berchner-Pfannschmidt, U., Metzen, E., Acker, H. & Fandrey, J. 2007. Optical analysis of the HIF-1 complex in living cells by FRET and FRAP. *Faseb j,* 21**,** 700-7.

Xavier, R. J. & Podolsky, D. K. 2007. Unravelling the pathogenesis of inflammatory bowel disease. *Nature,* 448**,** 427-34.

Xie, H. & Simon, M. C. 2017. Oxygen availability and metabolic reprogramming in cancer. *J Biol Chem,* 292**,** 16825-16832.

Yahaya, M. a. F., Lila, M. a. M., Ismail, S., Zainol, M. & Afizan, N. 2019. Tumour-Associated Macrophages (TAMs) in Colon Cancer and How to Reeducate Them. *J Immunol Res,* 2019**,** 2368249.

Zhang, N., Fu, Z., Linke, S., Chicher, J., Gorman, J. J., Visk, D., Haddad, G. G., Poellinger, L., Peet, D. J., Powell, F. & Johnson, R. S. 2010. The asparaginyl hydroxylase factor inhibiting HIF-1alpha is an essential regulator of metabolism. *Cell Metab,* 11**,** 364-78.

Zheng, H., Lu, Z., Wang, R., Chen, N. & Zheng, P. 2016. Establishing the colitis-associated cancer progression mouse models. *Int J Immunopathol Pharmacol,* 29**,** 759-763.

Zheng, X., Zhai, B., Koivunen, P., Shin, S. J., Lu, G., Liu, J., Geisen, C., Chakraborty, A. A., Moslehi, J. J., Smalley, D. M., Wei, X., Chen, X., Chen, Z., Beres, J. M., Zhang, J., Tsao, J. L., Brenner, M. C., Zhang, Y., Fan, C., Depinho, R. A., Paik, J., Gygi, S. P., Kaelin, W. G., Jr. & Zhang, Q. 2014. Prolyl hydroxylation by EglN2 destabilizes FOXO3a by blocking its interaction with the USP9x deubiquitinase. *Genes Dev,* 28**,** 1429-44.

Zilles, K. T., B. N. 2010. *Anatomie,* Berlin, Heidelberg, Springer Berlin, Heidelberg.

9 Appendix

9.1 Supplementary figures

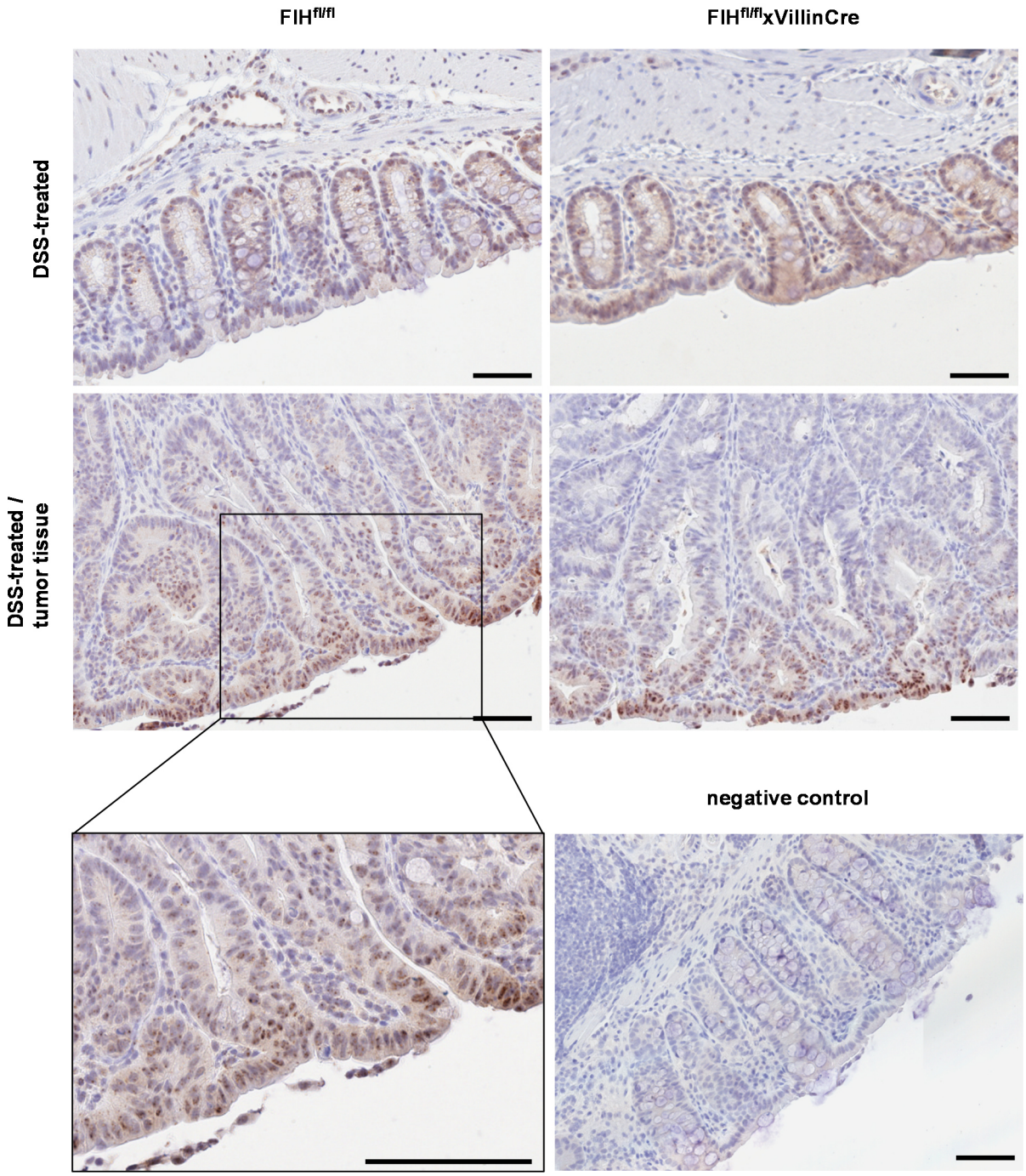

Figure 9-1: Immunohistochemical HIF-1α staining in colon tissue from AOM-DSS-treated mice. Scale bar = 50 µm.

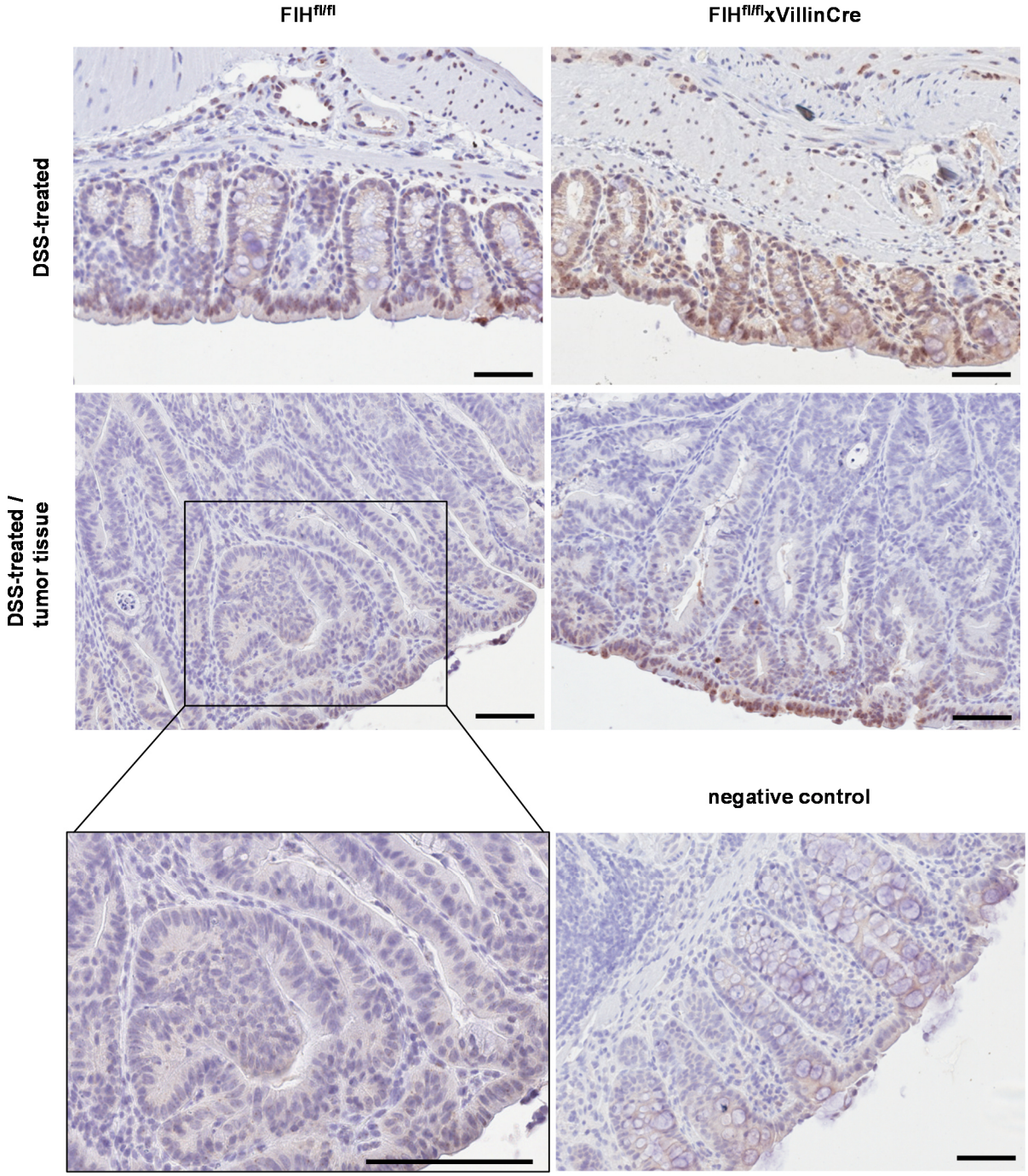

Figure 9-2: Immunohistochemical HIF-2α staining in AOM-DSS-treated mice. Normal colon tissue as well as tumor tissue are compared between FIH$^{fl/fl}$ and FIH$^{fl/fl}$xVillinCre mice. Scale bar = 50 µm.

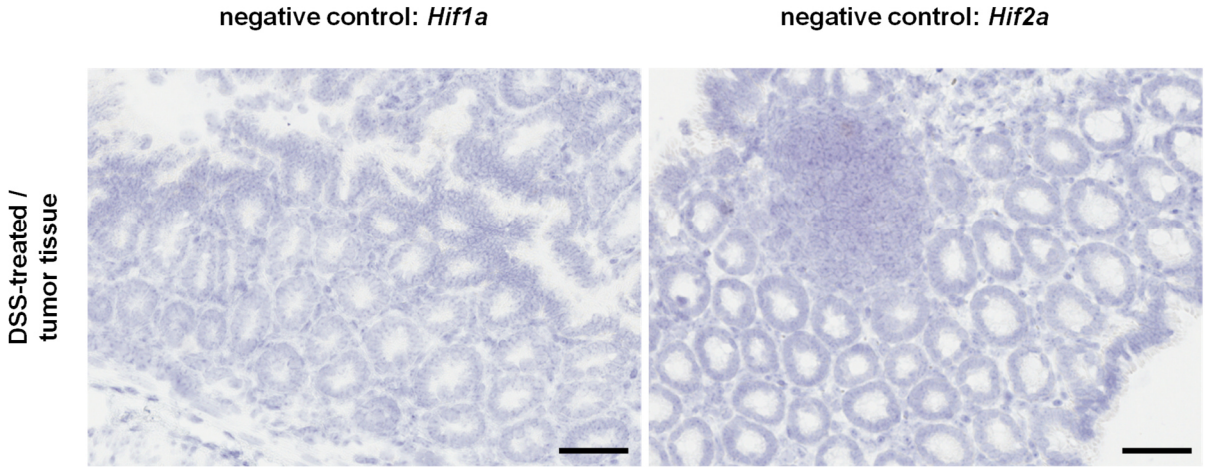

Figure 9-3: Negative control for the *in situ* hybridization with RNAscope®. Slides are completely blank for DAB staining without *Hif1a* and *Hif2a* probes revealing the specificity of the amplification system. Scale bar = 50 µm.

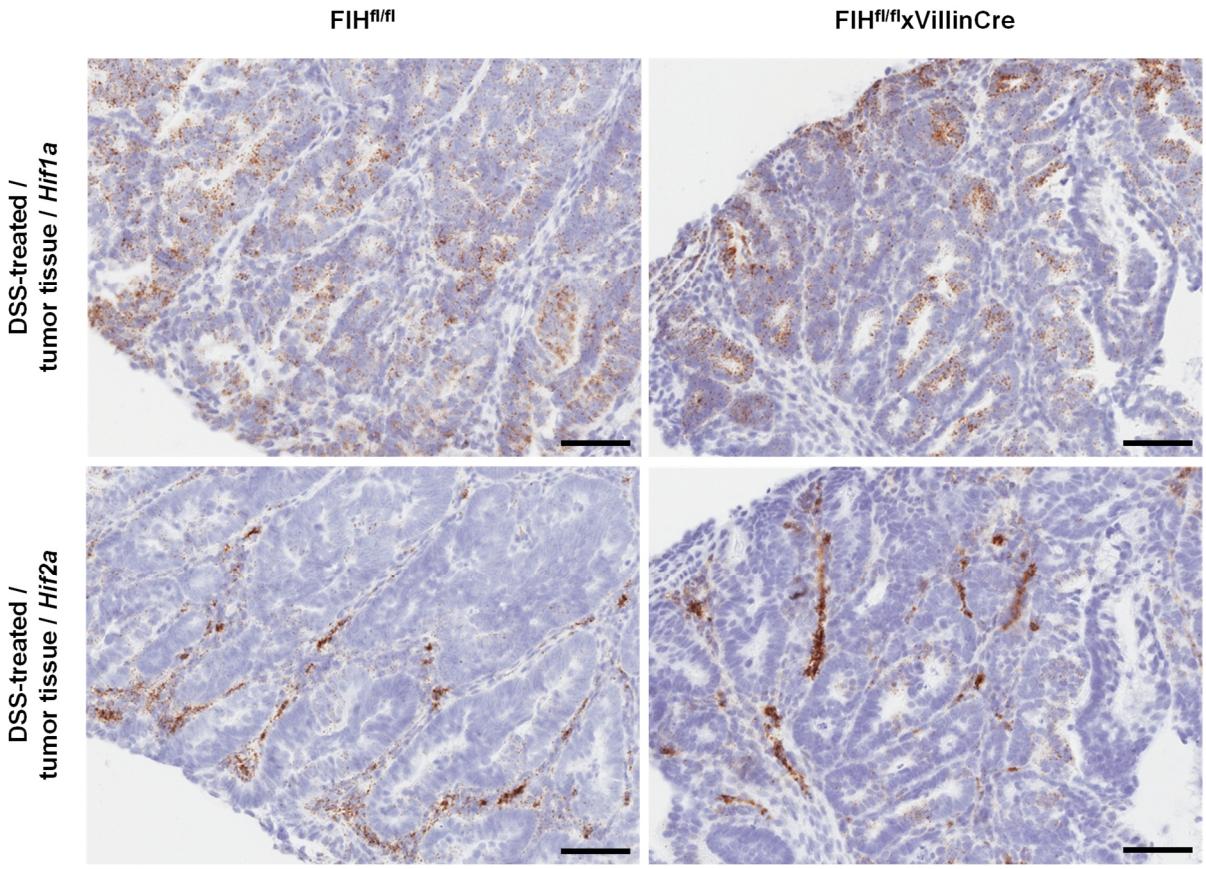

Figure 9-4: Detection of *Hif1a* and *Hif2a* mRNA by *in situ* hybridization in AOM-DSS-treated mice. Colon tumor tissue was stained for HIF-α mRNA in FIH$^{fl/fl}$ and FIH$^{fl/fl}$xVillinCre mice. Scale bar = 50 µm.

9.2 Table of figures

FIGURE 3-1: ULCERATIVE COLITIS AFFECTS THE DISTAL PART OF THE COLON. 8
FIGURE 3-2: COMPARISON OF THE MECHANISMS OF SPONTANEOUS CRC DEVELOPMENT AND COLITIS-ASSOCIATED CRC 10
FIGURE 3-3: STRUCTURE OF THE HIF SUBUNITS HIF-1A AND HIF-2A 13
FIGURE 3-4: REGULATION OF HIFS BY PHDS. 14
FIGURE 3-5: CRYSTAL STRUCTURE AND HYDROXYLATION REACTION OF THE FIH DIMER 15
FIGURE 3-6: EFFECTS OF HIF ACCUMULATION REGARDING TUMOR METABOLISM 18
FIGURE 5-1: SCHEMA OF THE AOM-DSS(-DMOG) MOUSE MODEL FOR COLITIS-ASSOCIATED CRC. 27
FIGURE 5-2: THE FRET PRINCIPLE. 45
FIGURE 5-3: FLUORESCENCE SPECTRA OF MCITRINE AND MCHERRY 47
FIGURE 5-4: TCSPC DATA (ADAPTED FROM PROST-FINGERLE *ET AL.*, 2017). 48
FIGURE 6-1: KNOCKOUT EFFICIENCY IN THE FIH$^{FL/FL}$XVILLINCRE MICE PROVEN BY DIFFERENT METHODS. 49
FIGURE 6-2: EXPRESSION OF UPREGULATED HIF-1 TARGET GENES IN EXPERIMENTAL CONTROL ANIMALS. 50
FIGURE 6-3: RNASEQ DATA REVEALED A HIGH FIH KNOCKOUT EFFICIENCY. 51
FIGURE 6-4: DISEASE PROGRESS SHOWED NO DIFFERENCES BETWEEN WILDTYPE AND FIH KNOCKOUT ANIMALS OF THE AOM-DSS MODEL. 52
FIGURE 6-5: TUMOR DEVELOPMENT IN MICE OF THE AOM-DSS MOUSE MODEL. 53
FIGURE 6-6: H&E STAINING OF NORMAL COLON AND TUMOR TISSUE. 55
FIGURE 6-7: IMMUNOHISTOCHEMICAL STAINING OF FIH IN AOM-DSS-TREATED MICE. 56
FIGURE 6-8: POSITIVE FUNCTIONALITY TEST OF DMOG *IN VITRO*. 57
FIGURE 6-9: COLITIS PROGRESS IS REDUCED IN FIH KNOCKOUT MICE OF THE AOM-DSS-DMOG MODEL. 58
FIGURE 6-10: TUMOR GROWTH IN THE MURINE AOM-DSS-DMOG MODEL. 59
FIGURE 6-11: H&E STAINED COLON TISSUE FROM AOM-DSS-DMOG-TREATED MICE. 60
FIGURE 6-12: SPLEEN WEIGHT OF EXPERIMENTAL MICE. 61
FIGURE 6-13: FLOW CYTOMETRY ANALYSIS OF THE SPLEENS OF AOM-DSS-TREATED MICE. 62
FIGURE 6-14: FLOW CYTOMETRY ANALYSIS OF SPLEEN CELLS FROM MICE OF THE AOM-DSS-DMOG MODEL. 63
FIGURE 6-15: INCREASED EXPRESSION OF *F4/80* ANALYZED BY QPCR AND RNASEQ. 64
FIGURE 6-16: IMMUNOHISTOCHEMICAL STAINING OF F4/80 IN CONTROL ANIMALS. 65
FIGURE 6-17: THE NUMBER OF F4/80-POSITIVE CELLS IN DSS-AOM-TREATED COLONS 66
FIGURE 6-18: F4/80 EXPRESSION WAS STRONGER IN AOM-DSS-DMOG-TREATED WILDTYPE THAN FIH KNOCKOUT MICE. 67
FIGURE 6-19: FOLD CHANGE VALUES FROM THE RNASEQ DATA FOR IMMUNE RESPONSE GENES. 69
FIGURE 6-20: IPA RESULTS OF THE RNASEQ DATA FROM THE AOM-DSS MODEL. 70
FIGURE 6-21: IMMUNOHISTOCHEMICAL HYPOXYPROBE^{TM}-1 STAINING OF COLON TISSUE OF AOM-DSS-TREATED MICE. 71
FIGURE 6-22: IMMUNHISTOCHEMICAL HYPOXYPROBE^{TM}-1 STAINING OF COLON TISSUE OF AOM-DSS-DMOG-TREATED MICE. 72

FIGURE 6-23: HIF-1A PROTEIN STAINING IN AOM-DSS-DMOG-TREATED MICE. 74
FIGURE 6-24: IMMUNOHISTOCHEMICAL STAINING OF HIF-2A IN MICE FROM THE AOM-DSS-DMOG MODEL... 75
FIGURE 6-25: RNASCOPE® FOR *HIF1A* AND *HIF2A* IN TUMOR TISSUE OF AOM-DSS-DMOG-TREATED MICE..... 76
FIGURE 6-26: CO-IP PROVED THE INTERACTION OF FLUOROPHORE-TAGGED HIF-1A AND FIH IN HEK293T CELL LYSATES. 78
FIGURE 6-27: EXEMPLARY MICROSCOPIC PICTURES FROM TRANSFECTED HEK293T CELLS. 79
FIGURE 6-28: SEFRET MEASUREMENT OF CFP-HIF-2A AND YFP-ARNT CONSTRUCTS. 80
FIGURE 6-29: INTERACTION MEASUREMENTS WITH SEFRET FOR HIF-1A WITH ARNT AND FIH. 81
FIGURE 6-30: MEASUREMENTS OF SEFRET BETWEEN MTURQ2-HIF-1A AND MKO2-ARNT OR MKO2-FIH..... 82
FIGURE 6-31: FLIM MEASUREMENTS OF FLUOROPHORE-TAGGED HIF-1A AND ARNT / FIH IN HEK293T CELLS.. 84
FIGURE 6-32: FLIM MEASUREMENTS OF HIF-1A AND ARNT OR FIH UNDER THE TREATMENT OF THE HYDROXYLASE INHIBITOR DMOG AND WITHOUT. 85
FIGURE 7-1: GRAPHICAL SUMMARY OF THE RESULTS FROM THE EXPERIMENTAL MOUSE MODELS FOR CRC DEVELOPMENT. 92
FIGURE 9-1: IMMUNOHISTOCHEMICAL HIF-1A STAINING IN COLON TISSUE FROM AOM-DSS-TREATED MICE. 108
FIGURE 9-2: IMMUNOHISTOCHEMICAL HIF-2A STAINING IN AOM-DSS-TREATED MICE. 109
FIGURE 9-3: NEGATIVE CONTROL FOR THE *IN SITU* HYBRIDIZATION WITH RNASCOPE®. 110
FIGURE 9-4: DETECTION OF *HIF1A* AND *HIF2A* MRNA BY *IN SITU* HYBRIDIZATION IN AOM-DSS-TREATED MICE. 110

9.3 Table of tables

TABLE 5-1: LABORATORY EQUIPMENT/KITS AND ITS PRODUCERS. 20
TABLE 5-2: USED CONSUMABLES AND CHEMICALS IN THIS WORK. 21
TABLE 5-3: FORMULAS OF THE MEDIA AND SOLUTIONS THAT WERE USED IN THIS WORK. 24
TABLE 5-4: CALCULATION OF THE DAI AFTER KIM *ET AL.* (2012). 27
TABLE 5-5: FACS ANTIBODIES/DIES WITH CONJUGATED FLUOROPHORE AND DILUTION FACTOR. 29
TABLE 5-6: REACTION MIX FOR CDNA SYNTHESIS. 31
TABLE 5-7: PROTOCOL OF CDNA SYNTHESIS IN THE MASTERCYCLER. 31
TABLE 5-8: REACTION MIX FOR A PCR PER SAMPLE. 32
TABLE 5-9: PRIMER SEQUENCES FOR QUALITATIVE AND QUANTITATIVE PCRS. 32
TABLE 5-10: THE STANDARD PCR PROGRAM FOR THE GOTAQ G2 POLYMERASE. 33
TABLE 5-11: REACTION MIXTURE FOR A QPCR APPROACH. 33
TABLE 5-12: THE QPCR PROGRAM FOR THE BIOZYM BLUE S'GREEN QPCR KIT. 34
TABLE 5-13: COMPOSITION OF THE STACKING AND THE SEPARATING GEL FOR SDS-PAGE. 35
TABLE 5-14: PROTOCOL OF DEHYDRATION OF TISSUE SAMPLES FOR HISTOLOGICAL ANALYSIS. 36
TABLE 5-15: PARAFFIN REMOVAL AND REHYDRATION PROCESS FOR IMMUNOHISTOCHEMICAL STAININGS. ... 37
TABLE 5-16: PARAFFIN REMOVAL AND REHYDRATION PROCESS FOR H&E STAININGS. 37
TABLE 5-17: PRIMARY ANTIBODIES USED IN IMMUNOHISTOCHEMICAL STAININGS. 39
TABLE 5-18: REACTION MIXTURE FOR THE TRANSFECTION OF HEK293T CELLS WITH TURBOFECT™. 41
TABLE 5-19: REACTION MIXTURE FOR THE TRANSFECTION OF U2OS CELLS WITH LIPOFECTAMINE™ 3000. 41
TABLE 5-20: LIST OF PLASMIDS 42
TABLE 6-1: IN AOM-DSS-TREATED FIH$^{FL/FL}$XVILLINCRE MICE DOWNREGULATED GO TERMS 68
TABLE 6-2: RNASEQ DATA SHOWED DOWNREGULATED IMMUNE RESPONSE GENES 68

9.4 Table of abbreviations

AOM	azoxymethane
APS	ammonium persulfate
Arg-1	arginase-1
ARNT	aryl hydrocarbon receptor nuclear translocator
ATP	adenosine triphosphate
bHLH	basic helix-loop-helix
Bnip3l	B-cell lymphoma 2 interacting protein 3 like
BSA	bovine serum albumin
CBP	CREB binding protein
CD	cluster of differentiation
cDNA	complementary DNA
CFP	cyan fluorescent protein
Co-IP	co-immunoprecipitation
C_T	cycle of threshold
C-TAD	C-terminal transactivation domain
DAB	3,3'-Diaminobenzidine
DEPC	diethyl pyrocarbonate
DMEM	Dulbecco's Modified Eagle Medium
DMOG	dimethyloxaloylglycine
DMSO	dimethyl sulfoxide
DNA	deoxyribonucleic acid
DSS	dextran sodium sulfate
DTT	dithiothreitol
E2F3	E2F transcriptions factor 3
EDTA	ethylenediaminetetraacetic acid
EGTA	ethylene glycol-bis(β-aminoethyl ether)tetraacetic acid
EPO	erythropoietin
FACS	fluorescence activated cell sorting
FCS	fetal calf serum
FIH	factor-inhibiting HIF
FLIM	fluorescence lifetime imaging
FRET	fluorescence resonance energy transfer
FVD	fixable visbility dye
GLUT1	glucose transporter 1
GTC	guanidinium thiocyanate
HIF	hypoxia-inducible factor

HRE	hypoxia-responsive elements
i.e.	that is (Latin: *id est*)
IL	interleukin
inos	inducible NO synthase
KCl	potassium chloride
KH_2PO_4	potassium hydrogen phosphate
KLF3	Kruppel-like factor 3
KMT2D	lysine-specific methyltransferase 2D
LB	lysogeny broth
LiCl	lithium chloride
Mdm2	mouse double minute 2 homolog
MEFs	murine embryonic fibroblasts
mRNA	messenger RNA
Na_2HPO_4	sodium hydrogen phosphate
NaCl	sodium chloride
NaF	sodium fluoride
NaOAc	sodium acetate
NP40	Nonidet® P40
N-TAD	N-terminal transactivation domain
NTP	nucleotide triphosphate
ODD	oxygen-dependent degradation domain
PAS	Per-Arnt-Sim
PBS	phosphate-buffered saline
PCR	polymerase chain reaction
PFA	paraformaldehyde
PGK1	phosphoglycerate kinase 1
PHD	prolyl hydroxylase
PI	proteinase inhibitor
PMSF	phenylmethylsulfonyl fluoride
pVHL	von-Hippel-Lindau protein
qPCR	quantitative PCR
RNA	ribonucleic acid
RT	room temperature
SD	standard deviation
SDS	sodium dodecyl sulfate
SDS-PAGE	SDS polyacrylamide gel electrophoresis
seFRET	sensitized emission FRET

SOB	super optimal broth
SOX4	SRY-box 4
TAE	Tris-acetate-EDTA
TBS	tris-buffered saline
TCSPC	time-correlated single-photon counting
TEMED	tetramethylethylenediamine
TP53	tumor protein p53
Tris	tris(hydroxymethyl)-aminomethane
UC	ulcerative colitis
UV	ultraviolet
VEGF	vascular endothelial growth factor
YFP	yellow fluorescent protein

9.5 List of publications and congress contributions

Papers

1. **Schützhold, V., Fandrey, J., Prost-Fingerle, K. (2018)** Fluorescence Lifetime Imaging Microscopy (FLIM) as a tool to investigate hypoxia-induced protein-protein interaction in living cells. *Methods Mol Biol*. 1742:45-53.
2. **Prost-Fingerle, K., Hoffmann, M.D., Schützhold, V., Cantore, M., Fandrey, J. (2017)** Optical analysis of cellular oxygen sensing. *Exp Cell Res*. 356(2):122-127.

Posters

1. **Schützhold, V., Prost-Fingerle, K., Fandrey, J., Winning, S. (2017)** The role of hypoxia-inducible factors (HIFs) in a mouse model of colorectal cancer. Annual Retreat of the Graduate School of Biomedical Science (BIOME) 'Cellular and Molecular Immunology' / 'Infectious Diseases' / 'Tumour and Signalling' Cores, Xanten. Poster Prize 'Tumour and Signalling'.
2. **Schützhold, V., Prost-Fingerle, K., Fandrey, J., Winning, S. (2017)** The role of hypoxia-inducible factors (HIFs) in a mouse model of colorectal cancer. 16th Day of Science at the Medical Faculty, University of Duisburg-Essen, Essen.
3. **Schützhold, V., Bicker, A., Fandrey, J., Winning, S. (2018)** Factor-inhibiting HIF (*Fih*) knockout enables an anti-inflammatory effect of HIFs in a mouse model of colitis-induced colon cancer. 1st Europhysiology, Joint Meeting of the Physiological Society, the Scandinavian Physiological Society, the German Physiological Society and the Federation of European Physiological Societies, London.
4. **Schützhold, V., Bicker, A., Fandrey, J., Winning, S. (2018)** Factor-inhibiting HIF (*Fih*) knockout enables an anti-inflammatory effect of HIFs in a mouse model of colitis-induced colon cancer. 17th Day of Science at the Medical Faculty, University of Duisburg-Essen, Essen.
5. **Schützhold, V., Prost-Fingerle, K., Bicker, A., Fandrey, J., Winning, S. (2019)** The role of the factor inhibiting HIF (FIH) in a mouse model of colitis-induced colorectal cancer. Annual Retreat of the Graduate School of Biomedical Science (BIOME) 'Cellular and Molecular Immunology' / 'Infectious Diseases' / 'Tumour and Signalling' Cores, Bonn.
6. **Schützhold, V., Prost-Fingerle, K., Bicker, A., Fandrey, J., Winning, S. (2019)** The role of the factor inhibiting HIF (FIH) in a mouse model of colitis-induced colorectal cancer. 18th Day of Science at the Medical Faculty, University of Duisburg-Essen, Essen.

Talks

1. **Schützhold, V., Fandrey, J., Winning, S. (2018)** Factor-inhibiting HIF (*Fih*) knockout enables an anti-inflammatory effect of HIFs in a mouse model of colitis-induced colon cancer. Annual Retreat of the Graduate School of Biomedical Science (BIOME) 'Cellular and Molecular Immunology' / 'Infectious Diseases' / 'Tumour and Signalling' Cores, Cologne. Abstract book p. 17.
2. **Schützhold, V., Prost-Fingerle, K., Bicker, A., Fandrey, J., Winning, S. (2019)** Factor-inhibiting HIF (*Fih*) knockout enables an anti-inflammatory effect of HIFs in a mouse model of colitis-induced colon cancer. 98th Meeting of the German Physiological Society, Ulm, Abstract book #129.

9.6 Acknowledgements

The acknowledgements are not included in the online version for data protection reasons.

9.7 Personal data sheet

The personal data sheet is not included in the online version for data protection reasons.

9.8 Declarations

Erklärung:
Hiermit erkläre ich, gem. § 7 Abs. (2) d) + f) der Promotionsordnung der Fakultät für Biologie zur Erlangung des Dr. rer. nat., dass ich die vorliegende Dissertation selbständig verfasst und mich keiner anderen als der angegebenen Hilfsmittel bedient, bei der Abfassung der Dissertation nur die angegeben Hilfsmittel benutzt und alle wörtlich oder inhaltlich übernommenen Stellen als solche gekennzeichnet habe.

Essen, den _____ _____

Unterschrift der Doktorandin

Erklärung:
Hiermit erkläre ich, gem. § 7 Abs. (2) e) + g) der Promotionsordnung der Fakultät für Biologie zur Erlangung des Dr. rer. nat., dass ich keine anderen Promotionen bzw. Promotionsversuche in der Vergangenheit durchgeführt habe und dass diese Arbeit von keiner anderen Fakultät/Fachbereich abgelehnt worden ist.

Essen, den _____ _____

Unterschrift der Doktorandin

Erklärung:
Hiermit erkläre ich, gem. § 6 Abs. (2) g) der Promotionsordnung der Fakultät für Biologie zur Erlangung des Dr. rer. nat., dass ich das Arbeitsgebiet, dem das Thema „The role of hypoxia-inducible factors (HIFs) in a mouse model of colorectal cancer“ zuzuordnen ist, in Forschung und Lehre vertrete und den Antrag von Vera Schützhold befürworte und die Betreuung auch im Falle eines Weggangs, wenn nicht wichtige Gründe dem entgegenstehen, weiterführen werde.

Essen, den _____ _____

Unterschrift Univ.-Prof. Dr. med. Joachim Fandrey